Fusion of first principles driven and system science approaches to advance radiation belt forecasting

I. P. Pakhotin

September 2014

Abstract

Modern radiation belt models can be broadly split into either physics-driven diffusion based algorithms, or data science techniques that utilise the continuous data coverage from satellites at geostationary orbit and the Lagrange point L1 to apply statistical data analysis methods to predict electron fluxes at geostationary orbit. The first kind, while posessing generality due to their physical nature, lack accuracy compared to their data-driven counterparts. This is because the magnetosphere is a highly complex system that is not easy to model and its dynamics are not yet fully understood. Meanwhile, data-driven methods possess statistical accuracy, but cannot predict outside their operating parameters, and so on their own provide no information about what happens in the wider radiation belt region.

This thesis is devoted to the development of a model that combines the two approaches into one unified system, attempting to combine the predictive range of physical modelling with the accuracy of the data-driven approach. This model uses geosynchronous orbit fluxes predicted using an advanced data science technique as an input to drive a physics-based radiation belt modelling code. The model has been developed and tested for a range of energy channels, magnetospheric conditions, and with various modifications. It was validated using data from NASA's recent Van Allen probes mission and with NOAA's GOES-13 geostationary satellite. The model results are in good agreement with observations, with the sources of inaccuracies explored in the manuscript. This work is a first attempt to create such a model, and potential improvements are outlined that should further increase accuracy.

A further modification of the model is explored that is found to provide superior performance at geostationary orbit at the cost of degraded performance elsewhere. It is proposed to use this modification in tandem with the main model, where accurate information about geostationary orbit is required. The modification has been tested on long-duration time periods and was found to generate good predictions for high-energy electron fluxes.

The role of electromagnetic ion cyclotron (EMIC) waves is explored using wave vector analysis and calculation of minimum resonant energies. The aim is to identify what effect EMIC waves have on electron dynamics at energies below 1 MeV. The conclusions are that EMIC waves, under certain conditions, do affect these electron populations in the magnetosphere, and their effect should be included in a representative radiation belt model. This is suggested as a further improvement to the simulation.

Acknowledgements

First and foremost I would like to sincerely thank my supervisor, Prof Michael Balikhin, for guiding me through this PhD, inspiring me every step of the way, and helping to turn this thesis into reality. It has been an honour and a pleasure to work under his mentorship. Prof Michael Balikhin truly is a great supervisor, a conssumate professional and a genuine pleasure to work with. To me he will always be one of the greats in the field of space plasma physics. I would also like to acknowledge my second supervisor, Dr Simon Pope, who dilligently helped me through the technical aspects of the PhD and was always at hand when needed.

I would also like to extend my sincere thanks to all my colleagues at the University of Sheffield Space Systems Laboratory: Homayon Aryan, Dr Simon Walker, Dr Andrew Dimmock, Dr Richard Boynton, Dr Viktor Fedun, Prof Robertus Von Fay-Siebenburgen, Dr Olga Amariutei and Dr Keith Yearby. Thank you for showing me the ropes in the beginning and taking the time to answer all the small and annoying questions in those early days. It has been a pleasure to work with you, travel to conferences with you and co-author papers with you.

In addition I would like to thank my American colleagues Dr Yuri Shprits, Dr Alexander Drozdov, Dr Dmitry Subbotin and Dr Adam Kellerman. It was a real pleasure working with this team on the VNC project and I look forward to more exciting collaborations in the future. In particular I would like to acknowledge Dr Dmitry Subbotin's help in providing the algorithm to convert differential fluxes into integral fluxes, and Dr Alexander Drozdov for the methodology to translate fluxes from geostationary orbit to the outer VERB boundary.

I would like to acknowledge Dr Illia Silin for his fruitful collaboration in the investigation of EMIC wave vectors and minimum resonant energies.

I would like to extend a special thanks to the journal editors and the referees who reviewed my papers.

Thanks go to the organisers and teachers of the STFC 2013 Plasma Physics School in Budapest. To all the PhD students I have met there I wish all the best of luck in completing their doctorates.

Last but by no means least, I would like to say a huge thank you to my parents who raised me and, accomplished scientists themselves, inspired me in this profession, as well as to my physics teachers in school and college. I greatly thank my wife Venera and to all my friends from Sheffield and elsewhere who have supported me through the difficult times and kept me going. A special mention does to my beautiful daughter Amelie who was born in the last months of the PhD and who helped give me the focus to carry through this work to completion.

The work leading to this thesis was sponsored by STFC. Spacecraft data was provided for the GOES-13 satellite courtesy of NOAA, for the Van Allen probes courtesy of NASA, and for the Cluster mission courtesy of the Cluster Active Archive.

Contents

List of Figures

1 Chapter 1: Introduction

1.1 Motivation

Space weather-related geomagnetic disturbances, as well as causing electrical disturbances to the terrestrial power grid [e.g. Schrijver et al., 2014] and communications [e.g. MacAlester and Murtagh, 2014], also affect space satellites [e.g. Baker, 1996]. Particles can lead to a charge build-up on the spacecraft; this potential can then cause a discharge and is a source of noise in electrical transmission. Meanwhile, higher energy particles, particularly the so-called 'killer' electrons above 2 MeV, can penetrate into the spacecraft's interior and cause radiation damage or interfere with circuitry operation. For this reason, there is a lot of interest in these high-energy electrons, both for space weather prediction as well as to understand expected radiation dozages and so design spacecraft to withstand them. High-energy electrons occur as trapped particles in the radiation belts, which are separated by a zone of reduced particle flux known as the slot region. While the inner belt is relatively stable with predictable variations linked to the solar cycle, the outer belt is highly dynamic, with energetic particle fluxes sometimes increasing by orders of magnitude over several hours. The outer belt is often located around geostationary orbit, and potentially affects the operation of numerous geosynchronous satellites. A statistical study of magnetic storm activity with energetic particle flux counduced by Reeves et al. [2003] showed that only about half (53%) of magnetic storms produced flux increases, with one in five (19%) actually leading to flux decreases, and 28% leaving flux levels largely unchanged. It is thus clear that the link between geomagnetic activity and radiation belt fluxes is not linear, but a result of competing electron loss and acceleration mechanisms.

This thesis is devoted to radiation belt prediction and understanding, both from a science perspective and from the view of providing radiation belt flux forecasts that can be used by satellite operators. Knowledge of an imminent increase in energetic particle fluxes can give satellite operators time to switch off non-critical subsystems to spare them from potential damage. In theory it can help increase the service life of a satellite. Two approaches to radiation belt modelling are explored - the physics-based methodology and the data-driven approach. The anatomy of the state-of-the-art in physics-driven prediction is analysed, and two subsystems representative of the two approaches are merged into one single system that promises to combine the accuracy of one and the predictive range of the other. The system is then validated against satellite observations both at geostationary orbit and inside the heart of the outer belt - using data from the new Van Allen probes - and both its merits and its weaknesses are critically examined. A role of one important plasma wave mode - the electromagnetic ion cyclotron (EMIC) instability - is examined in this context, with vector analysis performed to study minimum resonant energies and thus the extent of this instability on the radiation belt population.

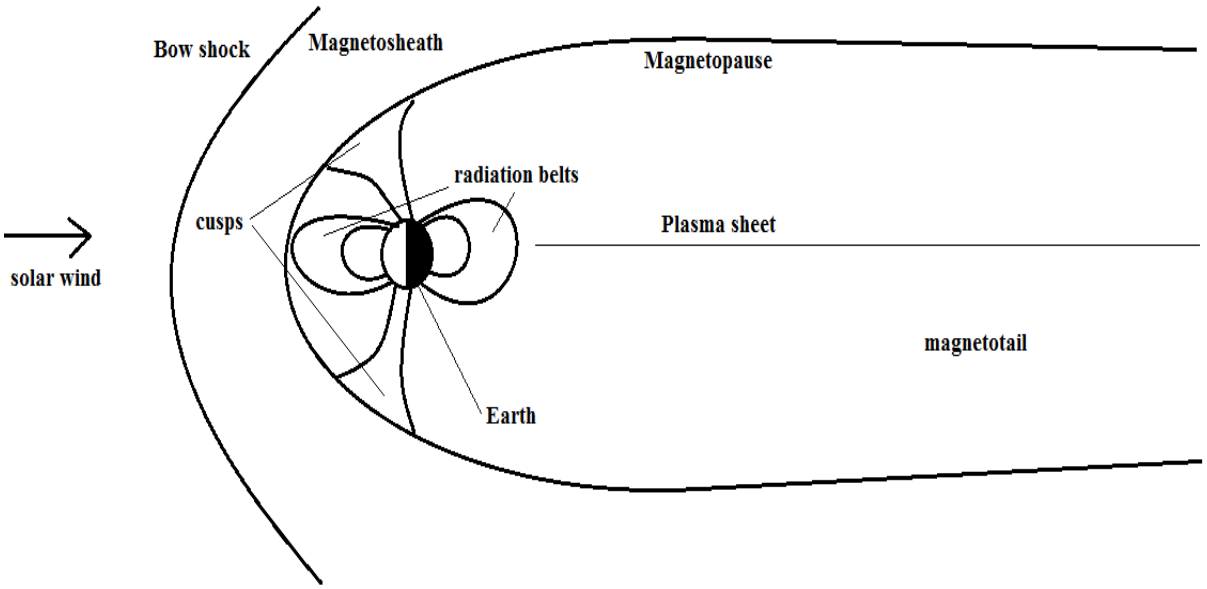

Figure 1: A schematic representing the magnetosphere.

1.2 Structure of the magnetosphere

The near-Earth environment is a cold plasma, with ions and electrons forming a collective magnetised fluid that is acted upon by various magnetic forces, chief among them the magnetic field of the Earth. The Earth's magnetic field is a tilted dipole (magnetic north is slightly offset from the geographic north) that is compressed by a stream of charged particles from the Sun known as the solar wind. This leads the magnetosphere to stretch out into a long magnetotail on the night side, while it is compressed on the dayside. Figure 1 shows the general magnetosphere structure. A thin current sheet exists in the magnetotail around the magnetic equator. Field lines of the magnetosphere can couple to field lines of the solar wind - the interplanetary magnetic field or IMF - in a process known as magnetic reconnection. If this occurs in the tail, the tension in the newly reconnected field lines is released and the field lines move inwards towards the Earth. This is known as a substorm. The rapid changes in the magnetic field preceeding this substorm is called a dipolarisation front. Magnetic reconnection and substorms can bring new charged particle populations inwards, towards the inner magnetosphere. In general, even in the absense of any substorms, charged particles from the tail steadily drift towards the Earth. The reason is the so-called $E \times B$ drift, where configuration of electric and magnetic fields in the tail cause the particles to move in an Earthwise direction. This is known as convection. As the particles approach the inner magnetosphere, they become trapped by the magnetic field configuration and circle the Earth. Ions and elec-

trons are oppositely charged, and so they circle the Earth in different directions (ions drift duskward, while electrons drift dawnward in the frame of reference looking down on the Earth's north pole). This causes a current system to form around the Earth, known as the ring current. The trapped particles drifting around the Earth form the ring current and radiation belts.

There is a region of relatively high plasma density that corotates with the Earth, known as the plasmasphere. Various plasma waves grow in the plasmasphere or at its limits near the plasmapause, because a higher density leads to a lower wave group velocity, and so a wave has more chance to become unstable as it propagates before leaving the generation region. These waves interact with trapped radiation belt particles in complex ways, either growing at the expense of their energy, or extinguishing while energising the particles. Local acceleration by waves can produce very high-energy populations that present a danger to spacecraft. Meanwhile, wave-particle interactions can also modify the trapped particle trajectories in such a way that they precipitate into the atmosphere and are lost from the system.

This thesis deals with understanding radiation belt dynamics. It is concerned with predicting radiation belt fluxes and evaluating various models that are in use for this purpose today. Since plasma waves play such a large role in radiation belt dynamics, wave-particle interactions are included in most physics-based radiation belt models in use today. A chapter of this work is devoted to studying a particular plasma wave - the electromagnetic ion cyclotron (EMIC) wave - because these instabilities are believed to be very effective at scattering high-energy particles that present the most danger to satellites.

1.3 Adiabatic invariants

In general, the motion of a particle in the presence of electric and magnetic fields can be described by:

$$\frac{d}{dt}(m\frac{d\mathbf{r}}{dt}) = q(\frac{d\mathbf{r}}{dt} \times \mathbf{B} + \mathbf{E}) + \mathbf{F} \tag{1}$$

where $\mathbf{r}$ represents the particle's position as a function of time t, initial position $\mathbf{r}_0$ and initial velocity $\mathbf{v}_0$ while $\mathbf{B}$, $\mathbf{E}$ and $\mathbf{F}$ represent magnetic field, electric field and external non-electromagnetic force respectively. In radiation belt theory, particle dynamics can be described by three quasi-periodic motion types: gyration, bounce and drift, each associated with what is known in literature as the first, second and third adiabatic invariants respectively.

Gyration is a consequence of the particle's motion in a magnetic field. Due to the Lorenz force, a particle with a velocity vector component perpendicular to the magnetic field vector experiences a force perpendicular to both. Thus a particle will gyrate around a field line with a frequency $\omega = \frac{eB}{m}$ where e is particle charge, B is magnetic field strength and m is the mass of the particle. This gyration has an associated **first invariant** - the magnetic moment - expressed as $\mu = \frac{p_\perp^2}{2m_0 B}$ where $p_\perp$ is perpendicular momentum and m_0 is the rest mass of

the particle. Perpendicular and parallel in this situation refer to the components of the vector with respect to the ambient magnetic field.

The **second invariant** is related to the ratio of parallel and perpendicular components of a particle's velocity - or the pitch angle. Let us consider a particle with a non-zero parallel velocity component. Such a particle, along with gyration, will move up or down a field line, eventually entering a region of differing magnetic field strength. If the Earth's magnetic field is approximated as a dipole, a particle that starts out at the equator and moves poleward will move into a region of stronger magnetic field strength. Conserving the magnetic moment (the first invariant), a rise in B must also correspond to a rise in $p_\perp$. Since the total momentum remains the same, this increase in $p_\perp$ happens at the expense of $p_\parallel$. When $p_\parallel$ drops to zero the particle is said to have reached its mirror point. It is then reflected in the opposite direction: any excursion from the mirror point into a region of lower field strength will correspond with an increase in parallel velocity in that direction. The result is the particle accelerating back where it came from until it reaches the magnetic minimum (usually around the magnetic equator) and travels towards the other pole where the process is repeated. The back-and-forth bouncing of charged particles between mirror points at opposite hemispheres can be represented as a simple pendulum with a virtual force - the 'mirror force', 'pushing' the particles away from the mirror points. The corresponding equation for the second invariant is

$$J = \oint p_\parallel ds \tag{2}$$

where $p_\parallel$ is the parallel component of particle momentum, and the integration is along the field line over the path of one bounce period.

The **third invariant** involves an azimuthal drift around the Earth as a consequence of gradient and curvature drifts. The general form for this invariant is

$$K = e \oint A_\phi ds = e\Phi \tag{3}$$

where Φ is the total magnetic flux enclosed by the drift trajectory.

The gradient drift comes about because of a radial variation in magnetic field strength. The gyroradius - or Larmor radius - of a gyrating particle is $r_g = \frac{mv_\perp}{|q|B}$ where m is particle mass, $v_\perp$ is perpendicular velocity, $|q|$ is modulus of the charge and B is magnetic field strength. Since B varies radially (in particular, the field is stronger closer to Earth), the Larmor radius is smaller on the side facing Earthward. As a result, trapped charged particles 'shuffle' azimuthally in a direction dependent on their polarity, at rates determined by the particle energy (in particular, $v_\perp$), ionisation state and radial field strength variation.

The curvature drift comes about as a result of a centrifugal force acting on a particle as it drifts along a curved field line. The force is directed radially outwards, and in the presence of a magnetic field generates a drift velocity

that is perpendicular to both the force and B vectors. Thus this drift is also azimuthal. Its magnitude can be shown to be $v_{curv} = \frac{m}{q}\frac{v_\parallel^2}{B}\frac{B\times\nabla B}{B^2}$. Combining the two drifts together yields a combined drift velocity:

$$v_D = \frac{m}{2qB}(v_\perp^2 + 2v_\parallel^2)\frac{B\times\nabla B}{B^2} \tag{4}$$

Since particles with the same energies (but different pitch angles) possess different drift velocities, over time this can lead to areas of pitch-angle anisotropy forming in parts of the magnetosphere, which can give rise to plasma instabilities.

In the absence of radial electric fields and with a dipolar magnetic field, the particles will have perfect symmetry and their azimuthal orbits will trace out a circle whose radius is dependent on the magnetic field strength and on particle energy. In a nondipolar magnetic field, where magnetic field strength varies azimuthally due to compression of the magnetosphere by the solar wind, the azimuthal particle orbits trace out ovals. In the presence of slowly time-varying magnetic fields and induced electric fields, particle drift orbits can change; once the disturbance passes and the dipole strength returns to normal, the particle guiding drift shells often return to pre-storm values. The condition for this to happen is that the invariant be conserved (i.e. that change be slow compared to the characteristic drift time scales). Finally, violation of the third invariant by ULF waves can occur in which case particles are radially transported via random re-energisation with a consequent change in guiding field line. This is the basis behind radial diffusion, and is driven by waves of frequencies (mHz) close to the characteristic third invariant timescales (tens of minutes to hours). The redistribution of particle energy and consequently, radial distance, is random, but the net movement as in all diffusion processes is from an area of high phase space density to low phase space density.

The drifting particles following lines of equipotential magnetic field in a compressed dipole tend to move radially outwards during magnetic daytime. This brings them closer to the magnetopause. The magnetopause itself is also much closer to Earth on the magnetic dayside than near magnetic midnight. During compression events, some particles may find their drift orbits intersecting the magnetopause around magnetic noon. If that happens, they escape from the Earth's field lines into interplanetary space. This phenomenon is known as magnetopause shadowing.

1.4 Plasma waves

Using Maxwell equations and equations of charged particle motion, is it possible [Stix, 1962] to derive wave modes for a cold plasma in a homogenous magnetic field. A generally low-beta plasma (beta being the ratio between magnetic and thermal pressure) such as that encountered in the magnetosphere fits that description reasonably well and in fact it will be seen that many wave modes encountered in the radiation belts belong to the basic modes of the cold plasma.

For energy propagating parallel to the local magnetic field, modes in the right-hand polarised R-mode (1) and left-hand polarised L-mode (2) are permissible.

$$R = 1 - \sum_k \frac{\omega_{pk}^2}{\omega^2}\left(\frac{\omega}{\omega + \epsilon_k \Omega_k}\right) \equiv 0 \tag{5}$$

$$L = 1 - \sum_k \frac{\omega_{pk}^2}{\omega^2}\left(\frac{\omega}{\omega - \epsilon_k \Omega_k}\right) \equiv 0 \tag{6}$$

where $\omega_{pk} = (\frac{n_k e^2}{m_k \epsilon_0})^{0.5}$ is the plasma frequency of charged particle species k, ϵ_k is the charge state (positive for ions, negative for electrons), and $\Omega_k = \frac{eB}{m_k}$ is the charged particle cyclotron frequency with m_k being particle mass. In the radiation belts, the R-mode corresponds to various whistler instabilities including chorus waves and plasmaspheric hiss, while the L-mode is the electromagnetic ion cyclotron (EMIC) wave. From the solution of Equation (20) in Stix [1962] for E_x and E_y it can be shown that the R-mode, as its name suggests, is right-hand polarised, while the L-mode is left-hand polarised. Highly oblique whistlers have been observed in the magnetosphere and are called equatorial noise or magnetosonic waves [e.g. Russell et al., 1970].

For propagation perpendicular to the local magnetic field, two more modes are permissible - the first is the plasma mode P defined as

$$P = 1 - \sum_k \frac{\omega_{pk}^2}{\omega^2} \tag{7}$$

It can be seen that in a finite plasma this mode has no resonance - $\omega \to 0$ would correspond to an infinitely large wavelength.

The second permissible mode is represented by the hybrid resonances $\frac{RL}{S}$ where R and L were defined earlier and S is the sum quantity defined as

$$S = \frac{1}{2}(R + L) \tag{8}$$

Chorus waves

Chorus waves have been linked to substorms [e.g. Tsurutani and Smith, 1974] and are believed to be caused by drift shell splitting [e.g. Roederer, 1970, Tsurutani and Smith, 1977, Min et al., 2010]. Particles injected from a substorm may initially have an isotropic distribution of pitch angles. However particles with different pitch angles have different mirror points. A particle's 2nd (bounce) invariant is given by $J = 2pI$ where p is particle momentum and I is the integral

$$I = \int_{S_m}^{S_m} [1 - \frac{B(s)}{B_m}]^{0.5} \, \mathrm{d}s \tag{9}$$

where S_m is the location of the mirror point, $B(s)$ is the magnetic field strength at a particular value of length s along the field line, and B_m is field

strength at a mirror point. Particles with different pitch angles have different values of I. Each particle during the course of its drift will bounce along a field line that passes through the intersection of its own I=const and B_m=const surfaces. Thus if particles with different pitch angles (and correspondingly different values of I) start out on the same field lines at injection, by the time they have drifted to the dawn side, they will occupy different field lines. In particular it can be shown that particles with lower pitch angles will occupy L-shells at lower radial distances as they drift eastwards, compared to high-pitch angle particles. The relative difference between pitch angle populations will lead to an abundance of high pitch angle particles at high L-shells by the time the electrons have drifted to the dawn sector, and this anisotropy can trigger the chorus instability. Abel et al. [2006] showed statistically that chorus waves can also be caused by drift echoes (injected electrons drifting all the way around the Earth and back into the dawn sector) rather than the initial substorm.

Electromagnetic Ion Cyclotron (EMIC) waves

The EMIC wave is an L-mode instability driven by ion anisotropy, in many ways completely analogous to the R-mode whistler (which is driven by electron anisotropy). They usually occur near the plasmapause and plasmatrough region where sharp density gradients are encountered, around the post-noon and dusk sector. They are left-hand circularly polarised and field-aligned at generation. They exist below the H^+ gyrofrequency and typically have frequencies of a few Hz. They can also be observed just below the gyrofrequencies of heavier ions (He^+, O^+). Cold plasma wave theory predicts a stop band between the He^+ and H^+ gyrofrequencies (as well as between He^+ and O^+ gyrofrequencies) where the wave mode has a cut-off and cannot propagate. However, a stop band is not always present and does not exist when thermal effects are considered [e.g. Silin et al., 2011b].

EMIC waves resonate with trapped ions and high-energy electrons, leading to pitch-angle scattering of both species. The size of the electron population affected by this instability is unknown, though it is believed that the lower limit for resonance with EMIC waves is around 1 MeV. Although the area affected by EMIC waves is quite localised in MLT, they are believed to be a very efficient scattering mechanism of high-energy electrons, so their cumulative effect over several drift periods can be significant. Their pitch-angle scattering rates increase with increasing energy [e.g. Shprits et al., 2008b].

Ion anisotropy for their excitation is generated by drift shell splitting in the same way as for electrons. Since substorm-injected ions drift in the opposite direction to electrons, EMIC waves tend to occur mostly in the dusk MLT sector. As well as drift shell splitting, the effects of Shabansky orbits on ion anisotropy generation have also been investigated [McCollough et al., 2012]. In a compressed magnetosphere, pockets of minimum B develop off the equator. When drifting ions enter such a region, they can cease bouncing between their usual mirror points and instead begin bouncing between new mirror points either side of this new off-equatorial B_{min} [Shabansky, 1971, Figure 13a in paper]. This new bounce motion covers a shorter distance, so their second invariant drops. Since their total kinetic energy remains the same, the effective

change is their pitch angle - the loss in parallel momentum $J = \oint p_{\|} ds$ implies a shift of energy into the perpendicular component. Even particles that do not change J on entering regions with off-equatorial B_{min} pockets still contribute to anisotropy. This is because as they encounter regions near the equator where the magnetic field increases along the field line, they transfer parallel energy into perpendicular energy to conserve their μ and kinetic energy, since at the equator the magnetic field now increases to a local maximum. This leads to a temperature anisotropy near the equator.

It is useful to note that both drift-shell splitting and Shabansky orbit effects are non-energising processes. That is, overall particle energy is unchanged, there is a simple redistribution between parallel and perpendicular energy components. Other processes that can generate anisotropy are summarised in [McCollough et al., 2010, and references therein] and include for example, adiabatic energisation, energisation by the convective electric field and interaction with solar wind-driven ULF waves, which are all energising processes and do change the total particle enegies.

Magnetosonic waves

These waves are observed between the proton gyrofrequency and half the lower hybrid resonance frequency. Peak wave intensities occur within 2 degrees of the magnetic equator and the wave intensity diminishes rapidly outside that region [e.g. Němec et al., 2006]. The waves propagate both radially and asimuthally around the minimum B surface. Meredith et al. [2008] conducted a statistical study of these waves using CRRES data and concluded they were likely to be formed by proton ring distributions of > 30 keV protons injected into the magnetosphere during substorms. They are observed at all magnatic local times outside the plasmapause but are restricted to the duskside MLTs inside the plasmapause. The most intense emissions were observed around L=3-4. They are believed to be highly oblique whistlers [e.g. Russell et al., 1970] and are electromagnetic in nature. They are linearly polarised along the static magnetic field, so cannot be in cyclotron resonance with trapped particles. However, they have the proper characteristics to be in bounce resonance with energetic electrons and are believed capable of accelerating electrons to MeV energies.

Plasmaspheric hiss

Also known as equatorial noise, hiss is a broadband, incoherent emission that exists within the plasmasphere in two distinct latitude regions [Meredith et al., 2004]. Equatorial hiss is strongest form 0600 to 2100 MLT, while mid-latitude hiss is predominantly in the region 0800-1800 MLT. It is believed to be a subset of chorus that penetrates into the plasmasphere at high latitudes and undergoes multiple reflections within the plasmasphere, such that it crosses the equator with small wave normal angles and does not undergo significant Landau damping [Bortnik et al., 2009]. These emissions thus persist within the plasmasphere and form an incoherent background. Hiss is believed to be responsible for the formation of the slot region, pitch-angle scattering electrons into the loss cone.

1.5 Radiation belt dynamics

The first theories to explain the radiation belt structure came from adiabatic invariant theory, where Fälthammar [1965] argued that random variation in electric and magnetic fields can violate the third (drift) invariant. This would lead to particles changing their radial position while conserving their first and second invariants, in a manner similar to diffusion and described by a diffusion equation. Thus it was argued that particles convected in would radially diffuse inwards, gaining energy. Outward radial diffusion, meanwhile, would be accompanied by energy loss. Meanwhile, local acceleration by plasma waves like chorus was another mechanism that was proposed. Superimposed epoch analysis was used to try and distinguish the contributions of the two [O'Brien et al., 2003]. That study concluded that both chorus acceleration and radial diffusion produced flux increases in the recovery phase of magnetic storms. Radial diffusion was seen as a more significant acceleration mechanism at GSO, while both were deemed about equally important at lower L-shells.

Following adabatic theory [e.g. Schulz and Lanzerotti, 1974] it can be seen why there is a distinction between local acceleration and radial diffusion processes. There is a wide variation in characteristic timescales between the third invariant (drift) and the first and second (gyration and bounce). Processes that violate the first two invariants do also violate the third one, but any change in drift invariant can then be assumed to average out over the third invariant timescale. Therefore, radial diffusion in modern radiation belt theory is treated as distinct from local processes (acceleration and loss), which are caused by wave-particle interactions violating the first and second invariants.

The relative importance of radial diffusion and local acceleration to high-energy radiation belt fluxes remained unknown for several years. It was eventually found from satellite data that a peak in PSD existed around L=4 that must have been caused locally, consistent with acceleration by chorus waves [e.g. Summers et al., 1998, Chen et al., 2006, Iles et al., 2006, Shprits et al., 2007]. Analysis of the Van Allen probes data by Thorne et al. [2013] provided more compelling evidence for local acceleration. In particular, flat pitch angle distributions that are a characteristic feature of chorus scattering at relativistic energies, further confirmed the role of chorus in electron acceleration. Recent work further confirms that chorus can accelerate electrons to highly relativistic energies [Li et al., 2014].

It is not easy to directly prove the existence of local acceleration even if satellites with particle detectors cross the heart of the radiation belts. The reason for this was outlined in [Reeves et al., 2013]: both radial diffusion and local acceleration can produce apparent peak fluxes in energetic electrons around the same radial distance. To demonstrate this problem, consider Figure 2 which is a simulation using the Versatile Electron Radiation Belt (VERB) code [e.g. Shprits et al., 2007]. The code itself will be described in more detail later in the appropriate sections, but for now it is sufficient to say that it is a radiation belt modelling tool that simulates radiation belt electron phase space density evolution as a consequence of various processes. Phase space density profiles can

then be converted to fluxes, as a function of L^*, energy, pitch angle and time. The code is designed such that radial diffusion, local acceleration and pitch angle scattering by various wave modes, as well as mixed diffusion terms, can be turned on and off. The code requires information about electrons injected or convected from the outer boundary and also about geomagnetic activity in the form of the Kp index. In this test, the flux from the outer bounday is set at a constant value, and Kp is also set to a constant value (Kp=3). Figure 2 (a) shows the flux profile of 1 MeV electrons. It can be seen that flux builds up with time with the peak coming closer and closer in radial distance. The reason for this is that, as electrons from the outer boundary diffuse inwards, they gain energy through conservation of their first invariant, so fluxes of energetic electrons accumulate with the effect reflected in the figure. Figure 2 (b) shows the same set-up but with local acceleration, pitch angle scattering and mixed terms turned on as well as radial diffusion. Fluxes do not build up at the lower L^* values as they are locally scattered by waves such as chorus and plasmaspheric hiss, but apart from that the profile looks similar, with the same peak in 1 MeV fluxes around L^*=4-5 as evident in Figure 2 (a).

To discern the difference, fluxes must be converted to phase space density which is flux divided by the square of the electron momentum. Figures 2 (c) and (d) show the PSD profiles for same set-up as in (a) and (b) respectively, where μ=3000 and J=0.01. Here, a developing peak in PSD around L^*=5 is evident in (d) that is absent in (c). In fact it can be seen towards day 15 on Figure 2 (d) that the PSD peak spreads outwards towards the outer boundary. This scenario - local acceleration of electrons at L^*=4-5 to relativistic energies and their subsequent outward radial diffusion to GSO - has been observed by satellites [e.g. Reeves et al., 2013, and references therein].

There exist several wave types capable of violating the first and second invariants of ions and electrons via resonant wave-particle interaction. The whistler wave mode and its ion equivalent - the electromagnetic ion cyclotron (EMIC) wave - can resonate with radiation belt electrons via the first invariant (gyration), leading to momentum change. A transfer of energy from the wave to the particle via resonance does two things: changes the particle's total velocity (energy diffusion) and the ratio of the particle's parallel and perpendicular momenta (this is known as pitch angle diffusion). Summers et al. [1998] constructed diffusion curves for whistler and EMIC waves for a range of representative storm-time magnetospheric plasma parameters. It was found that significant electron energy diffusion can occur via electron resonant interaction with whistlers, leading to a 'pancake' pitch angle distribution where high pitch angles predominate. L-mode EMIC waves meanwhile do not diffuse in energy but can be an effective pitch angle diffusion mechanism for high-energy $>$ 1 MeV electrons. Pitch angle diffusion or scattering can change the mirror points of the affected electrons. If the new location of the mirror points is such that they are in the atmosphere, these particles are lost from the system. The solid angle of minimum pitch angle value at which this happens is called the 'loss cone'. Thereby the following mechanism was proposed for relativistic electron flux dynamics during a storm:

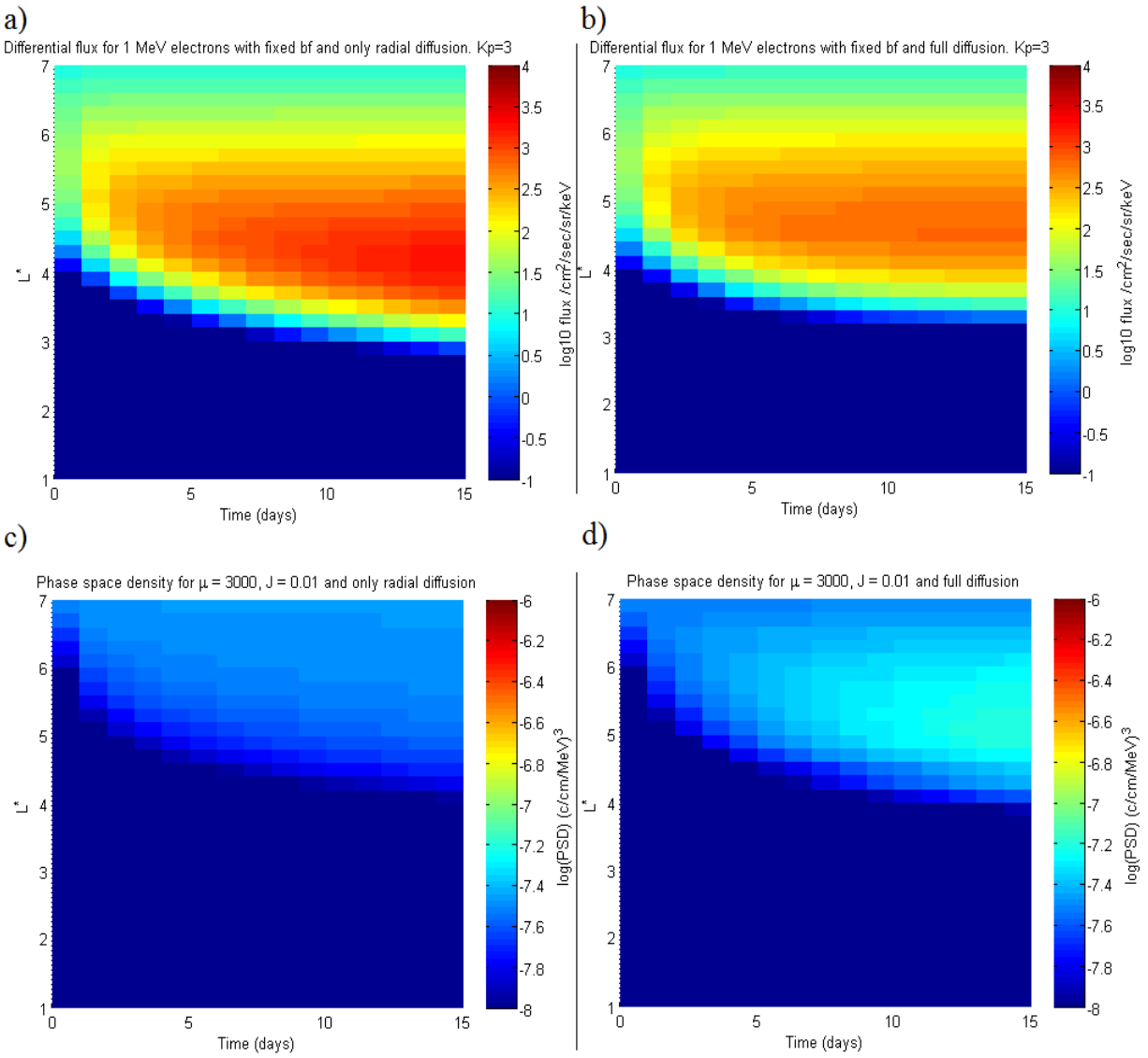

Figure 2: A comparison of flux and PSD profiles for radial diffusion only vs. radial diffusion and local processes. a) Differential flux vs. time vs. L^* for 1 MeV electrons with bf=1 and Kp=3 for 15 days with only radial diffusion turned on, b) the same but with local acceleration, pitch-angle scattering and mixed terms, c) PSD profile for electrons with μ=1000 and J=0.01 with only radial diffusion and d) PSD profile for electrons with the same invariant values with local acceleration, pitch-angle scattering and mixed terms.

1. During the main phase, increased EMIC activity would pitch-angle scatter relativistic electrons into the loss cone, leading to rapid flux depletion [e.g. Summers and Thorne, 2003]. At the same time, increased convective/substorm activity would bring both electrons and ions inwards from the tail into the radiation belt environment, increasing their anisotropy in the process. Ion anisotropy via substorms would generate increased EMIC waves.

2. Electron anisotropy would relax in the form of the whistler-mode instability, leading to increased chorus wave activity. Whistlers would diffuse the convected electrons in energy, accelerating them from a few 100 keV to relativistic energies. EMIC waves would pitch-angle scatter the accelerated electrons, and thus a combination of the two wave modes would act to reproduce the observed energetic electron dynamics [e.g. Summers and Ma, 2000a]. Other processes were also considered to be capable of acceleration of seed electrons to relativistic energies, for example fast magnetosonic waves [Summers and Ma, 2000b].

The basic ideas behind the above scheme form the foundations of most physics-driven radiation belt models today. Wave activity is parameterised by geomagnetic indices, and radiation belt dynamics are predicted as largely a combination of large-scale radial diffusion, as well as local loss and acceleration processes driven by wave-particle interactions.

1.6 Geomagnetic indices

To provide a measure of the activity of magnetosphere as a whole, several geomagnetic indices have been devised. Many radiation belt model coefficients are parametrised by these indices, as statistical studies have shown that plasma waves, radial diffusion rates and substorm activity are all related to one or more of them. Roughly speaking, they all provide a measure of the activity of the magnetosphere. Different geomagnetic indices provide different quality measures of various processes that occur in the magnetosphere, so it is useful to select more than one when evaluating a particular magnetic disturbance or chain of events. Models and functions have been developed to empirically predict geomagnetic index values based on L1 solar wind data [e.g. Wing et al., 2005, Borovsky, 2014].

Dst index

The Disturbance Storm Time or Dst index is an hourly measure of geomagnetic activity derived from a network of low-latitude magnetic observatories around the world. It was devised to observe the 'ring current' around the Earth which forms during storm times as new particles are injected into the near-Earth environement. The development and later decay of the ring current, manifested in a change of electric potential, induces a southward magnetic pressure on the Earth's dipole that is registered by low-latitude magnetometers. However, as pointed out by Campbell [2004], this is an oversimplification and in fact other current systems significantly influence this geomagnetic index. Nevertheless it is a very good tool for assessing the overall geomagnetic field disturbance activity and generating storm recovery time predictions. Storms analysed by the Dst

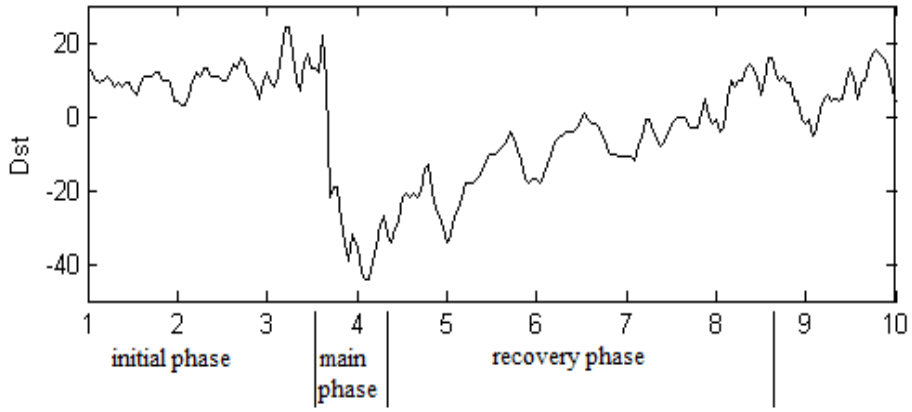

Figure 3: The Dst index for 1-10 August, 2013. The approximate initial, main and recovery phases of the magnetic storm are labelled on the diagram. The x-axis is in days.

index follow a classic three-stage profile: an "initial phase" characterised by a positive index, then a "main phase" drop to a negative potential, and finally a "recovery phase" where the potential slowly returns back to its original value near zero. An example of all three stages can be seen in a sample storm on Figure 3 using OMNIWeb data. The main-phase Dst drop can occur as a consequence of both magnetospheric compression by a solar wind stream, and the build-up of the ring current [Desorgher et al., 2000]. Solar wind data and B_z orientation from L1 usually give a fuller picture of events than the geomagnetic index alone.

Sym-H index

The Sym-H index is calculated in a very similar manner to the Dst index, the main differences being that it uses different ground stations for its input data (some of which are at higher latitudes), and it has a 1-minute time resolution as opposed to 1-hour as for the Dst index. The Sym-H index exhibits variations compared to the Dst index (as a result of different data processing, different input groundstations and greater visibility of transient electric and induced magnetic fields). Nevertheless, Wanliss and Showalter [2006] after comparing the two indices found that, for most geomagnetic conditions, the Sym-H index can be safely used as a de facto high-resolution Dst index with no significant loss of accuracy.

AE index

The Auroral Electrojet or AE index is obtained from a number of relatively high-latitude magnetometer stations [Davis and Sugiura, 1966] which measure the north-south magnetic perturbation. It is composed of the difference between two indices, the AU index which measures the maximum positive excursion of the perturbation, and the AL index which measures the maximum negative

excursion. It is an indicator of substorms, which are believed to be caused in the tail by magnetic reconnection and lead to a dipolarisation of the magnetosphere and an influx of new particles into the radiation belt region.

Kp index

This index, released every 3 hours, is calculated from the K-index which is a measure of the horizontal magnetic field fluctuations from 13 sub-auroral magnetometer ground stations. Local time and seasonal effects are calculated and the measurements are standardised such that they are self-consistent. This forms the basis of the Kp index. As such, while the Dst index measures mostly low-latitude effects and the AE index takes measurements from the auroral zone, the Kp index is somewhere in between. In theory this means that this measurement is able to assess the state of the magnetosphere in general. The problem with this measurement is that, while self-consistent, it does not represent any physical variable. Nevertheless it is widely used in radiation belt forecasting models and, because of its high correlation with the solar wind, models driven by solar wind parameters predict the Kp index for 1 and 4 hours ahead [e.g. Wing et al., 2005].

1.7 Novel contributions

This section summarises the novel research and development that has been made during the course of the PhD.

- A new radiation belt simulation and prediction model has been developed. It combines data-driven and physics-driven approaches, and can be considered as one evolution of the UCLA Versatile Electron Radiation Belt (VERB) code [e.g. Shprits et al., 2007]. The VERB code predicts radiation belt fluxes across the outer belt region, but needs input from the outer boundary to model injections of new particles. This information is provided from Nonlinear AutoRegressive Moving Average with eXogenous inputs (NARMAX) predictions of energetic fluxes at geosynchronous orbit, that have been translated to the outer boundary space of VERB. The resulting system - dubbed VERB-NARMAX Coupling or VNC - has been successfully tested for a range of geomagnetic conditions, simulating a range of representative storms. A variation on the system, called VNC-S or 'VNC-Scaled', which exhibits superior performance at geostationary orbit, has also been detailed and tested. Scientifically interesting information that is deduced as a result of the model development and performance is identified and discussed.

- Wave vector identification has been performed on an EMIC triggered emission to calculate its dispersion relation. The calculated dispersion relation was found to correspond to the cold plasma dispersion relation calculated using plasma parameters observed or inferred at the time of the event. Minimum resonant energies of EMIC wave events have been calculated using the methodlogy outlined in Silin et al. [2011a]. Special attention has been paid to a specific subset of the EMIC instability - triggered emissions - where particularly high wave numbers are observed. The overall goal was to find out if this wave mode affects radiation belt dynamics below 1 MeV. The conclusions are that under normal

conditions, EMIC wave minimum resonant energies are higher. However, one emission observed in the cusp exhibited much lower energies and, analysing the ambient plasma conditions, it is plausible to imagine a situation where EMIC waves may be generated in the magnetosphere by triggered emissions with < 1 MeV minimum resonant energies.

1.8 Thesis outline

The thesis is organised as follows. Chapter 2 presents an introduction to VNC, starting with a literature review of first data-driven prediction methods, including NARMAX, and then a discussion of physics-based systems. The Versatile Electron Radiation Belt (VERB) code is described in some detail, and a discussion regarding the joining of the NARMAX and VERB code occupies the rest of the section.

Chaper 3 presents the results of the combined system, first analysing representative time periods, then studying the model performance for low and high energies. An analysis is made of the scheme itself by taking NARMAX predictions out of the system and replacing them with actual empirical data. The chapter concludes with long-term modelling of the radiation belts using VNC and a short study of the effects of changing wave model parameters on the output.

Chapter 4 describes the VNC-S or 'VNC-Scaled' model. A description of the methodology is followed by an in-depth analysis of model performance using different magnetic field models. A direct comparison is made between VNC and VNC-S, and the study finishes with long-term modelling of the VNC-S system.

Chapter 5 is devoted to the analysis of EMIC waves. Starting with a discussion of the historical search for minimum resonant energy for this wave type, wave vector analysis is performed on an EMIC triggered emission to calculate minimum resonant energies. The same analysis is then performed on another EMIC event observed at the cusp.

Chapter 6 contains the conclusions obtained from the work carried out in the previous chapters. Recommendations for the improvement of VNC and VNC-S are includeed, as well as a discussion on the role of EMIC waves from the analysis of two observations by the Cluster mission.

2 Chapter 2: Radiation belt modelling

A new system for radiation belt simulation and prediction has been developed and tested. The VNC (VERB-NARMAX Coupled) algorithm is a collaboration between the University of Sheffield and the University of California, Los Angeles. The scheme represents a fusion of data-driven and physics-driven methodologies with the goal of providing the most accurate radiation belt prediction possible over a wide operational range. Several variations of the methodology produce valid results for various parameter ranges. This chapter outlines the operation and design of the constituent subsystems, as well as the various schemes to couple the subsystems together.

2.1 Data-driven prediction methodologies

Below follows an overview of data-driven radiation belt prediction systems in use or development today. Most of them use geostationary orbit satellites, which provide near-continuous data output, and perform various data analysis techniques on that data. Usually this is correlated with solar wind data from satellites at L1. Various geomagnetic indices may also be used.

Some of the earliest work on predicting highly energetic radiation belt fluxes was done by [Nagai, 1988]. The authors started with a superimposed epoch analysis to find that flux minima correspond with local maxima in Kp index and local minima in Dst index. The authors then used linear prediction filter (LPF) analysis to characterise and predict the general relationship between high-energy electrons with the Kp index. The study found that they could reproduce the increase-decrease sequences well, but the quantitative agreement was unsatisfactory in some cases.

Baker et al. [1990] also used the linear prediction filter to analyse energetic (mostly 3-5 MeV) electron fluxes with the Kp index, AE index and solar wind velocity. That study found that all three inputs were well-correlated with energetic electron flux and a rise in all of them corresponded to a rise in relativistic electron fluxes around 2-3 days afterwards. The authors noted that the impulse response function for energetic electrons exhibited a sharp drop at the time of Kp, AE and solar wind increase, followed by a rise in particle flux around 2-3 days later. The authors found that the system could predict when a rise or fall in flux would occur, but the magnitude of the electron increase was less certain. The study also found that electron variation corresponded with the 27-day solar cycle, and that the relationship between Kp index and electron flux was not time stationary, not linear and that other factors were probably involved in flux variations than those responsible for causing Kp enhancements. Prediction efficiency, defined as $1 - \frac{MSE}{VAR}$ where MSE is mean squared error and VAR is the variance of the data, was found to be 52%. This is similar to findings of Reeves et al. [2003] who found that in about 50 % of magnetic storms, fluxes tend to increase.

Koons and Gorney [1991] used a neural network to investigate high-energy (> 3 MeV) fluxes observed at GSO. The authors found that, when trained using

ΣKp for 10 consecutive days, the model produced much better results than the linear prediction filter during periods of high fluxes. This allowed the authors to devise a forecasting scheme for electron fluxes and to reconstitute fluxes when no data was available. The model was able to account for the observed variation using only the Kp index and without resorting to data such as the Jovian synodic year, which has been suggested as a factor before [e.g. Friedel et al., 2002, and references therein].

Ukhorskiy et al. [2004] developed an empirical model driven by multiple solar wind and magnetospheric inputs, combining the deterministic approach of nonlinear dynamics with conditional probability considerations. The model was used to generate 1-day predictions of daily flux maxima. The authors argued that the flux maxima are more important than average daily flux values from a satellite protection standpoint. The model was validated using GOES-7 and 8 satellite data for > 2 MeV electron fluxes for the years 1995-2000. The deterministic part of the model yielded an average prediction efficiency of 0.77. Wind velocity and $SymH$ were identified as the most relevant input parameters.

Lyatsky and Khazanov [2008] obtained very high correlation coefficients (around 0.93) between observed and predicted GSO fluxes by using two linked continuity equations with source and loss terms parametrised by solar wind measurements. The study, among other things, made the loss term proportional to solar wind density. It was assumed that penetration of solar wind plasma into the plasma sheet may lower the Alfven velocity and provide favourable conditions for EMIC wave generation. This is mirrored in the findings of NARMAX [Balikhin et al., 2011, Boynton et al., 2013] which also reported density as the main control parameter for highly energetic electron fluxes.

Turner and Li [2008] took advantage of a time delay in flux variations between different energy channels at GSO satellites to create a very effective model for forecasting one day in advance. The study noted that flux variations were detected at lower energy channels first, and only later translated into variations of relativistic electrons. Both radial diffusion and local acceleration were proposed as potential explanations. As well as low-energy electrons being chorus-accelerated towards ever higher energies (an assumption used in the aforementioned Lyatsky and Khazanov [2008] study), radial diffusion also affected low-energy electrons faster; as such they could effectively serve as a warning of a higher-energy tail of the population arriving. The delays were found to be on the order of up to 37 hours, decreasing as higher energy channels were examined. The model was able to achieve prediction efficiencies of over 80 % depending on the solar cycle. The model only used GSO satellite data as an input, which was seen as an advantage since it could continue generating predictions if data from L1 ceased.

Burin des Roziers and Li [2006] used statistical asynchronous regression (SAR) analysis to map electron fluxes from magnetic noon to any other MLT using statistical electron flux data from LANL satellites. Once the MLT flux profile was established for a number of solar wind conditions, it was possible to generate an MLT-dependent prediction of fluxes using GSO satellites and L1 data (solar wind velocity). Apart from times when magnetopause shadowing

affected results, the predicted fluxes were found to be in good agreement with observations. Prediction efficiency was found to be higher near magnetic noon than near magnetic midnight, due to larger variance of observed fluxes at magnetic noon and larger uncertainties around magnetic midnight. Due to constant stretching and dipolarisation of field lines at magnetic midnight, the L-shells the satellite crosses vary much more, and this degrades model accuracy. Nevertheless, the model provided good agreement with observations in all MLT sectors. This is one of the relatively few data-driven models that attempt to generate MLT-dependent predictions, rather than averaging out the diurnal electron flux variation.

O'Brien [2009] used statistical satellite anomaly data together with geomagnetic indices and fluxes of high-energy protons and electrons derived from particle detectors aboard GSO and near-GSO satellites to create algorithms that generate alerts of various types of operational anomalies. The alerts used a simple-to-understand colour scale (red, yellow and green) and were developed for surface charging, internal charging, single-event upsets and power degradation to solar arrays due to irradiation by high-energy particles. The study warned against over-generalising the system output, since each satellite has its own specifics, but aimed to provide general purpose information to a variety of users which the operator would tailor to their own system.

Ling et al. [2010] designed a neural network prediction system developing on the aforementioned Koons and Gorney [1991] model. The new model was trained using 2 years of > 2 MeV electron data from the GOES satellites, and the network was re-trained daily to improve performance. The system was found to have prediction efficiencies of 0.71, 0.49 and 0.31 for 1, 2 and 3-day forecasts respectively and was able to forecast electron flux during intense events such as the 2003 "Halloween" storm. The model did not use solar wind data as an input, instead using 10 days of consecutive previous flux and 7 consequtive days of past summed Kp index. It was postulated that, since the model performance in terms of its prediction efficiency was found to depend on the solar cycle phase, the solar wind data contains important information and would improve model performance if included as an input.

Sakaguchi et al. [2013] used a Kalman filter with a multivariate autoregressive model to forecast > 2 MeV electron fluxes, with solar wind speed, B_z and solar wind pressure as input variables. By combining the three variables, the system was able to achieve prediction efficiencies and forecast lead times superior to when any one input is used in isolation. The study was thus able to achieve prediction efficiencies of 0.72, 0.51 and 0.35 for forecasts 1, 2 and 3 days ahead respectively, for the time period 1999-2000. Overall, the model was found to perform better during solar cycle minimum than solar maximum, but the prediction efficiency for 1 day ahead was always maintained at over 69 % throughout the solar cycle. The study reproduced the 27-day autocorrelation maximum found by Baker et al. [1990], as well as two-day lags between solar wind variation and relativistic flux changes at GSO. By subjecting the model to test inputs, the authors found that solar wind speed increase causes a flux rise, a solar wind speed increase together with a southward B_z IMF causes a larger

flux enhancement (while a northward B_z reduces the effect of the solar wind velocity increase on fluxes), and that a pressure increase leads to a decrease in electron flux.

Su et al. [2014] used data from GOES satellites to predict fluxes > 2 MeV. The study shows that the most important factor affecting flux variation is the magnetic local time (MLT). They describe the variation in MLT using Gaussian fits parameterised by different Kp index values. Then, by taking flux values from active GOES satellites at particular MLT locations, they are able to predict fluxes anywhere at GSO. Prediction efficiency is good for Kp < 5 and falls off at higher geomagnetic activity values. High geomagnetic activity is associated with flux dropouts which means that flux variations may no longer be represented by the Gaussian fits. This is generally an issue affecting all radiation belt prediction models.

In data-based prediction, probability distribution functions (PDFs) have been successfully employed. A good example is the Geosynchronous Radiation-belt Electron Empirical Prediction (GREEP) model Kellerman et al. [2013], which uses PDFs derived for electron flux of various energies as functions of solar wind velocity and density [Kellerman and Shprits, 2012]. The model also employs *recurrence* (utilising time-lags and cross-correlation to locate cyclic phenomena related to solar rotation), and *presistence*, which predicts fluxes based on the difference between past days. The three flux predictions (PDF-based, recurrence and persistence) are combined together with a weighting generated for each one, based on how well it (independently) performed against real data for the current day. The weightings are updated dynamically. This allows the system to adapt to varying solar wind conditions: for example, at times of low solar activity, where fluxes are steady, the persistence would be expected to weigh more; during time periods of pronounced cyclic solar activity, recurrence should weigh more etc. Thus the model was able to provide good predictive performance for various stages of the solar cycle.

Multiple regression analysis has been performed on LANL satellite data to both devise a predictive model and to look for physical mechanisms responsible for flux variation [Simms et al., 2014]. Over two hundred storms were selected and statistically analysed, with the work focusing on storms specifically and omitting quiet time periods. The study found that many of the variables currently used as inputs are inter-correlated (for example, density and velocity both contribute to pressure; the Kp index is an indicator for a wide range of processes like ULF intensity). The study focused on isolating variables that are most predictive of flux when other variables are controlled. In decreasing influence, ULF, seed electron flux, solar wind velocity and its variation, and after-storm B_z were found to be the most significant variables accounting for flux variation.

2.2 NARMAX model description

NARMAX (or Nonlinear AutoRegressive Moving Average model with eXogenous inputs) is a data-driven methodology [Billings et al., 1989] that has been used to study nonlinear dependencies of the dynamics of the magnetosphere [e.g.

Boaghe et al., 2001, Balikhin et al., 2001, Boynton et al., 2011, 2013]. In this scheme the output at time t is a scalar value that is assumed to be a function of previous values of inputs $u(t)$, output $y(t)$ and error terms $e(t)$ as described by the equation:

$$\begin{aligned} y(t) = F[&y(t-1), ..., y(y-N_y), \\ &u_1(t-1), ..., u_1(t-n_{u_1}), ..., \\ &u_m(t-1), ..., u_m(t-n_{u_m}), \\ &e(t-1), ..., e(t-n_e)] + e(t) \end{aligned} \tag{10}$$

where $F[\cdot]$ is some nonlinear function, y, u and e are output, input and error terms, m is the number of inputs to the system and $n_y, n_{u1}, ..., n_{um}$ and n_e are the maximum time lags of the output, the m inputs and error, respectively.

In this study, NARMAX is used to predict integral electron fluxes for the next 24 hours given data from two GOES-13 satellite channels for detecting $>$ 800 keV and $>$ 2 MeV and solar wind parameters from L1. The output is in the form of fluxes of $>$ 800 keV and $>$ 2 MeV electrons in units of $n_e/day/cm^2/sr$. Predictions for these electrons are used as the boundary flux input to the VERB code. This lower-energy channel is chosen because electron behaviour at above 1 MeV differs significantly as other dynamics start to predominate [Shprits et al., 2013].

2.3 Physics-based diffusion codes

Li et al. [2001] developed one of the first radiation belt prediction models based on the Fokker-Planck equation for diffusion. Only radial diffusion was used, and solar wind data from L1 was the input. The equation was taken from Schulz and Lanzerotti [1974]:

$$\frac{\partial f}{\partial t} = L^2 \frac{\partial}{\partial L}\left(\frac{D_{LL}}{L^2}\frac{\partial f}{\partial L}\right) - \frac{f}{\tau} \tag{11}$$

where f was the electron phase space density, related to differential flux j by $f = j/p^2$. A grid was set up with the inner boundary at L= 4.5 and the outer boundary at L=11, considered to be the last closed drift shell before the average magnetopause location. The diffusion coefficient was a function of the L-shell ($D_{LL} = D_0(L/6.6)^{10}$) as was the electron lifetime term ($\tau = \tau_0(6.6/L)^{10}$). The coefficient D_0 was an empirically derived function of three parameters: solar wind velocity, B_z orientation and the variation of solar wind velocity. All three factors were normalised by their averages using two years of L1 data, and all had weighing functions such as to most closely mimic MeV electron data from LANL satellites. Despite the fact that this model heavily relied on statistical data for its key parameters, it is still considered a physics-based model in this manuscript, since it was built on physical principles and aimed to give physical explanations for observed relationships.

The study was able to accurately model high-energy (> 700 keV) electron flux at GSO for over a year of data. The study claimed that, since solar wind variations take some time (on the order of 2 days) to propagate to GSO from the outer boundary, the MeV electron flux can be predicted 1-2 days after a solar wind change is detected at L1. This was the physical explanation for the 1-2 day delay observed between peaks of solar wind velocity and peaks in high-energy GSO flux.

The SPACECAST forecasting system [Horne et al., 2013] features two independent models - BAS and ONERA. The general design of these models is to use a diffusion equation to describe radial transport from/to the outer simulation boundary and local acceleration/loss diffusion coefficients due to plasma waves, with an additional non-diffusive term to simulate atmospheric losses. The outer boundary is parametrised by the Kp index using CRRES statistics. As such, the Kp index forms the only input to this system. Another feature is that the GOES satellite orbit in L^* is predicted using a model that does not depend on the Kp index (for example in Figure 5, top, in paper, the location of the satellite, denoted by the white line, only shows diurnal variations without changing as the Kp index is varied). In contrast, as shall be explained below, the VNC uses a magnetic field model that does depend on the Kp index to calculate GOES satellite location in L^*. The effects of using different field models is investigated and discussed in the appropriate section below.

There are both advantages and disadvantages in using one geomagnetic index driver for the whole system. On the plus side, using one input certainly gives the system generality and with several sources of Kp index forecasting, the system continues to generate self-consistent predictions even if one input fails. The Kp index, as discussed above, is quite a universal measurement, implicitly accounting for a whole range of space plasma dynamics. Injections and dipolarisation, magnetospheric compression and wave activity are all corellated with this parameter. However, in itself it has no physical meaning and it is difficult to isolate individual events from the Kp index alone. This undoubtedly has a negative impact on the results - if the outer boundary is simply parametrised by the Kp index, there will be no way to differentiate, for example, compression (and plasmapause shadowing) events from substorm events, since both will cause the Kp index to rise. As was noted in Reeves et al. [2003], increased geomagnetic activity only correlates with increased energetic fluxes about 50% of the time and in a significant amount of cases actually leads to flux reduction.

The STEERB (Storm-Time Evolution of Electron Radiation Belt) model [e.g. Su et al., 2011a] has a separate loss term for the slot region dependent on L and Kp index and in the cited study employs a time-varying Dst-dependent magnetic field model to investigate the influence of adiabatic transport on radiation belt dynamics. The design is similar to SPACECAST. A kappa distribution function of energy vs. flux is used instead of an empirically-derived distribution or a Maxweillian, which are used on other models. The model inputs are the Kp index, a user-defined outer boundary flux, as well as parameters such as Dst needed to drive the magnetic field model. The model is used to simulate magnetic disturbances through the storm onset, main and recovery phases, using

adiabatic transport, radial diffusion, chorus acceleration and scattering by hiss and EMIC waves. The Su et al. [2011b] study concludes that adiabatic transport alone cannot reliably reproduce the main-phase dropout often observed during magnetic storms in the presence of chorus acceleration. Nevertheless, adiabatic transport is able to cause significant depletion upwards of 5 R_E without significant chorus waves and enhances the effect of magnetopause shadowing because particle drift shells dilate as the ring current builds, and get transported to the magnetopause boundary. The study also concludes that adiabatic transport is coupled to non-adiabatic processes, for example transporting populations into parameter areas where they are likely affected by non-adiabatic processes. Ignoring adiabatic transport is found to generally produce overestimates of flux during the main phase and underestimates in recovery. Thus its effect is to confound the changes that occur during a 'classic' storm. This makes physical sense - as the initial storm impact compresses the magnetopause or builds the ring current, particles are 'temporarily' adiabatically transported out of the visibility of the detector. When the magnetic field returns to normal, these particles return again.

2.4 Implicit vs. explicit schemes for the diffusion equation

Radial diffusion and local acceleration are both modelled by the heat equation. The differential equation in VERB is obtained using the finite differences method [Subbotin et al., 2010] where the derivative is estimated by a series of small differences evaluated at consequent time steps. The evolution of a parameter at each time step is a function of its previous value at that parameter space, as well as the influence of values next to it. The simplest way of calculating the evolution of a variable is then the so-called forward time central space method (see Figure 4(a)). In the figure, j, n is the prior parameter value, $j-1, n$ and $j+1, n$ are two known (set) boundary conditions, and the required value at the next time step $j, n+1$ is obtained by

$$\frac{u_j^{n+1} - u_j^n}{k} = \frac{u_{j+1}^n - 2u_j^n + u_{j-1}^n}{h^2} \tag{12}$$

In this method, $u_j^{n+1} = (1-2r)u_j^n + ru_{j-1}^n + ru_{j+1}^n$ where $r = k/h^2$. The method is simple and fast, but becomes unstable when $r>1/2$. This is known as the Courant condition and places a limit on the size of the time step. When the limit is exceeded, errors accumulate rapidly and the prediction becomes invalid. Figure 5 demonstrates this using an abstract simulation. Here, a simulation space is set up with fixed outer boundaries (1 and 0) and both schemes are run for 300 time steps. This is supposed to represent diffusion of heat (or phase space density). On Figure 5 (a) it can be seen that the diffusion is simulated as expected, with 'heat' equal to 1 at the outer boundary and 0 everywhere else at t=0. As time goes on, heat diffuses from the boundary across the simulation domain until a steady state is reached around t=200, where the 'cold' top boundary balances the 'hot' bottom boundary and no net diffusion

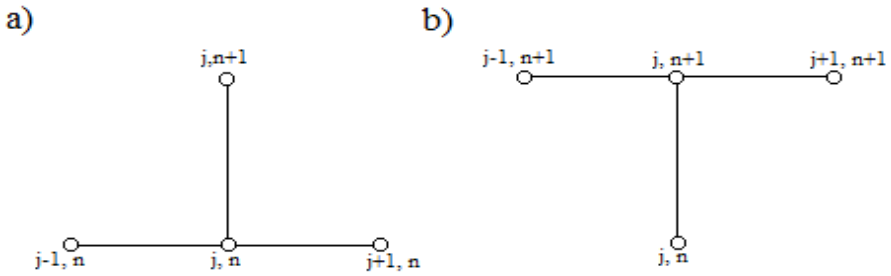

Figure 4: A stencil diagram showing a) the explicit and b) the implicit scheme.

takes place anywhere in the simulation domain. The parameter $r = \Delta t/\Delta h^2$ equals 0.25. The Courant condition is satisfied.

However, if the spacial resolution is increased (or the time step is increased), the explicit scheme fails. Figure 5 (b) shows the result of the same simulation as before but this time with Δh=0.7. It can be seen that the simulation becomes unstable as now $r = \Delta t/\Delta h^2 > 1/2$.

The implicit method, or backward-time central space, derives the value at the current time step using the previous value and boundary conditions at the current (not the previous) time step (see Figure 4 (b)). The equation for the implicit method is

$$\frac{u_j^{n+1} - u_j^n}{k} = \frac{u_{j+1}^{n+1} - 2u_j^{n+1} + u_{j-1}^{n+1}}{h^2} \tag{13}$$

The value for u_j^{n+1} can be obtained by solving a system of simultaneous equations:

$$(1 + 2r)u_j^{n+1} - ru_{j-1}^{n+1} - ru_{j+1}^{n+1} = u_j^n \tag{14}$$

this means that a system of simultaneous equations has to be solved at each time step. The matrix determinant calculation required for this means the process can take longer if the matrix is very large. However, the scheme is always stable, regardless of the size of the time step. It is this implicit scheme that is used in the VERB code. Figure 5 (c) and (d) demonstrate this. They are exactly the same as Figures 5 (a) and (b) but with the implicit method used instead of the explicit method. It can be seen that even with the lower Δh, the diffusion process is simulated successfully.

2.5 VERB model description

The Versatile Electron Radiation Belt (VERB) code [e.g. Subbotin et al., 2011b, and references therein] is a diffusion code that models radiation belt particle dynamics using the bounce-averaged Fokker-Planck equation [e.g. Schulz and Lanzerotti, 1974] with radial, pitch angle and energy diffusion:

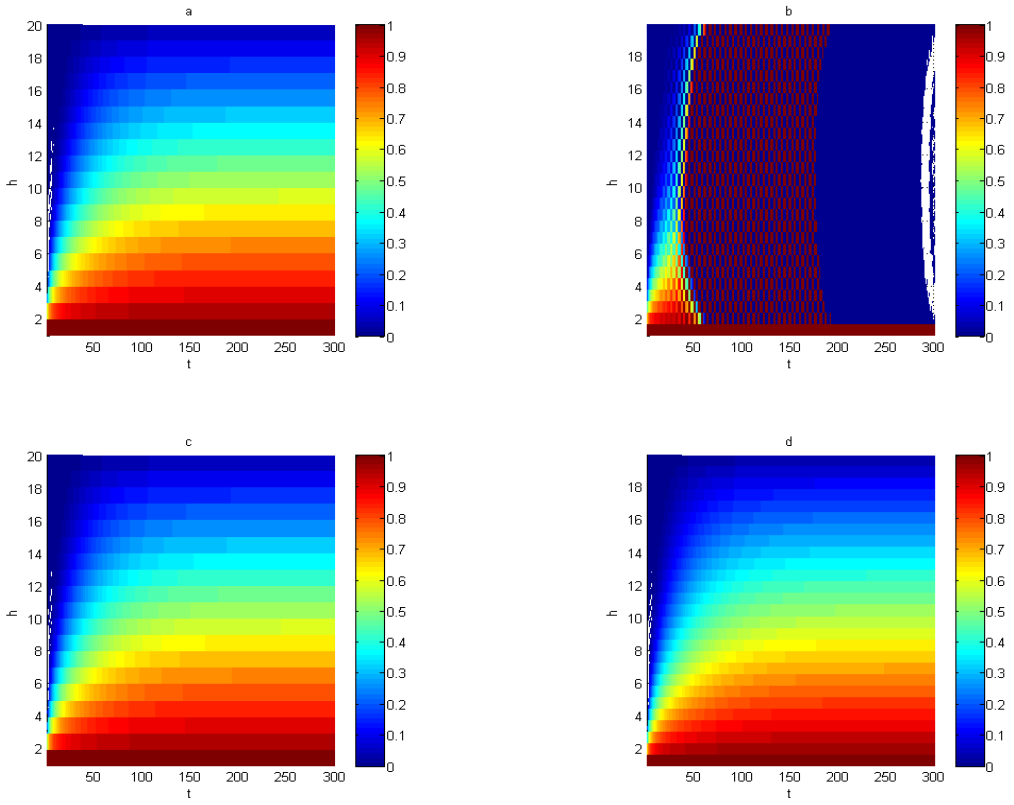

Figure 5: a comparison of the explicit and implicit schemes of the finite differences method for various spatial and temporal resolutions. Constant boundaries are set up in the simulation space vis. 0 at the top and 1 at the bottom for all time. The colour bar represents temperature (or phase space density) in arbitrary units. The y-axis represents the simulation space. The simulation is run for 300 time units. (a) the explicit scheme with Δh= 1 and Δt = 0.25. (b) the explicit scheme with Δh = 0.7 and Δt = 0.25. (c) the implicit scheme with Δh = 1 and Δt = 0.25, (d) the implicit scheme with Δh = 0.7 and Δt = 0.25.

$$\frac{\partial f}{\partial t} = L^{*2}\frac{\partial}{\partial L^*}\bigg|_{\mu,J}\frac{1}{L^{*2}}D_{L^*L^*}\frac{\partial f}{\partial L^*}\bigg|_{\mu,J} + \frac{1}{p^2}\frac{\partial}{\partial p}\bigg|_{\alpha_0,L}$$
$$\cdot p^2\left(D_{pp}\frac{\partial}{\partial p}\bigg|_{\alpha_0,L}f + D_{p\alpha_0}\frac{\partial}{\partial \alpha_0}\bigg|_{p,L}f\right) + \frac{1}{T(\alpha_0)sin(2\alpha_0)}\frac{\partial}{\partial \alpha_0}\bigg|_{p,L} \tag{15}$$
$$\cdot T(\alpha_0)sin(2\alpha_0)\left(D_{\alpha_0\alpha_0}\frac{\partial}{\partial \alpha_0}\bigg|_{p,L}f + D_{\alpha_0 p}\frac{\partial}{\partial p}\bigg|_{\alpha_0,L}f\right) + \frac{f}{\tau}$$

here, f is the electron phase space density, t is time, p is relativistic momentum, α_0 is equatorial pitch angle, and L is McIlwain's magnetic shell parameter (radial distance from the centre of the Earth to the equatorial fieldline point). L^* is the Roederer parameter, which is what the McIlwain parameter would be if the real magnetic field were translated to a dipolar condiguration. This distinction will be expanded on below. Radial diffusion is represented by the first term on the right-hand side of the equation, while diffusion in energy (momentum), pitch angle and mixed terms are represented by the next four. The three adiabatic invariants are represented by

$$\mu = \frac{p_\perp^2}{2m_0B} \tag{16}$$

$$J = \int_{bounce} p_\parallel ds \tag{17}$$

$$\Phi = \oint_{drift} BdS \tag{18}$$

$T(\alpha_p)$ in (1) is a function related to the bounce frequency and is approximated by Lenchek et al. [1961]

$$T(\alpha_0) = 1.3802 - 0.3198(sin\alpha_0 + sin^{1/2}\alpha_0) \tag{19}$$

Losses to the atmosphere are represented by the last term f/τ where τ is a characteristic electron lifetime assumed to be infinite outside the loss cone and equal to a quarter bounce time inside it. All tensors are parameterised by Kp index either explicitly or implicitly through plasmapause location. They are bounce- and MLT-averaged and data on wave-particle interactions is drawn from statistical studies. The radial diffusion term is parametried by the Kp index following [Brautigam and Albert, 2000]:

$$D_{L*L*} = 10^{0.056Kp-9.325}L^{*10} \tag{20}$$

The wave model uses three wave types: dayside chorus, nightside chorus and plasmaspheric hiss. Parameters for the first two can be found in [Subbotin et al., 2011b], while the parameters for plasmaspheric hiss are taken from [Orlova et al., 2014].

The important point to note is that the VERB code runs on two inputs: the Kp index and a quantity called 'boundary flux'. While the Kp index is a well-established quantity in the geophysical community, the boundary flux represents the flux (as a function of energy) that would be observed at the outer boundary (usually $L^* = 7$) with a particle detector, normalised by a statistical measure of flux obtained from statistical satellite observations. In essence it is a measure of particle injections and convection from the magnetotail, that provides the source and seed populations which the Kp-parametrised processes then act upon. This quantity is impossible to measure in real-time. First, $L^* = 7$ is not a fixed point in space, and second, even if it was, it is usually outside geosynchronous orbit and so the satellite cannot be stationary there. As such it is necessary to infer it to various degrees of accuracy. The picture is complicated by the fact that, although injected particles are believed to come from the tail (MLT ≈ 0), the early versions of VERB that are used in VNC are MLT-independent, with all MLT-dependent parameters such as plasma waves averaged [e.g. Shprits et al., 2009].

2.6 L vs. L^*

At this point it is useful to clarify a distinction in one key parameter used in the simulation. In radiation belt and space plasma physics literature, a commonly used measurement is the L-shell or McIlwain parameter. To calculate it, a field line must be traced to the magnetic equator. The distance from that equatorial point to the Earth's centre (in R_E) is the L-shell. For example, an L-shell of 4 defines a field line that would cross the magnetic equator 4 R_E from the centre of the Earth. It is useful for mapping field lines across different latitudes along which trapped electrons and plasma waves propagate. Magnetometer stations placed at field line footpoints at high latitudes can thus observe waves that have been generated equatorially and pinpoint at which distances they were created.

L^*, also known as the Roederer L^* [Roederer, 1970] is given by Equation (1) and represents the radial distance in R_E to the equatorial points of the (symmetric) shell on which the particles would be found, if we adiabatically turned off all the nondipolar perturbations of the trapping field.

$$L^* = \frac{2\pi M}{\Phi R_E} \tag{21}$$

Thus if the magnetic field were a perfect dipole, the McIlwain L and Roederer L^* would be identical. VERB uses L^* in its calculations because it is specifically related to the third invariant. To understand the effects of compression on L^*, consider Figure 6. The left side demonstrates a dipole magnetic field, such as would be observed under quiet magnetospheric conditions or right after a dipolarisation event. Here, L^*=4 and L^*=7 are both azimuthally equidistant from the Earth. Meanwhile, the figure on the right shows a more realistic magnetic field configuration - a compressed dipole - that becomes more pronounced during high solar wind pressure events. The effect of magnetospheric compression is to increase the flux density on the dayside, so that L^*, which is really

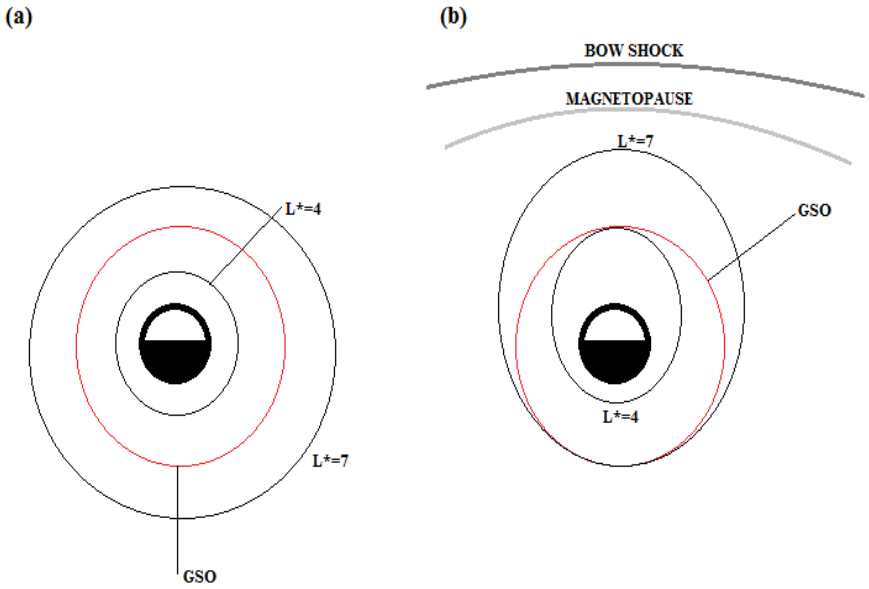

Figure 6: Different L^* values in relation to Earth and GSO location in (a) a dipole, and (b) a compressed dipole (for example, following a solar wind compression event). The direction of the Sun is upwards on the diagrams.

an equipotential magnetic field strengh contour, increases on the dayside. In other words, because of the greater magnetic flux density, the same magnetic field strength can be observed further away from Earth than on the nightside. As a result, it can be seen that GSO now cuts across different L^* regions. Since the energetic particle flux on some L^* is greater than on others (the heart of the outer radiation belt is located around L^*=4-5), as the spacecraft orbits the Earth, a diurnal variation in particle fluxes can be observed, with the peak fluxes occuring at magnetic noon.

2.7 Outer bounday flux

The outer boundary is defined as the limit of particle stable trapping [e.g. Schulz and Lanzerotti, 1974] where particles complete a full drift period and their dynamics could be described by invariant theory. For radiation belt models that do not distinguish between MLT sectors, such as the version of VERB under study, the outer boundary is a source of new matter and energy into the system, where 'seed' particles carried by the E x B drift are injected into the magnetosphere. In theory the outer boundary (on the dayside) is also a particle sink due to magnetopause shadowing, but the current version of VERB does not differentiate between different MLT sectors.

In previous studies, when VERB was used to evaluate the effect of various

processes on radiation belt dynamics, outer boundary information was extracted from CRRES data [e.g. Kim et al., 2012]. While this was adequate for simulations, it was not suitable for generating predictions. Other methods involved coupling VERB to a convection code [Subbotin et al., 2011a]. In VNC, the outer boundary is represented by high-energy fluxes observed at geostationary orbit, or rather, NARMAX predictions of them. Assuming exponential fits, it is possible to calculate differential flux from two integral energy channels. There are several problems with this approach. First, NARMAX outputs fluxes in units of particles $cm^{-2}sr^{-1}day^{-1}$ with predictions generated every 24 hours. With no hourly flux predictions, it is impossible to distinguish the relative contribution from different MLT sectors. The second problem is that high-energy channels are used ($>$ 800 keV and $>$ 2 MeV) that were initially designed to predict for killer electrons. These are not ideal energies with which to model convection, since the convection process will not generate energies as high as 800 keV. NARMAX fluxes could be either locally accelerated particles that have radially diffused outwards to GSO or a high-energy tail of a population injected in from the magnetotail by intense transient acceleration events. Thirdly, fluxes observed at GSO would have to be projected to the outer boundary (set to L^*=7). But the location of the outer boundary varies with magnetic local time, for reasons shown earlier. Thus without MLT information there is no obvious way to know which L^* to trace from.

It is possible to envision a modified NARMAX prediction system that could be used as a measure of particles entering from the tail. Such a system would generate predictions every hour, or only for time periods when the satellite would be between, for example, 2200-0200 MLT. This would make it possible to assume that the electron fluxes picked up by the satellite (especially if lower-energy channels are used as inputs) do originate from the tail. Local acceleration is negligible around the magnetic midnight sector due to relatively low wave intensity. Populations could theoretically be brought in via drift from the dayside, and be picked up by GOES-13 particle detectors. It may be possible to distinguish them from injected particles via their pitch-angle distributions, especially during periods of high solar activity. Magnetopause shadowing would in theory produce the butterfly distribution in all energy channels; these populations could then be factored out.

With these considerations in mind, the decision was made to recalculate fluxes from L^*=6.2, it being the average GSO location in L^*. It was assumed that the phase space density did not vary significantly between L^*=6.2 and L^*=7. Then, invoking conservation of the first invariant:

$$p_{GSO} = \sqrt{\frac{E^2}{c^2} + 2m} \tag{22}$$

$$PSD_{GSO} = \frac{f_{GSO}}{p_{GSO}^2} \tag{23}$$

$$\mu = \frac{p_{GSO}^2 sin^2\alpha}{2m_0 B} \tag{24}$$

$$PSD_B = PSD_{GSO} \tag{25}$$

$$p_B = \sqrt{\frac{2\mu m_0 B}{sin^2\alpha}} \tag{26}$$

$$f_B = PSD_B P_B^2 \tag{27}$$

$$E_B = \sqrt{p_B^2 + m^2c^4} - mc^2 \tag{28}$$

Having obtained both the expected flux at the boundary and the energy to which these electrons would be adiabatically translated, it is possible to use an empirical power-law fit to calculate the boundary flux parameter. The subscript B in the above calculations was used for 'boundary', while the subscript GSO denoted parameters for geostationary orbit.

Ganushkina et al. [2013] used the Inner Magnetosphere Particle Transport and Acceleration model (IMPTAM) to simulate low-energy flux from the plasma sheet. The results were compared with fluxes measured at different energy channels from geostationary satellites. It was found that large-scale convection using steady electric and magnetic fields were insufficient to reproduce particle flux profiles. Adding local current pulses to represent substorms, whose times were inferred from the AE index, improved results significantly. A later study simulating quiet times [Ganushkina et al., 2014] when there was no large-scale variation in electric or magnetic field models, again confirmed that substorm modelling made it possible to reproduce peaks in flux that occurred at the inferred times of the substorms. These results indicate that substorms have a significant effect on the electron seed population at GSO and must be included in representative convection models. In the model used in this study, no attempt was made to explicitly account for substorms, though new versions of VERB are currently under development which will have that capacity. The effect of substorms is to a degree captured by NARMAX, but with its 24-hour resolution, dynamics on the scale of hours or less would be smoothed.

2.8 Magnetopause shadowing simulation using VERB

The effect of magnetopause shadowing on the radiation belts is a fast, non-adiabatic loss of energetic particles to interplanetary space. When the drift paths of trapped radiation belt particles cross the magnetopause location, they couple to interplanetary magnetic field lines and are lost from the radiation belts [Desorgher et al., 2000]. It affects particles across the pitch angle and energy spectrum, including energies that are too low for EMIC resonance [e.g. Bortnik et al., 2006]. Depending on the intensity of the event, L-shells up to and inwards of geosynchronous orbit may be affected. According to Yu et al. [2013] magnetopause shadowing, with the associated outwards radial diffusion driven by a sharp gradient, can account for over 90 percent of high-energy electron loss

outwards of L^*=5. Modelling and predicting such losses is an ongoing effort in the radiation belt community. Using VERB, one way to model such an event is to physically switch off the simulation at the time of the dropout and re-start it immediately afterwards. This in effect resets the PSD to zero. In reality the dropout losses may affect only the higher L-shells, leaving some part of the belt intact. Thus the above method, which resets PSD to zero across all parameter space, is a somewhat crude approximation of the real process. However, it is still a useful tool for emptying PSD inside the local acceleration space, which is quite hard to do otherwise.

The classic way of simulating main-phase depletion in the earlier versions of VERB is described in Subbotin et al. [2010], in essence by cutting flux to the outer boundary. However, as the parameter 'boundary flux' is a measure of flux at all energies assuming a roughly exponential distribution, even very low values can still equate to enough low-energy electrons to generate a seed population for local processes. As a result, it has been proven in tests and can be seen on Fig. 15 d,e in the paper, high levels of flux are maintained inside the local acceleration region. In fact, experiments proved that even setting the boundary flux to as low as 1×10^{-15} still produced a steady increase in flux around $L^* = 4$ to observable levels when local acceleration was turned on. Setting the boundary flux values lower risked destabilising the simulation by generating areas of zero PSD.

3 Chapter 3: Results and Analysis

The model output was validated against both GOES-13 measurements at geosynchronous orbit and Van Allen probes measurements through the radial range $L^* = 3 - 6$. No attempt was made to analyse the inner Van Allen belt because the version of VERB used in this particular study does not model it. The inner belt is believed to be geomagnetically stable, with slow predictable flux variations linked to the solar cycle. The Van Allen probe B was used, and fluxes were compared to observations made by the MagEIS particle detector [Blake et al., 2013]. For validation with the GOES-13 integral fluxes, two differential flux time series were obtained for geostationary orbit from the model and then coverted into an integral flux time series. Details of this operation can be found in Appendix 1.

Three time periods were analysed: August 1-25, September 1-23 and October 1-20, 2013. Each time period will be analysed in detail below, with discrepancies and sources of uncertainty also analysed and accounted for.

3.1 Period 1-25 August 2013

The results for August 1-25, 2013, can be seen on Figure 7: (a) shows the Dst and Kp indices, (b) shows the outer boundary as calculated from NARMAX predictions (blue), real GOES-13 data (red) and taken from the VNC output (green). Figure 7 (c) shows Van Allen probe B MagEIS data for the channel corresponding to an energy of 892 keV, and (d) shows the VNC simulation for the same energy. All flux values as logarithmic, in differential units of $cm^{-2}sec^{-1}sr^{-1}keV^{-1}$.

This time period contains three periods of geomagnetic disturbance - 4-6 August, 13-18 August and 21-23 August. As can be seen on Figure 7 (a) each period sees the Dst index drop below zero sharply, which is then followed by a slow recovery where Dst index returns to zero unless interrupted by another magnetic storm. The Kp index rises sharply, then falls again.

Figure 7 (b) shows the daily integrated > 800 keV particle flux seen from geostationary orbit by the GOES-13 satellite (red) as well as NARMAX (blue) and VNC (green) modelling of the same integrated flux. It can be seen that a main-phase storm dropout is registered at the same time as the Dst drop, in accordance with numerous observations. Fluxes recover over 3-4 days, exceeding pre-storm levels unless interrupted by another disturbance. This can be seen very clearly for August 3-7 on Figure 7 (b). It is important to note that NARMAX (blue) registers the main-phase dropout with a 1-day delay and slightly over-estimates the recovery flux the next day. This has implications on the VNC simulation as NARMAX is an input to it, as will be discussed later.

Figure 7 (c) shows the differential electron flux observed on Van Allen B from the MagEIS channel corresponding to an energy of 892 keV, as a function of time and L^*. Time resolution is chosen to be 8 hours, which strikes a balance between reasonable temporal detail and capturing data at all L-shells the spacecraft traverses. The orbital period of the Van Allen probes is ≈ 9 hours. Elevated

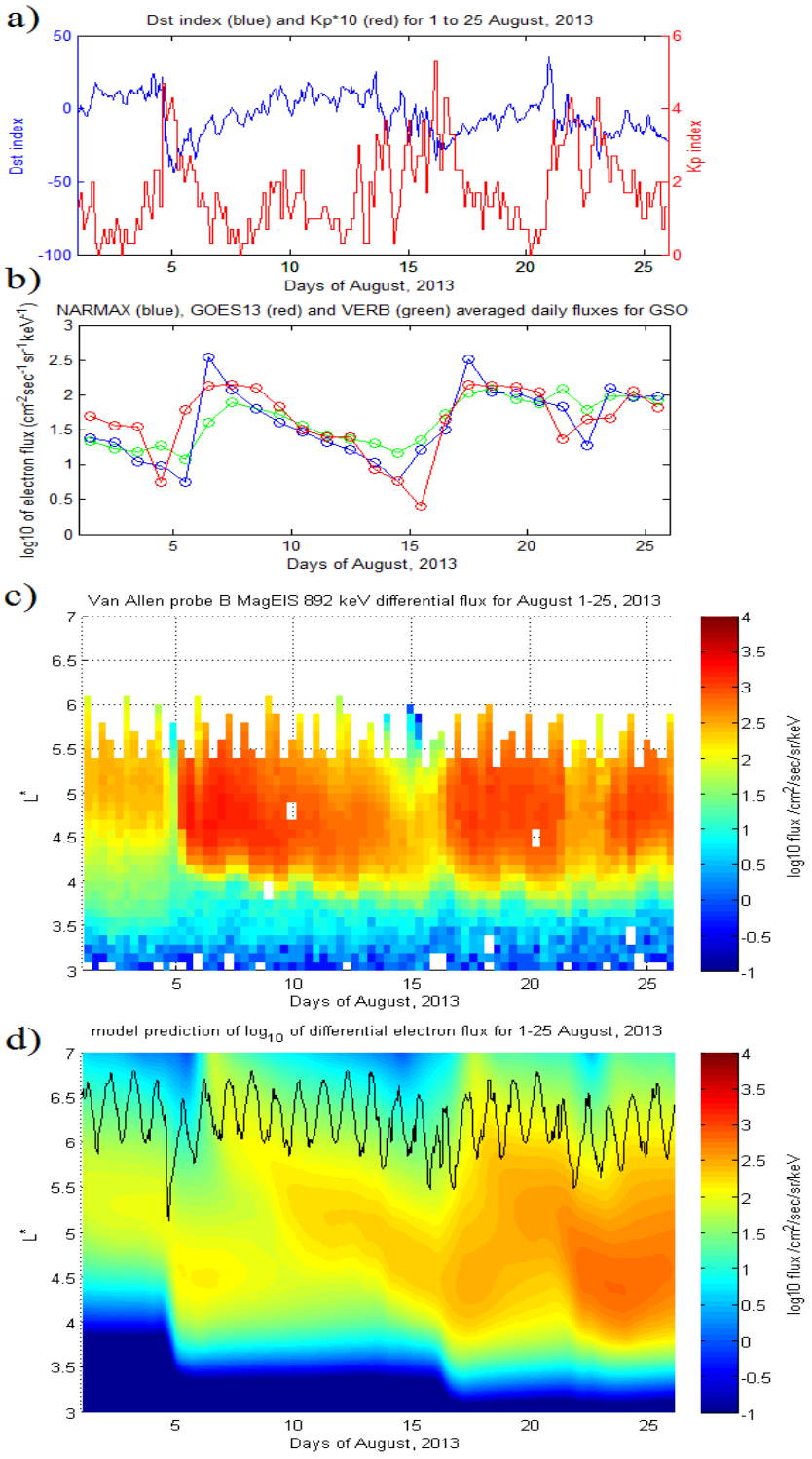

Figure 7: For 1-25 August 2013, a) Dst and Kp indices b) differential flux for NARMAX, GOES-13 and VERB c) Van Allen probe B MagEIS data for 892 keV, d) VERB simulation of the outer radiation belt using the NARMAX-derived differential flux as the outer boundary. Black curve in d) represents geostationary orbit.

flux levels can be seen between L^*=4-5.5, which corresponds to the location of the outer belt. Sudden drops in flux intensity can be seen around days 4-6, 13-17 and 22-24, which corresponds to the times of the aforementioned disturbances. Flux depletions are seen to penetrate through the entire belt, with flux levels rising afterwards, often beyond pre-storm values. This shows that the dynamics observed at geostationary orbit occur inside the whole outer belt.

Figure 7 (d) shows the VNC simulation of this time period. The units and scales are the same as for Figure 7 (c) for direct comparison. Several features are straightaway evident. First, the model does indeed reproduce the rapid depletions seen by Van Allen B and GOES-13 satellites. Three periods of flux depletion are seen at roughly the same times as in the observations. However, in the model the losses do not penetrate through the whole belt, as seen on MagEIS data. This results in the modelled fluxes building up over time in the heart of the radiation belt, which is not observed on the Van Allen probe. This demonstrates that magnetopause shadowing cannot be modelled simply by varying the outer boundary as non-adiabatic losses may extend lower than the simulation boundary [Kim et al., 2012].

In Figure 7 (d) on days 4-5 the peak of fluxes shifts from L^*=5.5 to L^*=4.5. The cause is most likely adiabatic acceleration in response to the compression of the magnetosphere. This effect is not present in the observations, possibly because in practice particles at those radial distances are scattered by plasmaspheric hiss. A related discrepancy between the model and observations is at the lower radial distance, below L^*=4 where VNC registers a flux build-up with electron counts increasing at lower values, while MagEIS observes a sharp cut-off in flux density around L^*=4.2. The area below that is the slot region which is formed by plasmaspheric hiss scattering electrons into the loss cone. As such it is probably the VERB wave model (in particular, the plasmaspheric hiss component of it) that under-estimates the pitch-angle scattering. VERB wave model diffusion coefficients are constantly being improved using statistical wave data and so it is likely that future versions of VNC will not have this issue.

Immediately following the main phase dropout is a flux enhancement that is evident on Figure 7 (c) on day 5. This enhancement is only partially reproduced by the model. The reason is as follows. The outer bounday for VERB is set from recalculated NARMAX fluxes. But NARMAX does not register the enhancement until the next data point (see Figure 7 (b) days 4-5), which in this case corresponds to a 1-day delay. By the time NARMAX registers the enhancement, the Kp index had already dropped from its peak value. Since all radial diffusion and acceleration processes in VERB are characterised by the Kp index, this leads to an under-estimation of energising processes and ultimately results in lower simulated particle counts. This is a problem that arises in simulating rapid storms (as opposed to generally periods of elevated geomagnetic activity) as a result of the low time resolution (24 hours per data point) of NARMAX, and its susceptibility to lag when predicting dropouts. As summarised earlier, dropouts are hard to predict in general because the only data available to predict such an event is solar wind data from L1, which only gives a 40-60 min warning of an impending compression event before impact. It

can however be noted here that increasing the time resolution of NARMAX to 1 hour rather than 24 hours should significantly improve simulation performance. Work to this end is currently ongoing.

Figure 7 (b) shows the VNC-simulated fluxes at GSO (green) taken from the output displayed on Figure 7 (d). The black line representing GSO location in L^* can be seen on Figure 7 (d); fluxes over 24 hours are read off from that line. It can be seen that the green line on Figure 7 (b) generally follows the NARMAX predictions (blue) while both dropouts and enhancements are less pronounced than for NARMAX. This is due to the fact that variations are smoothed as they propagate from the outer boundary to $L^* \approx 6.2$ which is the average GSO location. Figure 8 shows the hourly GOES-13 (blue) fluxes compared to VNC output (red) , and can be seen as similar to Figure 7 (b) (red and green respectively) but with a higher time resolution and in integral fluxes $>$ 800 keV instead of differential fluxes. NARMAX predictions are overlaid on the same figure as black crosses. Integral flux on the VNC was obtained by running the analysis for 2 different energies and assuming an exponential distribution to calculate integral fluxes from the two known values at each point in time. It can be seen that while VNC misses the main rapid build-up around days 5-7, it performs well at simulating the overall dynamics of GSO fluxes for this time period. The rapid flux build-ups on days 5-6, 16-17 and 23-24, are probably due to the Dst effect where geomagnetic activity changes the magnetic flux density around the spacecraft, so new particle populations from different field lines occupy that space preserving their first invariant [Kim and Chan, 1997]. These new populations may have higher counts, registering as an apparent storm-time enhancement. This is reproduced to an extent by the Tsyganenko [1989] magnetic field model which is Kp-dependent; in Figure 7 (d) it can be seen that the L^* line drops sharply towards L^*=5 on days 4-5.

An hourly time resolution shows a diurnal variation in fluxes that is averaged over in Figure 7 (b) daily flux values; as the spacecraft drifts to the nightside in the non-dipolar field, its position in L^* rises, or equivalently, its magnetic field strength decreases and the amount of magnetic flux enclosed per unit time falls. This places the satellite further from the heart of the radiation belts, and particle fluxes are lowered. While the spacecraft is around noon (1700 UT for GOES-13), particle fluxes reach their local maxima.

Overall, despite some of the aforementioned discrepancies, the model succesfully simulates each of the 3 major magnetic disturbances and reproduces observations both for GSO and for the whole outer radiation belt environment.

3.2 Period 1-23 September 2013

This time period features mostly quiet geomagnetic activity, with the Kp index mostly around 1-2. Figure 9 shows the time period in the same format as Figure 7. A Dst signature of some magnetic activity is evident in the beginning, around days 1-3. A second small drop in Dst can be seen around 18-20 September. Looking at the Figure 9 (b) it can be seen that there are broadly three periods of enhanced fluxes: on days 1-11, 14-16 and 18-23. The figure 9 (c) clearly

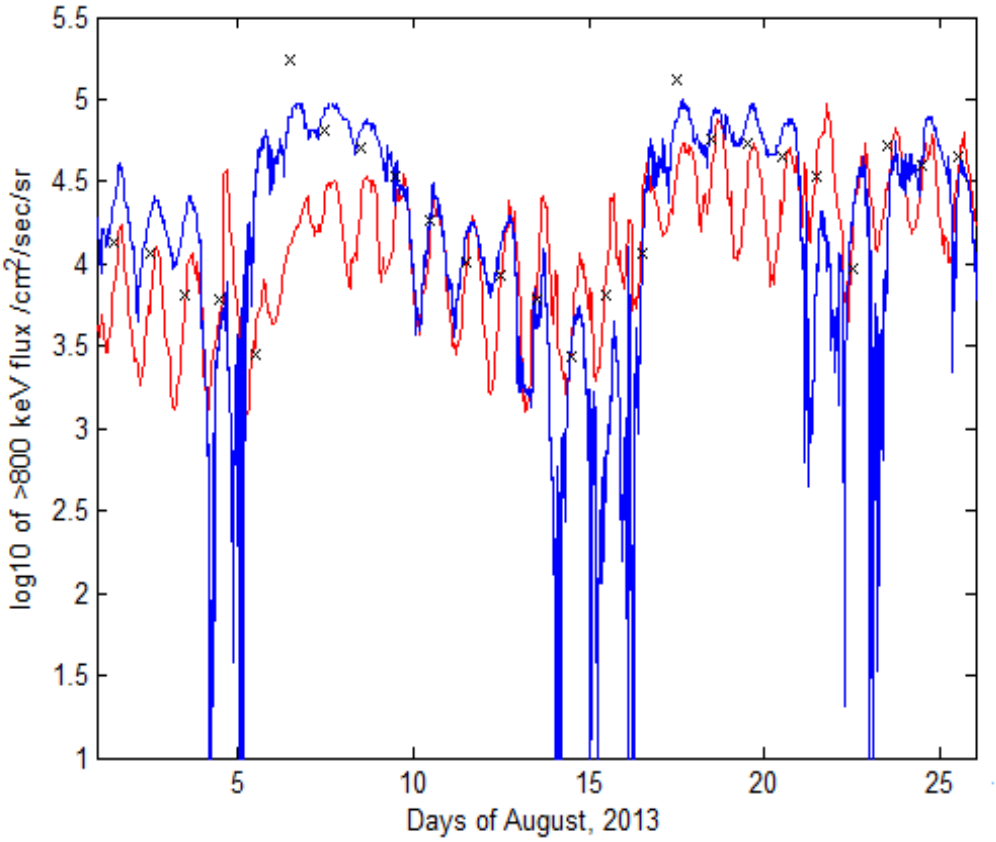

Figure 8: Integral fluxes for $>$ 800 keV electrons for August 1-25, 2013, for GOES-13 (blue) and VNC (red). Black crosses show NARMAX-predicted values for the days in question.

shows up the first and last enhancements, with the smaller enhancement around days 14-16 barely visible at the outer edge of the spacecraft's orbit. The Van Allen probes do not reach GSO at apogee, and dynamics seen at GSO may not penetrate inwards of L^*=5.5. However, all three enhancements are seen on the model in Figure 9 (d) which simulates for the interval between GSO and Van Allen probe coverage. There, a small enhancement on days 14-16 can be clearly seen at the outer boundary.

The model under-estimates flux increases in the days 1-5 September. It can be seen that NARMAX predicted low fluxes relative to those observed by GOES-13 on day 1; this delay meant that for the model, the injection did not start until the next day. The low fluxes are also possibly due to the fact that the simulation has not been running for long enough before activity occurs. It can be seen from Figure 9 (c) that on the first day, flux intensity around L^*=4-5 was already quite high, and the injection on day 2-3 added more particles to the radiation belt. In the model, the phase space density in the beginning by definition is zero outside the boundaries. Subbotin et al. [2011b] demonstrated that, in long-term simulations of VERB, results were in agreement with observations after 10 days of simulation spin-up. These simulations have been given one day of 'prior' spin-up time; this may not be enough. This point will be further explored later in the manuscript.

The third enhancement is also slightly underestimated for the same reason as explored in the previous time period. The flux increase clocked at GSO by GOES-13 (Figure 9 (b), blue) on day 19 coincides with a high Kp index. At that point, NARMAX flux predictions are low, and do not rise until day 20 by which point the Kp index has dropped from 4 (a maximum for this time period) to 0-2. A third discrepancy is that the model (Figure 9 (d)) predicts a slow, steady build-up of electrons in the heart of the radiation belts with the zone of maximum flux slowly moving downwards in L^*. This does not happen; according to Van Allen B data, flux fall across the whole outer belt in the days 12-19. Outwards radial diffusion as a result of magnetopause loss can be one explanation, but a more likely explanation, given the relatively benign geomagnetic conditions, is pitch-angle scattering by either chorus or EMIC waves. It will be shown later that adjusting dayside chorus model parameters causes the model output to more closely match observations.

Figure 10 shows the time interval fluxes for geostationary orbit. Besides from some discrepancy in simulating dropouts and a delay in following increased fluxes following injections, the model agrees with the data. The delay in registering flux increases is likely due to NARMAX; it can be seen by the black crosses on days 1-3 and 19-21 that NARMAX values were low when GOES-13 fluxes first started increasing. Model fluxes eventually rose as NARMAX generated a higher flux value at the next data point.

3.3 Period 1-20 October 2013

The third time period under consideration contains the most active space weather investigated here. As can be seen on Figure 11 (a) it contains three magnetic

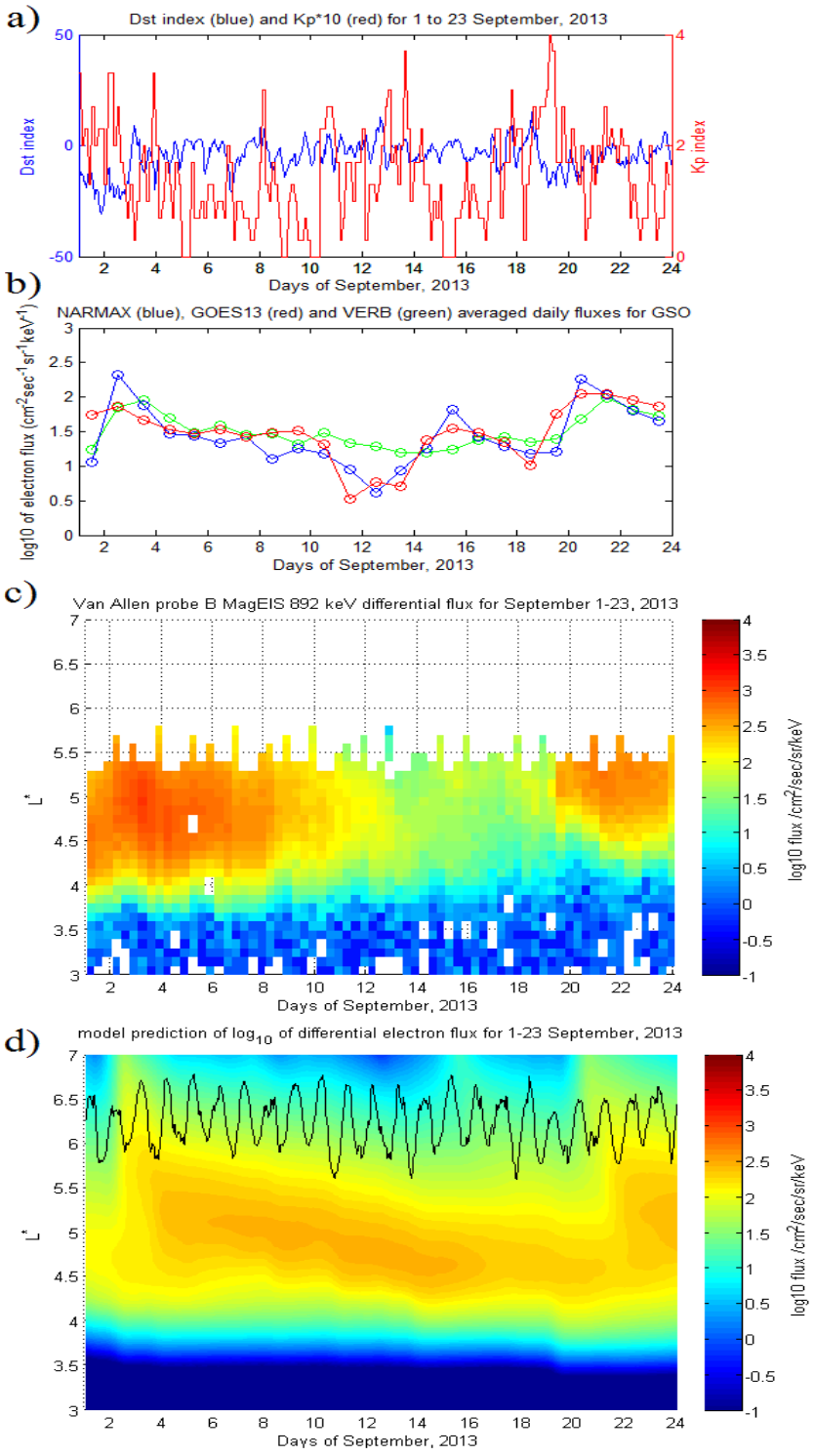

Figure 9: For 1-23 September 2013, a) Dst and Kp indices b) differential flux for NARMAX, GOES-13 and VERB c) Van Allen probe B MagEIS data for 892 keV, d) VERB simulation of the outer radiation belt using the NARMAX-derived differential flux as the outer boundary. Black curve in d) represents geostationary orbit.

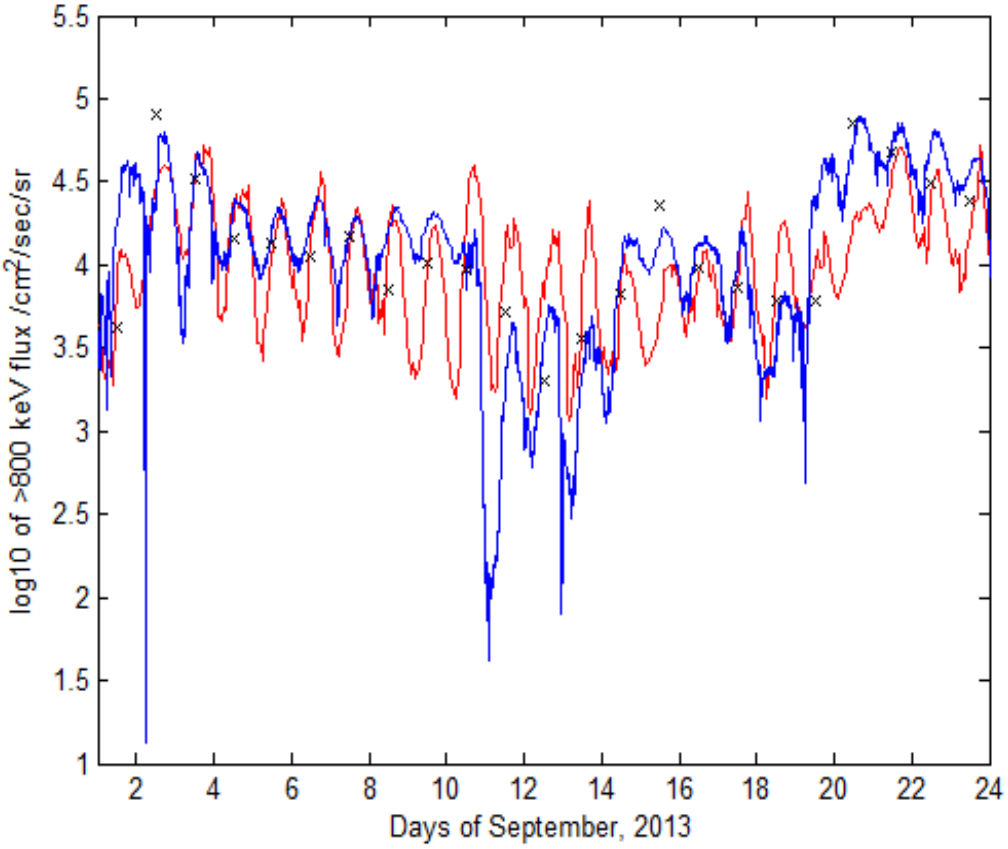

Figure 10: Integral fluxes for > 800 keV electrons for August 1-25, 2013, for GOES-13 (blue) and VNC (red). Black crosses show NARMAX-predicted values for the days in question.

storms, on days 2-3, 8-9 and 14-16. The Kp indices reach maxima of 7, 5 and 4+ respectively. Aside from storm time periods (which are intense and quite short), the Kp index hovers around zero. This presents a challenge to the VNC model - a delay in forecasting storm onset will result in the bulk of storm-time local acceleration and radial diffusion being carried out under very different Kp indices than during the storm itself.

Nevertheless, as seen on Figure 11 (c) and (d), the observations and the model are in agreement for this active space weather case. All three storms are reproduced. It can be seen on Figure 11 (b) that in this case NARMAX tracks the GOES-13 fluxes quite well. A small flux enhancement at day 1 can be seen around L^*=5 which is picked up by the model. There follows a dropout, which is captured by the simulation, and then an injection on days 2-3 which is also captured. The intensity of the storm is such that fluxes rise even inwards of L^*=4 where normally energetic electrons would be scattered by plasmaspheric hiss. This continues until days 8-9 when there is another storm and another main-phase dropout. This is also captured by the model. A region of enhanced flux intensity forms around L^*=4 in both model and observations; this persists until days 14-15 when there is another storm and another dropout. The fluxes fall correspondingly in the model and in observations. The belt rebuilds for a third time around L^*=4-4.5 which can be seen on both observations and model. This time the belt persists until the end of the time period.

Looking at the black line on Figure 11 (d) representing GSO location, it can be seen that GSO moves inwards dramatically during storm time, as the magnetospheric compression increases magnetic flux density. This calls into question the validity of the assumption that GSO is represented by L^*=6.2 during intense storm events. One can speculate that fluxes recalculated from L^*=5 would correspond to even weaker outer boundary fluxes, which may result in more pronounced dropouts. However, this is largely meaningless without hourly NARMAX forecasts as daily integral NARMAX forecasts absorb the rapid hourly variations and detail is lost. A future version of VNC could have the assumed L^* for GSO vary with MLT and Kp index to achieve higher accuracy.

It is interesting to note that the daily integrated fluxes output from VNC at GSO (Figure 11(b), green) do not vary much. Although both L^* at GSO and fluxes vary widely with storm activity, in effect the two variations compensate for each other. As can be seen on Figure 11 (d) on, for example, days 2-3, during storm time both the area of peak flux and the GSO move downwards in L^*. A more high-resolution picture of VNC output at GSO can be seen on Figure 12. Although the model output (red) deviates from the steady-time diurnal sinusoid variation and takes on quite dramatic shapes, flux variation from one day to the next is quite low. This contrasts with the GOES-13 observations (blue) and NARMAX (black crosses), especially on days 2-3 during the most intense storm in this time period. It should be noted that the magnetic field model used in this study is only driven by the Kp index. As such it does not explicitly account for magnetospheric compression (solar wind velocity, pressure, density) or B_z which is linked to magnetic reconnection and dipolarisation of the magnetosphere. It is very possible that using another magnetic field model

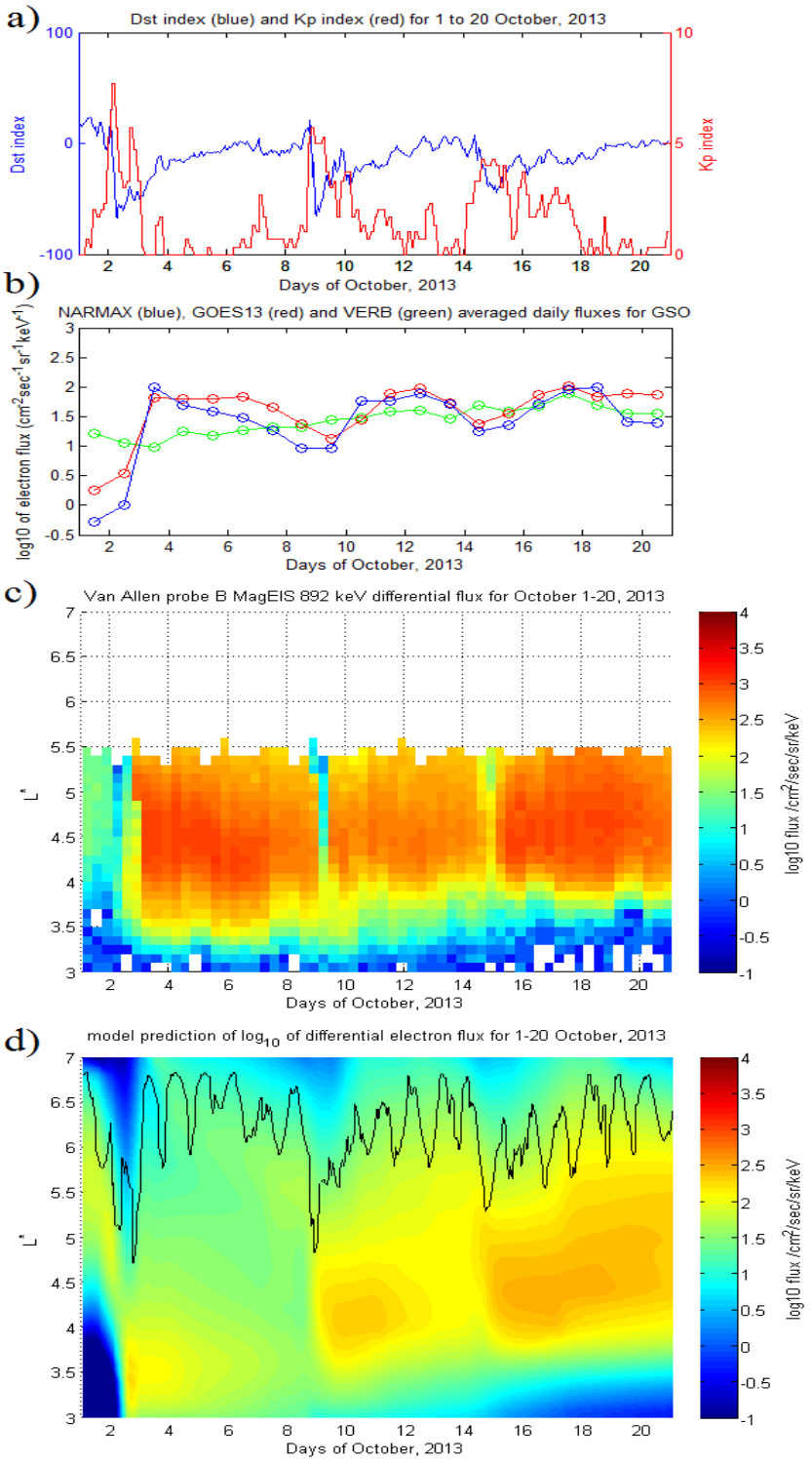

Figure 11: For 1-20 October 2013, a) Dst and Kp indices b) differential flux for NARMAX, GOES-13 and VERB c) Van Allen probe B MagEIS data for 892 keV, d) VERB simulation of the outer radiation belt using the NARMAX-derived differential flux as the outer boundary. Black curve in d) represents geostationary orbit.

that does take account of this data will result in a more accurate picture of L^* at GSO at high geomagnetic indices.

3.4 Simulation results at low energies

For the aforementioned three time periods, low-energy flux simulations are presented below, as well as the corresponding observations from the Van Allen B probe. The MagEIS channel corresponding to 54.4 keV is used for this section, and VNC output is computed for this energy.

Figure 13 (a) shows the MagEIS low-energy flux for August 1-25, 2013, and Figure 13 (b) shows the VNC simulation at the same energy. The inner belt ($L^*< 3.5$) is omitted in the simulation. The VNC simulation domain has a greater outer range than the Van Allen probe orbit, making it possible to observe how outer boundary variations propagate across the outer belt at these low energies.

It can be seen that VNC over-estimates fluxes compared to MagEIS observations. This appears true for low energies as for higher energies. The possible causes are difficulty in effectively simulating magnetopause shadowing, or inaccuracies in the wave model. Another difference is that flux enhancements, where they occur, penetrate to lower L^* in the observations than in the simulation.

However, despite these differences and the apparently distinct radial profile, the simulated flux profile below L^*=5.5 (black line in Figure 13 (b)) is similar to observations. The profile shows a series of enhancements caused by particle injections from the outer boundary. There is no sign of any local acceleration around L^*=4, and in fact flux levels between the injections are distinctly low. This is not surprising considering that, according to classic radiation belt theory, low-energy electrons diffusing inwards from the outer boundary are accelerated to MeV energies by magnetospheric waves or lose energy in generating these waves. Five enhancements are visible - a small one around August 1-2, a larger one on August 4-8, another small enhancement on August 10-12, and two large enhancements on August 14-19 and 21-25 respectively. All five are successfully simulated by VNC. Furthermore, by looking at the flux profile above L^*=5.5 and to the outer boundary, VNC makes it possible to see where these enhancements come from. In fact all of them are outer boundary variations that propagate down to the heart of the outer belt where they are observed by the Van Allen satellite.

Figure 14 shows the low energy flux for September 1-23, 2013, for the same energy as before. This time period features sporadic and relatively low-level geomagnetic activity, possibly indicative of repeated substorms. Figure 14 (a) gives more evidence of this, showing repeated injections of low-energy particles on Sept 1-5, Sept 7, Sept 10-15, Sept 18 and Sept 19-22. The simulation also shows repeated injections inwards of L^*=5.5, although it overestimates their magnitude due to NARMAX over-estimating GSO flux on Sept 2-3, Sept 15-16 and Sept 20-21. Once again, injections do not penetrate inwards of L^*=4, likely due to an over-estimation of a mechanism for depleting low-energy electrons in that area. NARMAX also predicts enhancements with a delay during this time

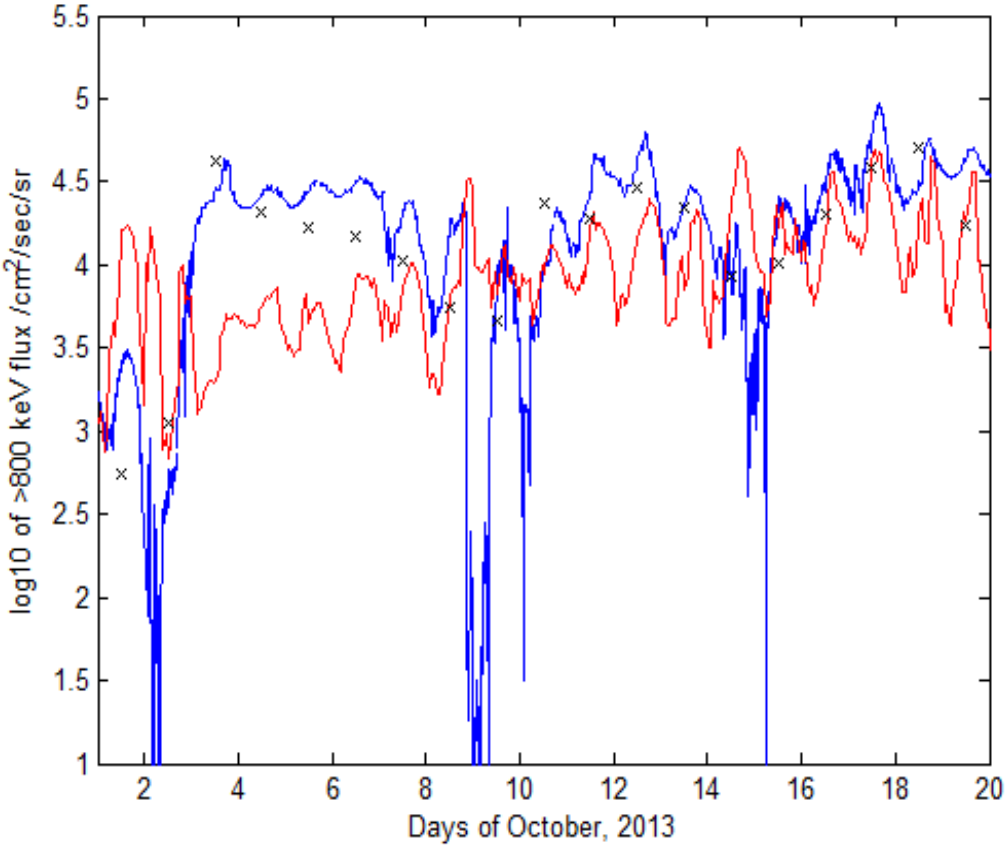

Figure 12: Integral fluxes for > 800 keV electrons for August 1-25, 2013, for GOES-13 (blue) and VNC (red). Black crosses show NARMAX-predicted values for the days in question.

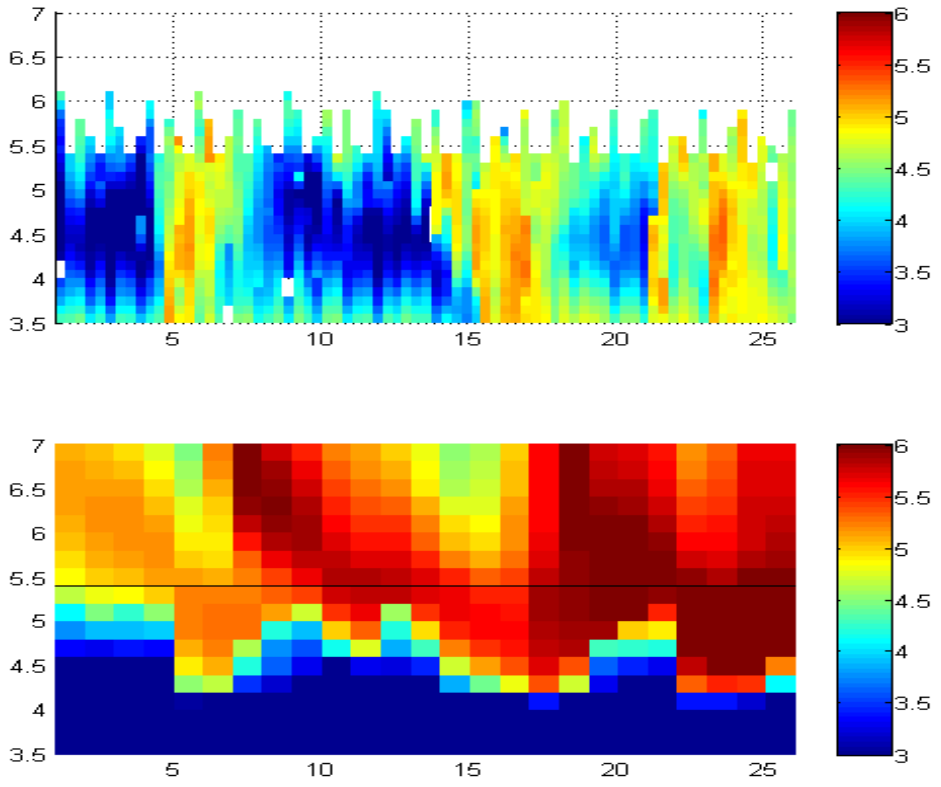

Figure 13: Low-energy (54.4 keV) fluxes (a) observed on MagEIS and (b) modelled by VNC, for the period 1-25 August 2013. The black line in (b) shows the location of the approximate maximum radial reach of the Van Allen B satellite orbit.

period, and this delay shows up in VNC (the fluxes approach their maxima around Sept 2-3, Sept 12-14 and Sept 19-23, while VNC predicts maxima below L^*=5.5 for Sept 4-6, 11-16 and 20-24 respectively).

The low-energy fluxes for October 1-21 are shown on Figure 15. The three enhancements starting on October 2, 9 and 14 are clearly visible on Figure 15 (a). They are reproduced below L^*=5.5 on the VNC simulation (Figure 15 (b)). The most striking difference here between the results and the simulation is the lack of any low-energy electrons below L^*=4 in the simulation. That is not observed by Van Allen B, and in fact, fluxes are more intense below L^*=4 and persist for longer. The reason for this difference at 54.4 keV is unclear. It is possible that the plasmaspheric hiss model may overestimate pitch angle scattering at these energies, since it usually acts around L^*=3-4. Beyond that, VNC once again reproduces enhancements seen on MagEIS, albeit with a smaller amplitude for reasons discussed previously. It also simulates the flux profile above the Van Allen satellite orbit, making it possible to see where these injections came from. It can be seen that the enhancements in MagEIS flux on October 9 and 14 were preceded by increases in flux at GSO on October 4 and 12, which can also be seen on Figure 11 (b) (red and blue lines). These outer boundary variations later diffused inwards and, following periods of elevated geomagnetic activity around October 9 and 15 respectively, were rapidly transported inside L^*=5.5. A similar event happened on October 2, leading to the flux near the outer boundary to end up inside the Van Allen B orbital range. The enhancement that created that original population is not visible, and must have occured before October 1. It is possible that if the simulation had covered an earlier time period, that disturbance would have been included and the magnitude of the first flux enhcancement would have been closer to what was really observed on MagEIS.

It might seem striking that the outer boundary populations would take so long (days) to diffuse inwards to the heart of the radiation belt. However, we must remember that Kp index is very low for most of the time period, except for the three rapid and short-lived spikes. Indeed, a drop of one Kp index value would correspond to a decrease in D_{LL} of about half an order of magnitude (Figure 5 in [Brautigam and Albert, 2000]).

The fact that NARMAX, which predicts GSO flux for two high-energy channels, appears capable to successfully simulate particle injections for such low-energy electrons, is one surprising outcome of this project. Traditional state-of-the-art radiation belt theory [e.g. Shprits et al., 2008a, and references therein] suggests that high-energy electrons at GSO come from a locally accelerated population at L^*=4 that then diffuses outwards. However, if that were the case, this model would not show any agreement with observations for low energy, since there would be no causal link between high-energy electrons at GSO and low-energy electrons inside GSO. If anything, it would be the other way around, and so the only way to model injections properly would be to train NARMAX on a low-energy channel of a geosynchronous satellite and then to generate predictions hourly so as to be able to isolate those MLT sectors where injections are likely to happen. The fact that the low time resolution (24 hours) NAR-

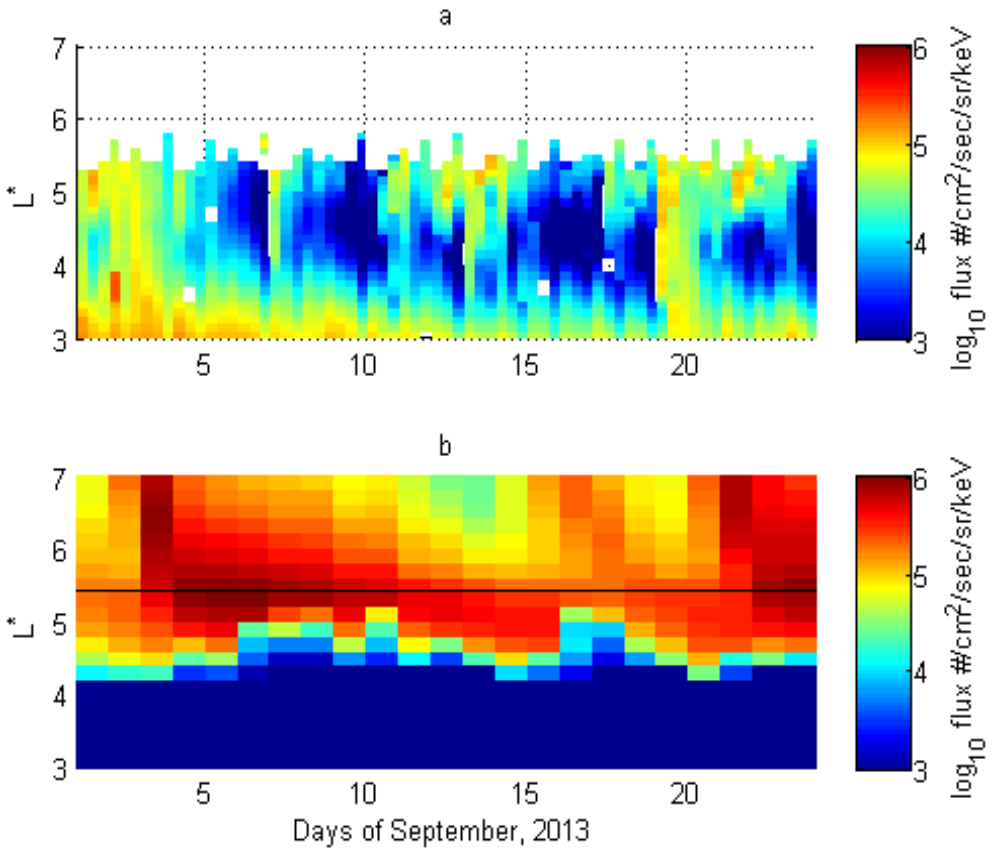

Figure 14: Low-energy (54.4 keV) fluxes (a) observed on MagEIS and (b) modelled by VNC, for the period 1-23 September 2013. The black line in (b) shows the location of the approximate maximum radial reach of the Van Allen B satellite orbit.

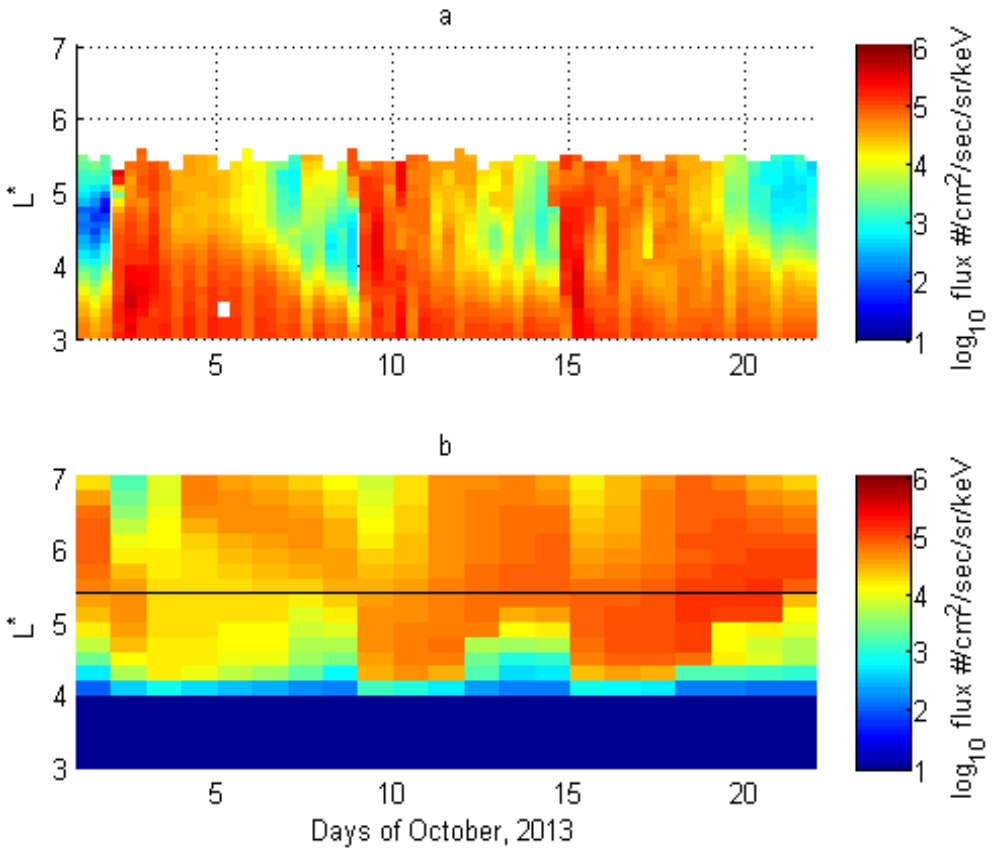

Figure 15: Low-energy (54.4 keV) fluxes (a) observed on MagEIS and (b) modelled by VNC, for the period 1-21 October 2013. The black line in (b) shows the location of the approximate maximum radial reach of the Van Allen B satellite orbit.

MAX with its high-energy output can successfully simulate low-energy radiation belt dynamics suggests that high energy electrons at GSO do not come from inside GSO but are in fact a high-energy tail of a population that originated from the plasma sheet. This could have happened because of intense transient acceleration processes in the magnetotail.

It is probable that both processes take place simultaneously and the relative importance of one over the other is unclear. One way to see which one predominates is to use GSO data for a low-energy channel as an input and to see if the results are better than if the $>$ 800 keV and $>$ 2 MeV GOES-13 energy channels are used.

3.5 Simulation results at high energies

Figure 16 shows the MagEIS observations and VNC simulations for a high-energy channel, in this case one corresponding to 2.519 MeV, for August 1-25, 2013. Compared to Figure 13 local acceleration around L^*=4 is pronounced (it was non-existent for low energies). Fluxes around L^*=4 increase steadily throughout the simulation period, reaching a maximum towards the end of it. No such behaviour is seen in observations, however. Although Figure 16 (a) does show a steady flux around L^*=4 between August 1-15, it does not increase monotonically as on the VNC simulation. This suggests a balance between energy diffusion by wave-particle interactions and losses, probably by pitch-angle scattering by EMIC waves. Outwards radial diffusion following magnetopause compression is also a possible loss source, but Figure 13 (a) shows that low-energy fluxes seem to increase at time periods when high-energy fluxes drop (around August 15 and August 20-25) as particles from the outer boundary enter the heart of the outer radiation belt. Magnetopause shadowing and outwards radial diffusion should affect particles at all energies simultaneously. Since EMIC waves were not modelled in this simulation, it is probable that they are the missing source of high-energy particle losses.

There is a high-energy population that is clearly visible in Figure 16 (a) between August 6-14 around L^*=5, drifting radially lower over the course of the next few days. This population is also visible on the VNC simulation (Figure 16 (b)). This is distinct from the monotonic locally accelerated population around L^*=4 and appears to have come from the outer boundary. The fact that VNC modelled it successfully, including its 'descent' which is consistent with inward radial diffusion, it is possible to state that this population came from the outer boundary and was not locally accelerated. If this is the case, this is a high-energy tail of a population that has been injected into the inner magnetosphere from the plasma sheet. The magnitude of this tail is comparable to the magnitude of the locally accelerated electrons in the heart of the belt. In fact the outer belt appears to have two regions of peak flux around August 5-9, with an area of reduced flux between them. The same dynamic is reproduced on the VNC observations.

This result makes it possible to tentatively say that the electron flux due to high-energy tail of injected populations can be just as strong as that from

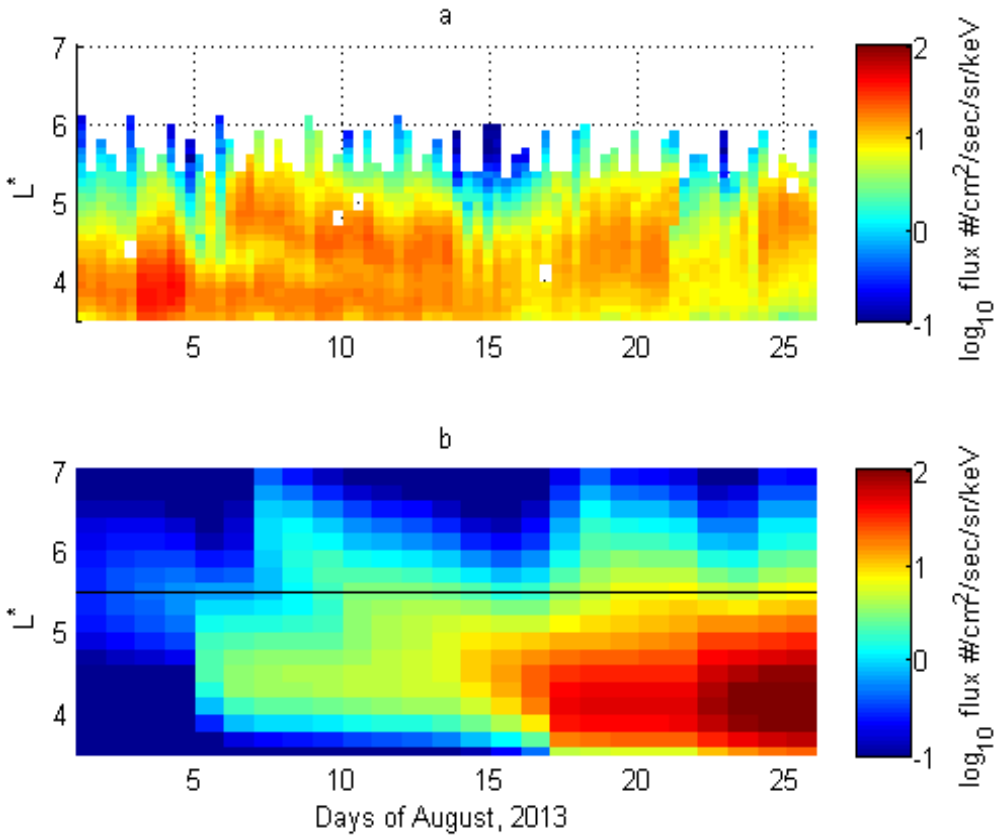

Figure 16: High-energy (2.519 MeV) fluxes (a) observed on MagEIS and (b) modelled by VNC, for the period 1-25 August 2013. The black line in (b) shows the location of the approximate maximum radial reach of the Van Allen B satellite orbit.

locally accelerated particles. In some places it even appears stronger. Two zones of increased 'killer' electron flux can result in the outer belt - one due to local acceleration and another area, slightly higher, due to the injected electrons.

The high-energy flux for september 1-23, 2013, is displayed on Figure 17. Here the local acceleration again begins to dominate model output (figure 17 (b)). The two periods of increased flux diffusion from the outer boundary (September 2-12 and 19-23) are represented by the model (increased flux from the outer boundary is visible on September 3-4 and 21-24 on Figure 17 (b)). However, how these injections manifest inside L^*=5 is unclear as local acceleration dominates the flux profile. Continuous local acceleration is present around L^*=4 in Figure 17 (a) but does not increase with time as in the simulation. This suggests a balance of sources and losses (probably the aforementioned EMIC waves which are not included in the model).

High-energy (2.519 MeV) fluxes modelled for October 1-21, 2013, are shown on Figure 18. Three periods of flux enhancement can be identified on observations and the model (October 2-9, October 9-14 and October 15-21), but their radial profile is wrong. Unlike in Figure 15 (b), where the model predicts a sudden drop of fluxes below L^*=4 while the observations do not match it, here the situation is reversed. The observations show that high-energy fluxes drop off rapidly below $L^* \approx 3.5$, while the model predicts local acceleration below L^*=4. It is possible that this is due to the large Kp indices during storm times - the magnetic pressure forces the whole outer belt inwards radially, and all local acceleration processes run at lower L-values. However, there is no evidence of steady local acceleration in the MagEIS data, certainly not on the scale predicted by the model. Meanwhile, significant high-energy populations can be seen around L^*=5 on October 2-9 and October 15-21 (to a lesser degree also on October 9-14), which are not modelled by VNC at all. EMIC waves are turned off for this VNC run which could potentially be responsible for scattering high-energy electrons around L^*=4. But EMIC waves do not accelerate electrons, and so no explanation exists for the model's failure to simulate the aforementioned populations outwards of L^*=4.

In conclusion it is fair to say that energetic ($>$ 1 MeV) electrons dynamics do indeed seem to be governed by different processes than those within the framework of the 'classic' radiation belt modelling. It is possible that other wave types exist at these times that are not included in the code. As the results demonstrate, model output for high energies, particularly with rapidly changing indices, should be treated with caution.

3.6 Observed GOES-13 data as the input to VNC

In order to test the robustness of the VNC scheme assuming a 100 % perfect NARMAX prediction, the same time periods as before were analysed with real GOES-13 integral daily flux data forming the input, instead of NARMAX predictions. All other parameters were kept the same. The purpose is to test the methodology - is it feasible to use daily integral fluxes of high energy channels to predict radiation belt fluxes at all energies, including energies lower than those

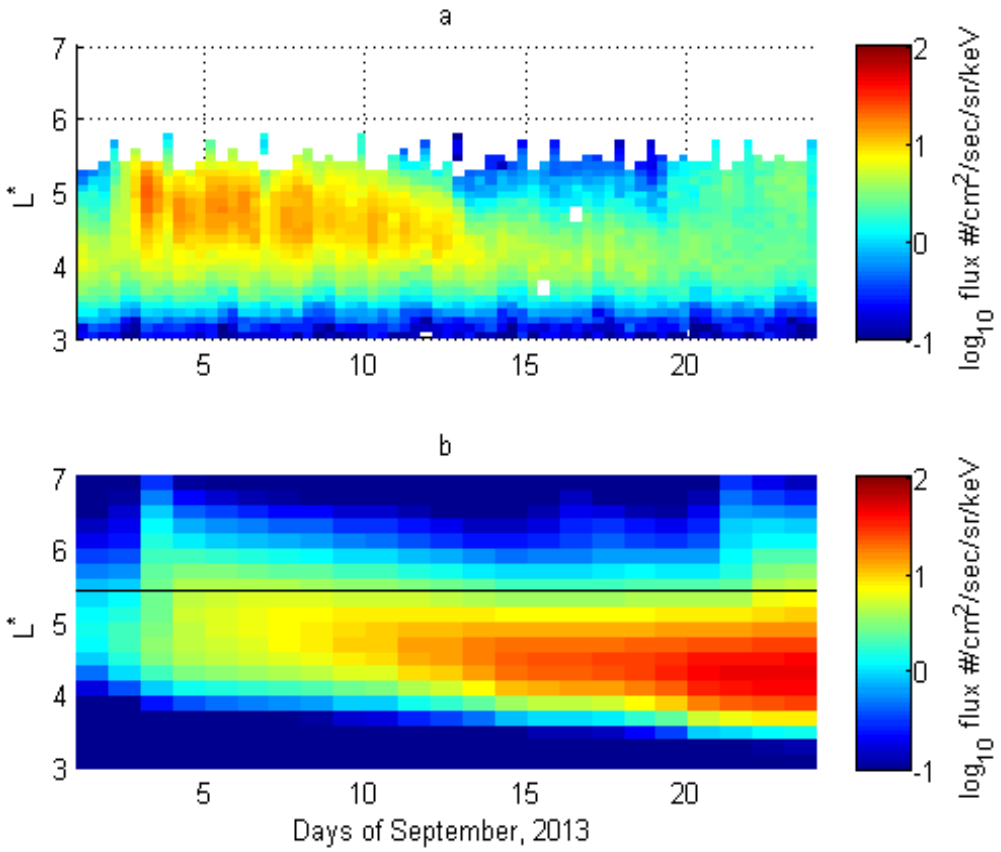

Figure 17: High-energy (2.519 MeV) fluxes (a) observed on MagEIS and (b) modelled by VNC, for the period 1-23 September 2013. The black line in (b) shows the location of the approximate maximum radial reach of the Van Allen B satellite orbit.

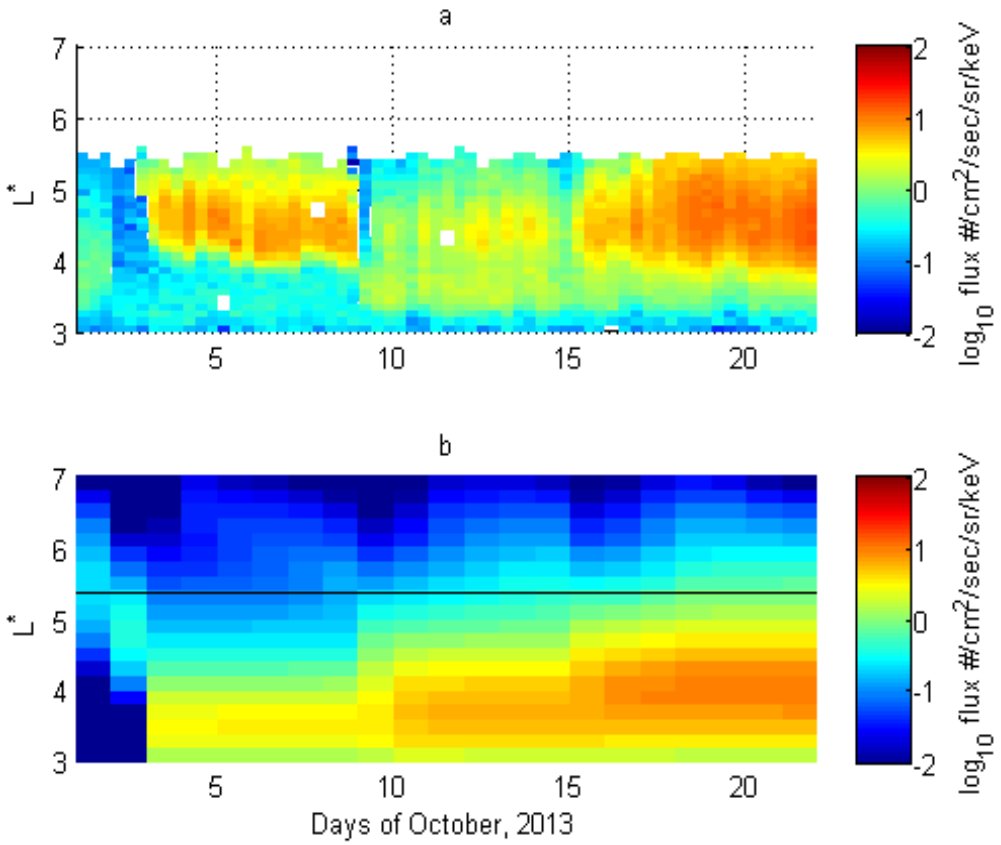

Figure 18: High-energy (2.519 MeV) fluxes (a) observed on MagEIS and (b) modelled by VNC, for the period 1-21 October 2013. The black line in (b) shows the location of the approximate maximum radial reach of the Van Allen B satellite orbit.

forming the input? The results for August 1-25, September 1-23 and October 1-20, 2013 can be seen on Figures 19, 20 and 21 respectively.

The first feature that can be seen observing the August event (both cross-L^* fluxes, middle, and GSO, bottom) is the low value of fluxes during enhancements compared to MagEIS data (top) and GOES-13 data (bottom, blue). Using daily GOES-13 flux as the input underestimates fluxes by up to an order of magnitude. Since VERB accounts for adiabatic effects by design, underestimations of storm enhancements do not come from neglect of adiabatic effects. Rather, it is believed that the outer boundary flux is underestimated.

The outer boundary flux is calculated using GOES-13 measurements of GSO fluxes at two energy channels - $>$ 800 keV and $>$ 2000 keV, integrated over 24 hours. Both of these channels detect relatively high-energy electrons, that could have come to GSO from two sources. Either they form part of a population that diffused inwards from the plasma sheet and radially accelerated to GSO, gaining energy in the process. Alternatively, they could be chorus-accelerated particles inside GSO around L^*=4 that had then subsequently radially diffused outwards, losing energy but still retaining enough to be captured by the detectors. Since the daily integral flux does not distinguish which MLT sectors contribute what proportion of fluxes, it is almost impossible to differentiate between the two potential sources at such low time resolutions.

It is tempting to point to this as a source of the discrepancy. However, in that case, the error should be in the other direction. If the problem is that the satellite sees electrons from not one but two sources, only one of which is 'correct', the result should be an over-estimation, not an under-estimation of fluxes. In fact, following that logic, since the highest electron counts are observed on the dayside where there are no particle injections, local acceleration processes should completely eclipse injections and a model built around these fluxes will consistently over-estimate fluxes with the output bearing little relation to observations. However, we consistently see a similarity between model and observations, albeit with injections under-estimated and fluxes over-estimated. Therefore, the problem has to lie elsewhere.

Injections of new populations into the inner magnetosphere can happen on the scale of several hours. However, GOES-13 daily fluxes and NARMAX predictions smooth out these events. Instead of the boundary flux exhibiting sharp spikes followed by long periods of low values, the system is input with generally elevated electron counts over time periods on the scale of days. This has two effects, both of which are observed on the VNC simulations when compared to observations both at and outside GSO. Firstly, flux enhancements are muted, with the system under-estimating electron counts following magnetic disturbances. Secondly, dropouts are not simulated properly. Outwards radial diffusion may occur in the simulation if the boundary flux is very low for long periods. This can be seen on Figure 20 for the September event, where following elevated GSO and boundary fluxes around September 2-10, a dropout is evident around September 11. This dropout can be seen as a sharp fall in flux around the outer boundary in the model (middle) and GSO (bottom). Observing the heart of the simulated radiation belt (middle) around September 14-18 the flux

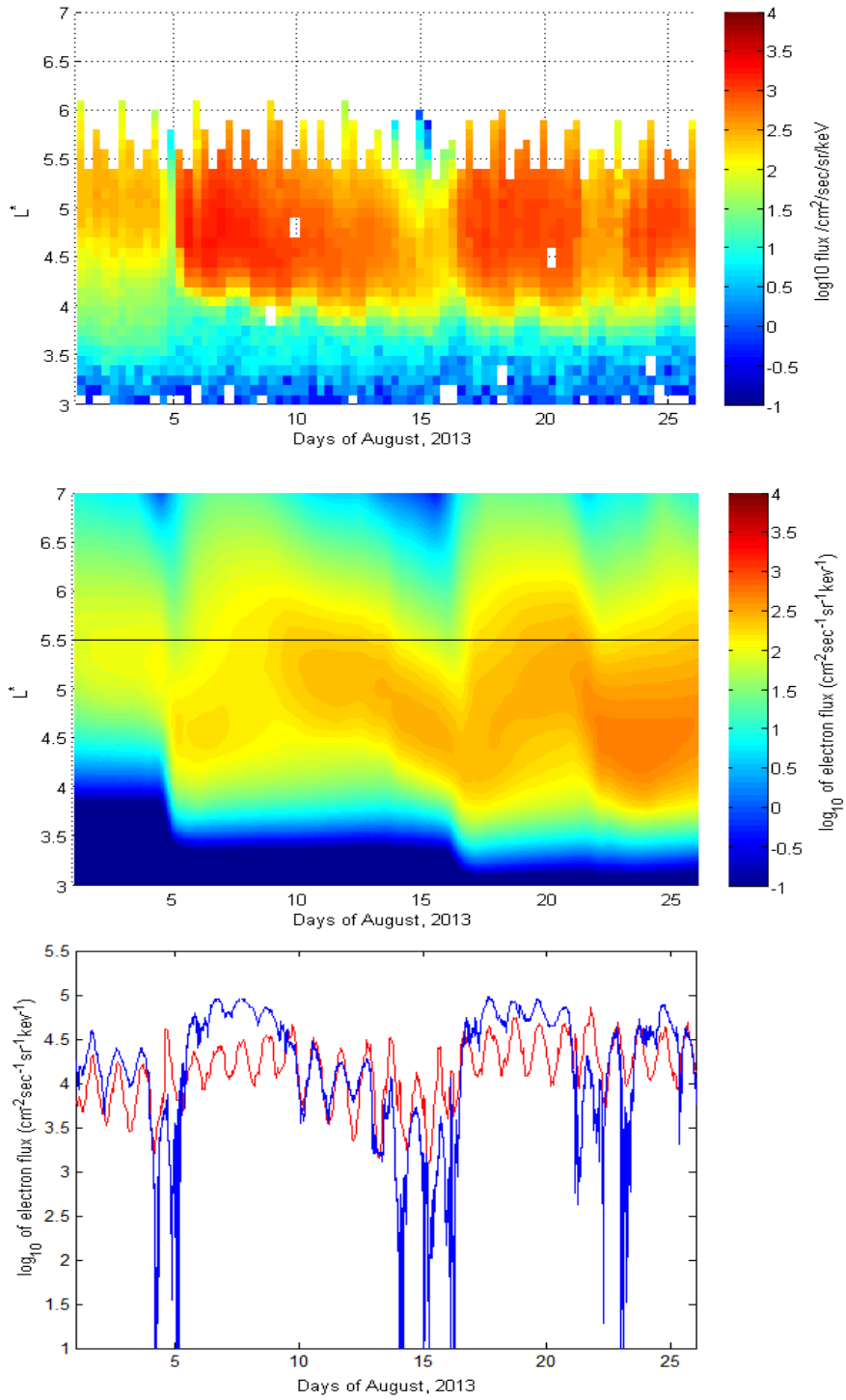

Figure 19: For 1-25 August, 2013, (top) MagEIS fluxes for 891 keV, (middle) VNC simulation of 891 keV fluxes using real GOES-13 data as input (black line denotes the location of approximate radial apogee of Van Allen B satellite orbit), and (bottom) integral GSO fluxes for 800+ keV observed on GOES-13 (blue) and modelled by VNC with GOES-13 input (red).

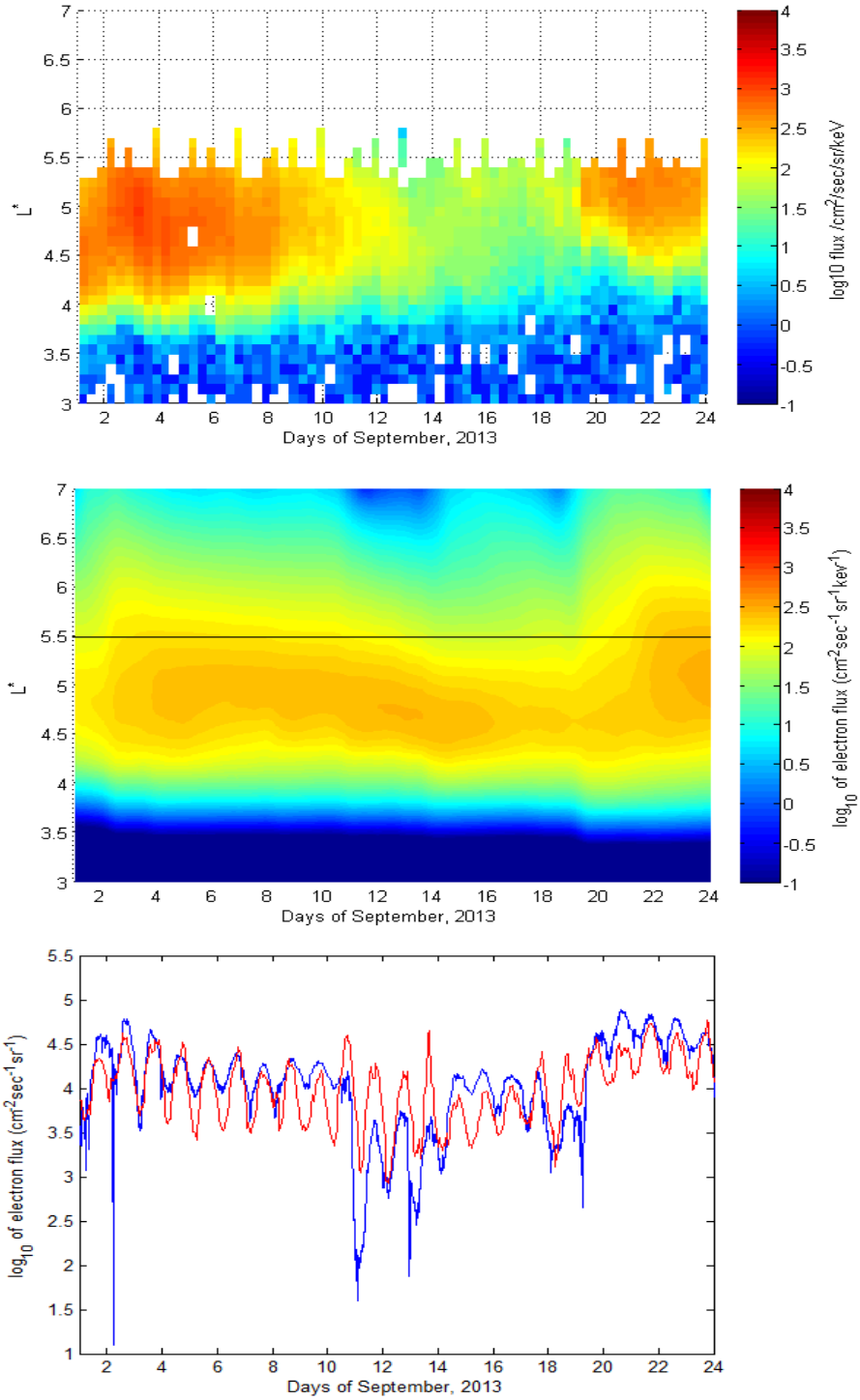

Figure 20: For 1-23 September, 2013, (top) MagEIS fluxes for 891 keV, (middle) VNC simulation of 891 keV fluxes using real GOES-13 data as input (black line denotes the location of approximate radial apogee of Van Allen B satellite orbit), and (bottom) integral GSO fluxes for 800+ keV observed on GOES-13 (blue) and modelled by VNC with GOES-13 input (red).

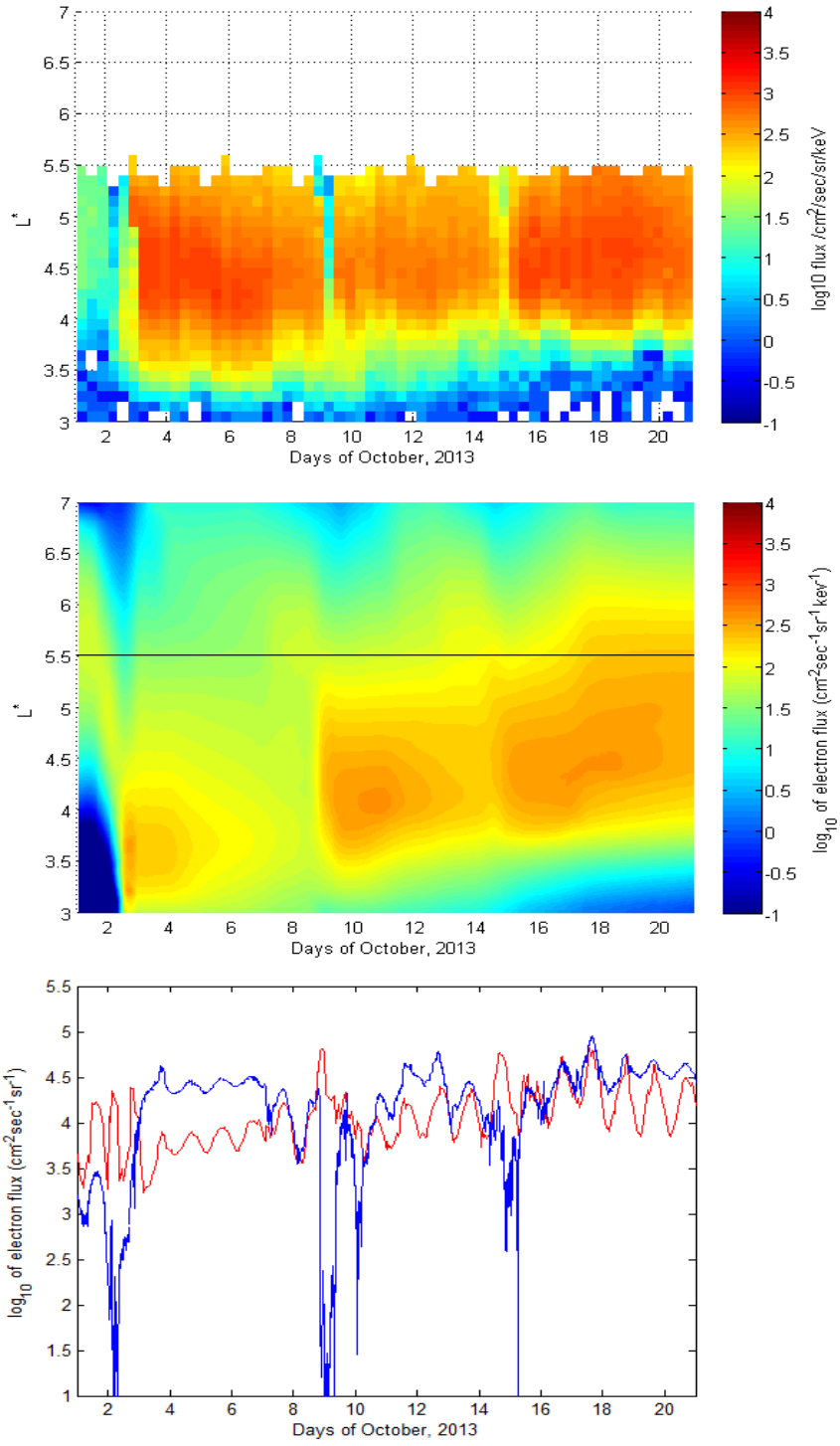

Figure 21: For 1-20 October, 2013, (top) MagEIS fluxes for 891 keV, (middle) VNC simulation of 891 keV fluxes using real GOES-13 data as input (black line denotes the location of approximate radial apogee of Van Allen B satellite orbit), and (bottom) integral GSO fluxes for 800+ keV observed on GOES-13 (blue) and modelled by VNC with GOES-13 input (red).

values definitively fall until the next series of enhancements.

However, if events that occur on the timescale of hours are instead averaged out so that they appear to occur on the scale of days, the simulation will inevitably over-estimate dropouts and under-estimate injections. Coming to the October 1-20, 2013 event (Figure 21) this process is particularly evident. In fact, looking at the GSO data (bottom), it can be seen that where the data shows dropouts the model shows enhancements! This occurs on October 8-9 and again on October 14-15. A look at the outer boundary (top of the middle figure, around $L^* = 7$), it can be seen that the bounday flux does indeed drop. In reality that translates into fast depletions across the entire outer belt (top). But the gradients of the outer boundary flux are nowhere near that high in the simulation. Observing GSO data, the flux on the October 8-9 depletion drops over 3 orders of magnitude. That sharp gradient is inevitably smoothed out over 24 hours (after all, high fluxes were also recorded on the same day, and they move the integral count upwards). As a result, the outer radial diffusion is not modelled correctly, does not penetrate into the heart of the radiation belt, and since the same disturbance that caused the depletion also caused the GSO to move adiabatically inwards in L^*, the model reads fluxes from near the heart of the radiation belt where they are highest. Thus the dropout is incorrectly modelled as an enhancement. A similar process repeats on October 14-15.

In fact, NARMAX partly compensates for this behaviour, because the prediction system tends to slightly over-estimate flux enhancements. This means that the model performance with NARMAX is better than model performance with real GOES-13 fluxes used as input. This can be clearly observed in the next section.

3.7 Long-term VNC modelling of magnetic activity

The VNC scheme suffers from transient behaviours that must be properly accounted for. Firstly, it is recommended to run VERB for several days of simulation before taking any measurements. This is because the PSD outside the boundaries does not correspond to a steady state on initialisation, and some 'slack' should be given for the code to approach a steady value. This is a common feature of diffusion-based codes and is present in VERB [Subbotin et al., 2011b] and, for example, SPACECAST [Horne et al., 2013]. Another question is how the model performs over a long time period having reached steady state. It was demonstrated earlier that at energies higher than 1 MeV, VNC consistently over-estimates fluxes and a persistent, steady build-up of electron fluxes is noted around L^*=4, making measurements at that energy range suspect. Does a similar effect take place below 1 MeV? It was already demonstrated that VNC underestimates flux dropouts. Over a long time period, this will lead to an artifical saturation of the simulation space with electrons, rendering the results after a certain time period meaningless and results before that time period suspect. To test this hypothesis, a 3-month time period was chosen for simulation, starting on 1 November, 2013.

The results for 891 keV can be seen on Figure 22. The figure shows MagEIS

fluxes (top), a VNC simulation of the same time period (middle), and a VNC simulation for the same time period using GOES-13 instead of NARMAX as the source of the outer boundary (bottom). The black lines denote the approximate apogee of the Van Allen satellite. Looking at the observations, three major storm time periods can be seen (plus several minor ones) - around days 10-20, 38-45 and 65-75. Observing the simulations (middle and bottom), the following conclusions can be drawn from this study:

1. The model successfully simulates all three major storms and, to various degrees, the minor storms. VNC driven by NARMAX actually performs better (as mentioned in the previous section) since NARMAX tends to overestimate flux enhancements. The GOES-13 driven VNC does underestimates all three major storms, while the main VNC overestimates the first one, underestimates the second one and predicts the third one reasonably well.

2. The model does not effectively simulate flux depletions. Nevertheless, throughout the 3-month period the heart of the radiation belts in the model clearly suffers depletions in the simulations. Over-estimation of dropouts is likely not due to a build-up of electrons over time, but due to the traditional problem of simulating dropouts that has been explored in the previous section. No long-term deviations of the model are observed.

3. Fluxes at the lower boundary of the outer belt (around L^*=4) follow a profile reasonably similar to observations. This suggests that plasmaspheric hiss is quite well-represented by the model. There is still some over-estimation of fluxes near the lower boundary compared to observations, but that may be due to a general over-estimation of fluxes during periods of depletion.

To thoroughly test the long-term behaviour of the system, a year of magnetic activity was simulated. Figure 23 shows the VNC simulation for all of 2013, as well as Kp and Dst index variations. Although the Dst index does not drive the model, it provides a good indication of storm activity. It can be seen that the strongest geomagnetic storms in 2013 were around March (day 70), May-June (days 140-180) and November (320-340). The flux enhancements closely follow significant drops in Dst and rises in Kp index, although interesingly, the single biggest Kp index, registered in October, does not cause the model to predict high fluxes. The reasons for this were explored previously when that time period was analysed in detail.

The 2013 time period includes all the simulation time periods mentioned in this manuscript with the exception of January 2014 (the last month of the 3-month simulation discussed above). By comparing simulations for individual months with the results of the simulation for the whole year, any long-term effects will become apparent, especially considering that the August, September, October and November are all in the latter part of the year, after several months of simulation dynamics have elapsed. This leaves plenty of time for any long-term simulation effects to develop.

Figure 24 shows the effect of long-term simulation for the August 1-25, 2013 time period. The top surface plot shows the simulation run from August 1-25, 2013 (with one day of 'slack' before August 1); the bottom surface plot shows a segment from Figure 23 (bottom) corresponding to August 1-25, 2013. There

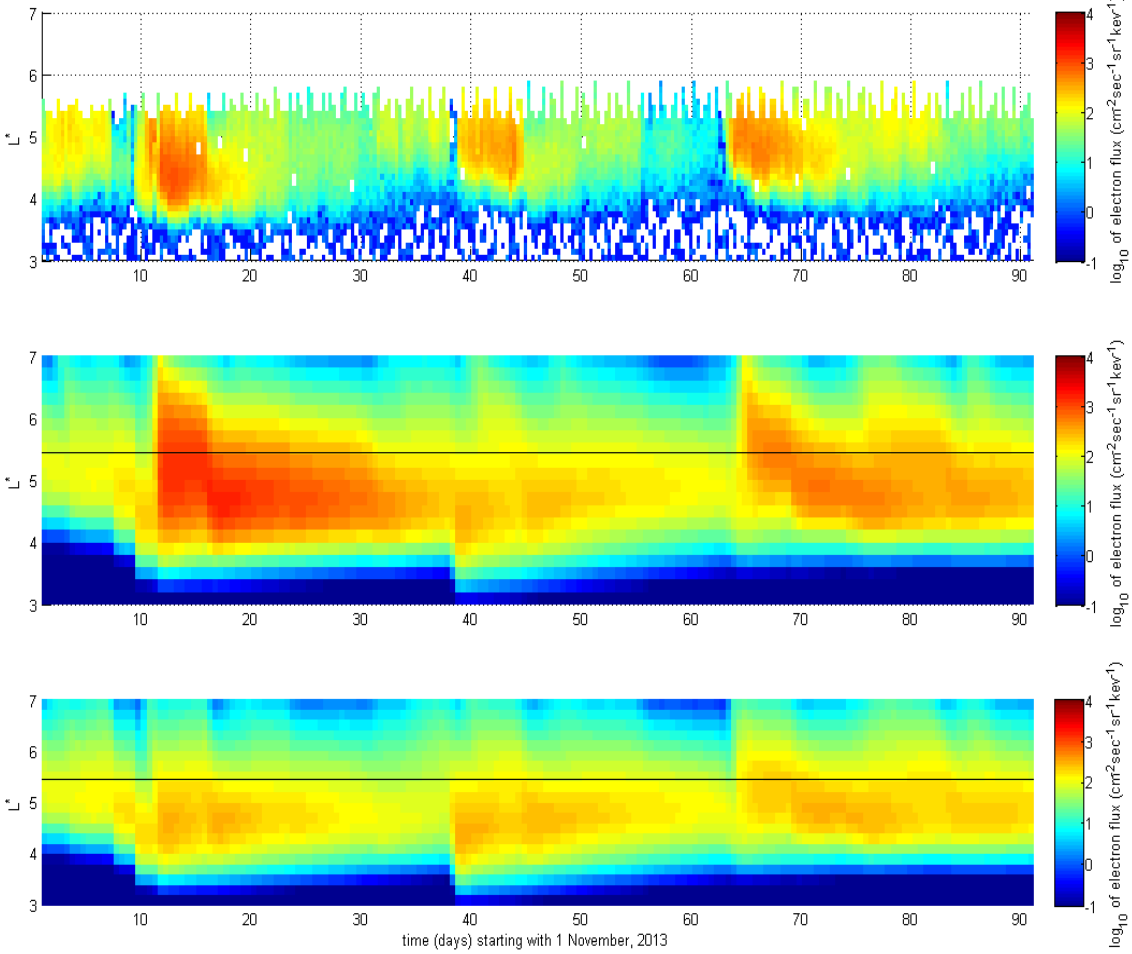

Figure 22: Electron fluxes for 891 keV electrons over a three-month period starting on 1 November, 2013: (a) Van Allen B MagEIS data, (b) VNC simulation and (c) VNC with GOES-13 instead of NARMAX used as the outer boundary. The black lines in (b) and (c) denote the location of the approximate radial apogee of the Van Allen B satellite orbit.

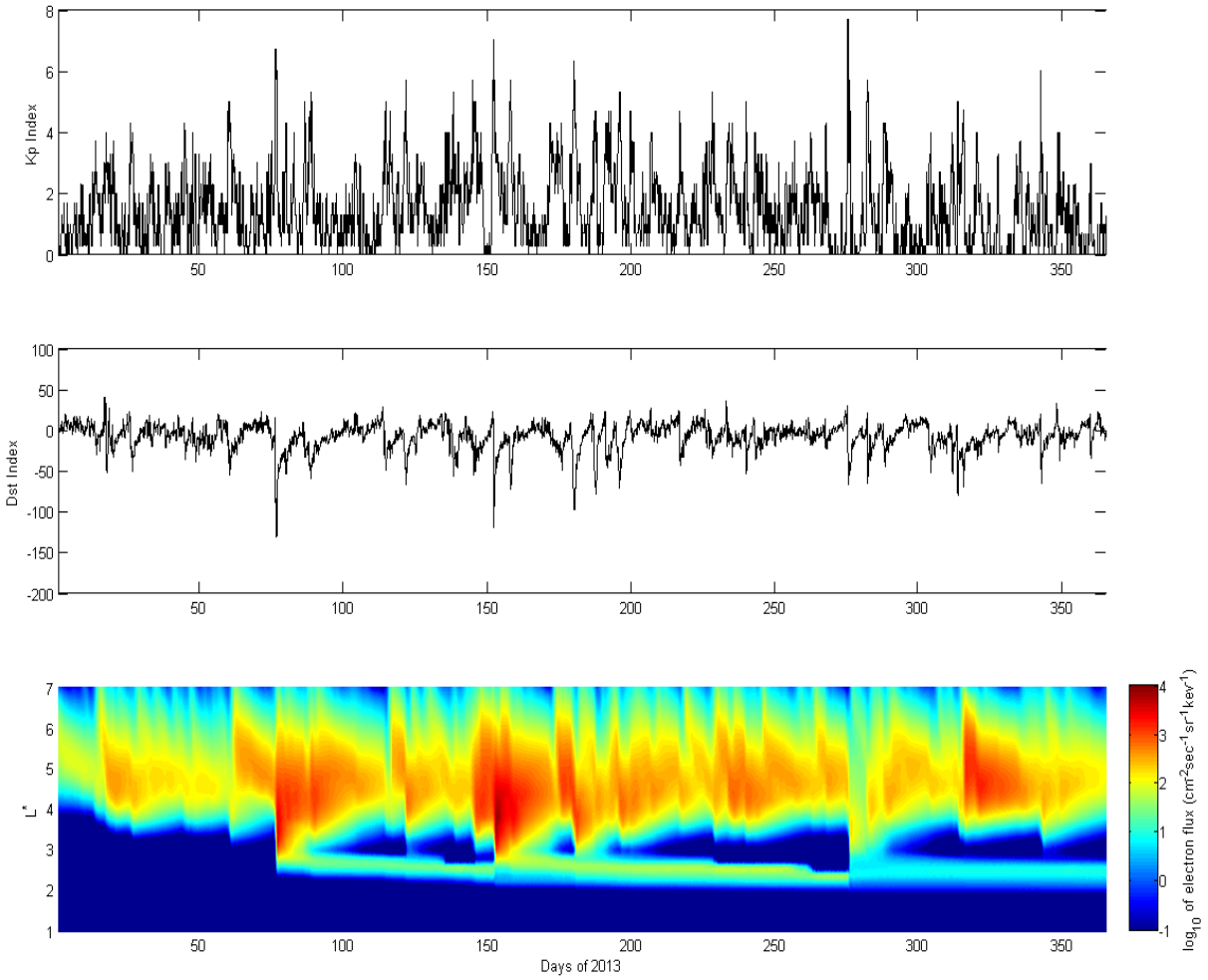

Figure 23: (a) Kp idnex, (b) Dst index and (c) differential electron flux for 891 keV, for the year 2013.

are two types of differences between these diagrams. First of all, it can be seen that the flux at L^*=4-6 is higher on the bottom panel for the first ten days of the simulation, compared to the top panel. This effect was discussed previously - while in the top panel, the model is still filling in the simulation space with fluxes, in the bottom panel, fluxes have already stabilised long ago and are representative from the first day. It is useful to note that this does not appear to affect GSO (which is around $L^* = 6$ and upwards), but has a significant impact in the heart of the radiation belt.

The second difference can be seen looking at the outer boundary ($L^* = 7$). The top panel has sharper gradients. This is an artificial effect - because the simulation for all of 2013 was so resource intensive, it was decided to plot it with a lower time resolution. The interpolation was thus performed between fewer data points. It can be seen that, inside the radiation belt, fluxes are virtually identical after about 10-15 days.

Figure 25 shows the same information for the period September 1-23, 2013. Again, prior fluxes are seen to persist in the bottom panel, while initially much lower in the top panel. As before, the changes do not appear to spread to geostationary orbit, and the flux profiles become very similar after about 15 days.

Finally, figure 26 shows the October 1-20, 2013 time period. Here the two simulations converge sooner because of rapid depletions due to the dramatic geomagnetic conditions. Fluxes that persist before the simulation disappear after the first storm event or get adiabatically transported out of the energy range under observation. The simulations are essentially the same after 5-10 days. The conclusion here is that the quieter the geomagnetic conditions, the more prior fluxes have an effect on the simulation accuracy.

Figures 27 to 30 show the geostationary orbit fluxes for the four quarters of 2013 for $>$ 800 keV electrons, compared to GOES-13 observations. In the first quarter, apart from the large discrepancy between days 1-15, the model (red) mostly tracks the observations (blue), although the variation of the observations is consistently larger than that of the model. This is a natural consequence of using integral daily fluxes as an input instead of their hourly values - dropouts and enhancements alike will be smoothed. In the second quarter, VNC over-estimates fluxes between days 100-114 by about an order of magnitude. A data gap exists around days 140-150, and the model generally tracks the variations apart from the aforementioned time period. One important feature is the exaggeration of diurnal changes in particle flux by the model. This may be a consequence of the magnetic field model used. Model performance generally degrades in the third quarter, which features many periods of enhancments and dropouts. The model does exhibit variation, but it is far less than the observations indicate. Nevertheless, the model responds to variations and exhibits large variance in this quarter. Finally in the last quarter, the model under-estimates fluxes for the period 274-280 (this is the October 2013 period studied previously) and over-estimates fluxes by around half an order of magnitude on days 315-335. A flux dropout following days 358-359 is also unaccounted for. The prediction efficiency for the whole of 2013 is 0.1277.

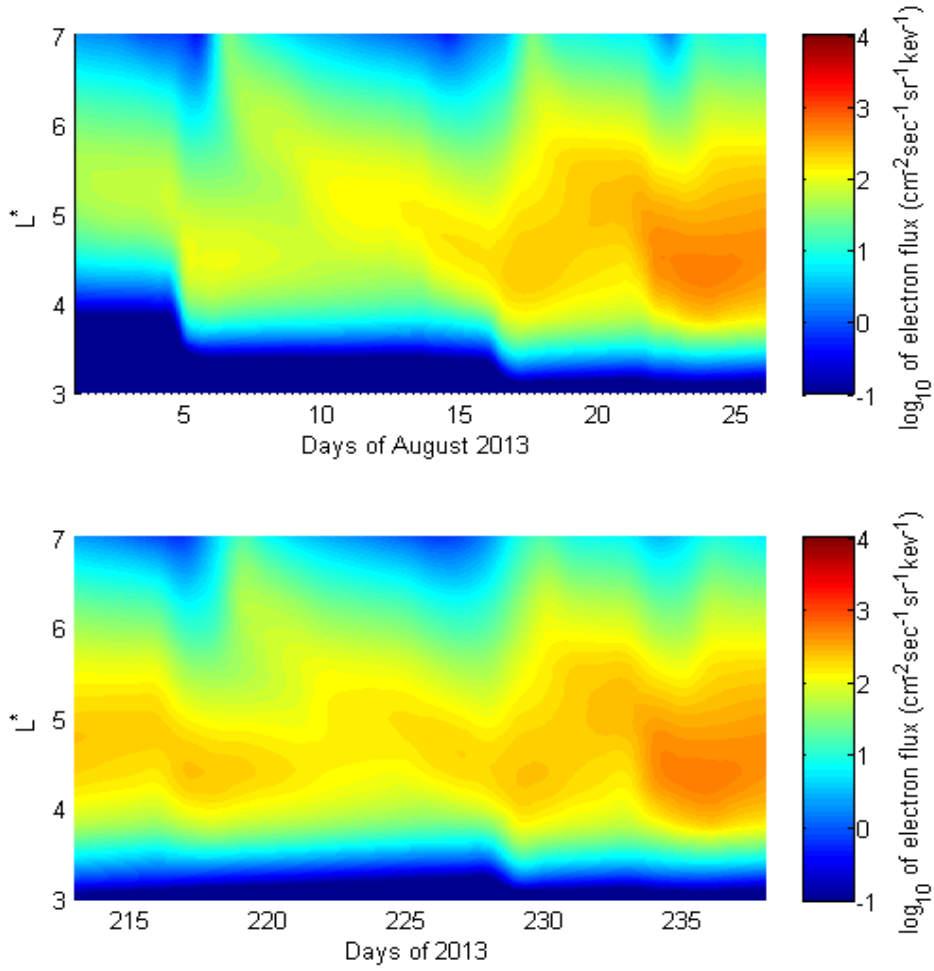

Figure 24: VNC simulation for differential fluxes at 891 keV for the August 1-25 period, run from the beginning of August (top) and from the beginning of 2013 (bottom).

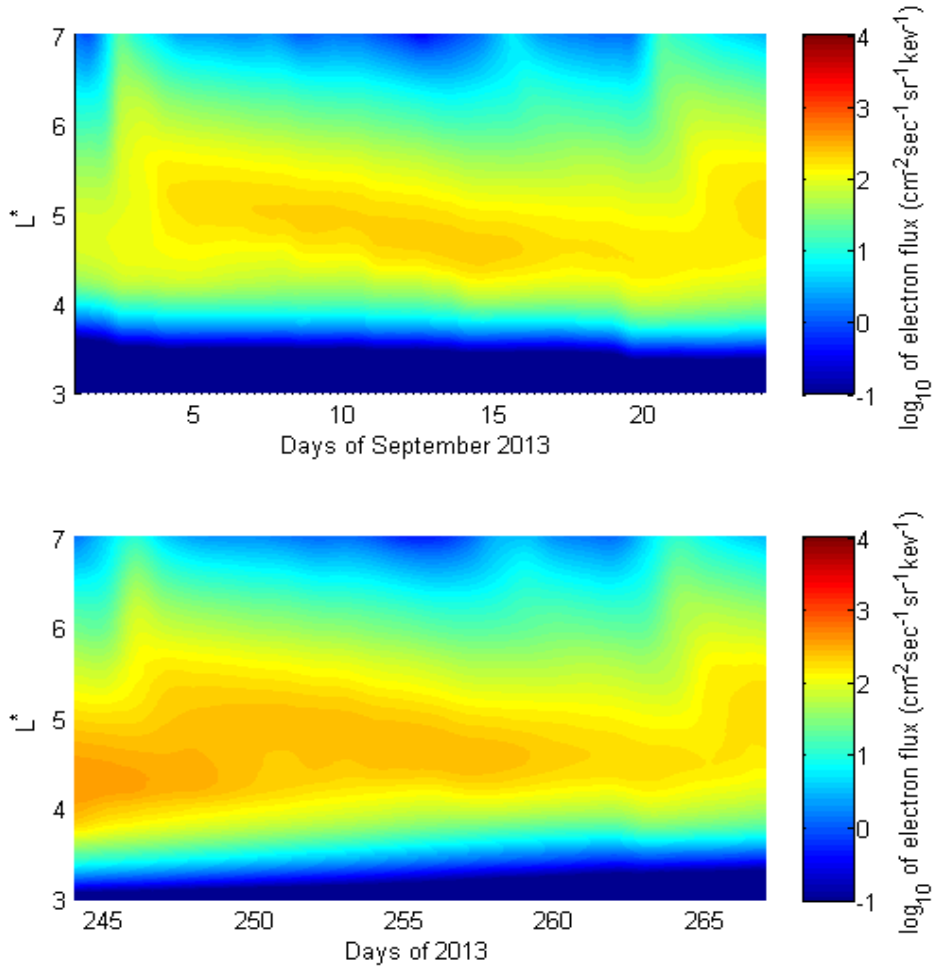

Figure 25: VNC simulation for differential fluxes at 891 keV for the September 1-23 period, run from the beginning of September (top) and from the beginning of 2013 (bottom).

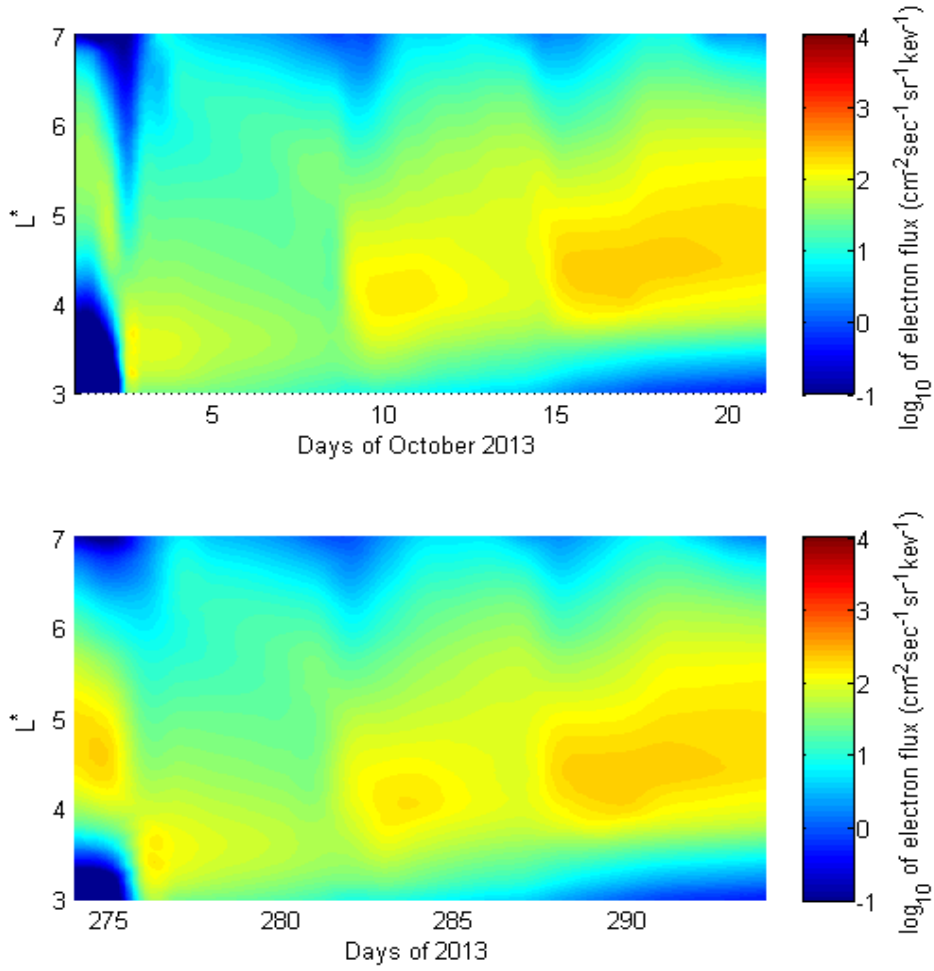

Figure 26: VNC simulation for differential fluxes at 891 keV for the October 1-20 period, run from the beginning of October (top) and from the beginning of 2013 (bottom).

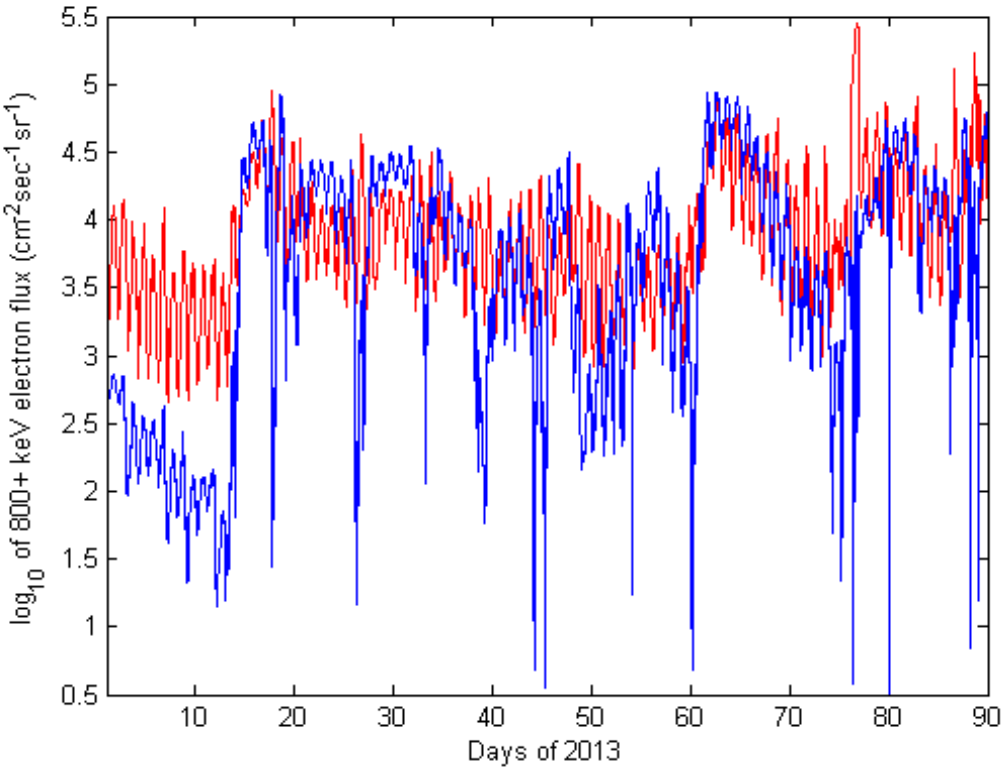

Figure 27: Flux of > 800 keV electrons observed on GOES-13 (blue), flux modelled by VNC (red) for the first quarter of 2013.

.

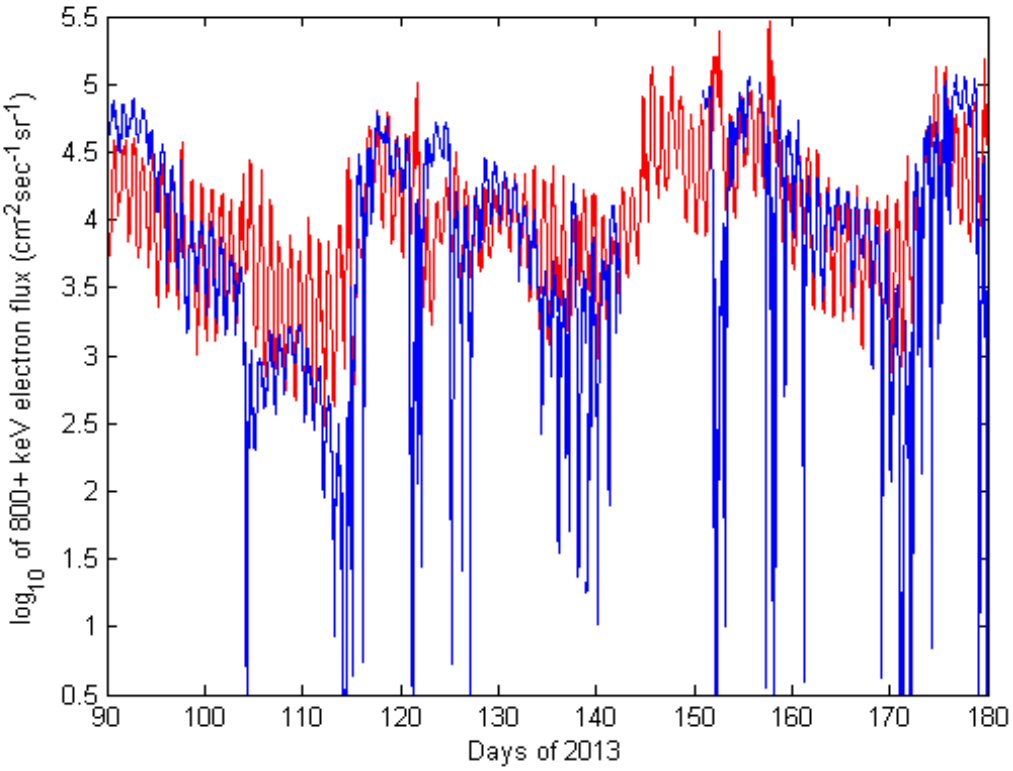

Figure 28: Flux of > 800 keV electrons observed on GOES-13 (blue), flux modelled by VNC (red) for the second quarter of 2013.

.

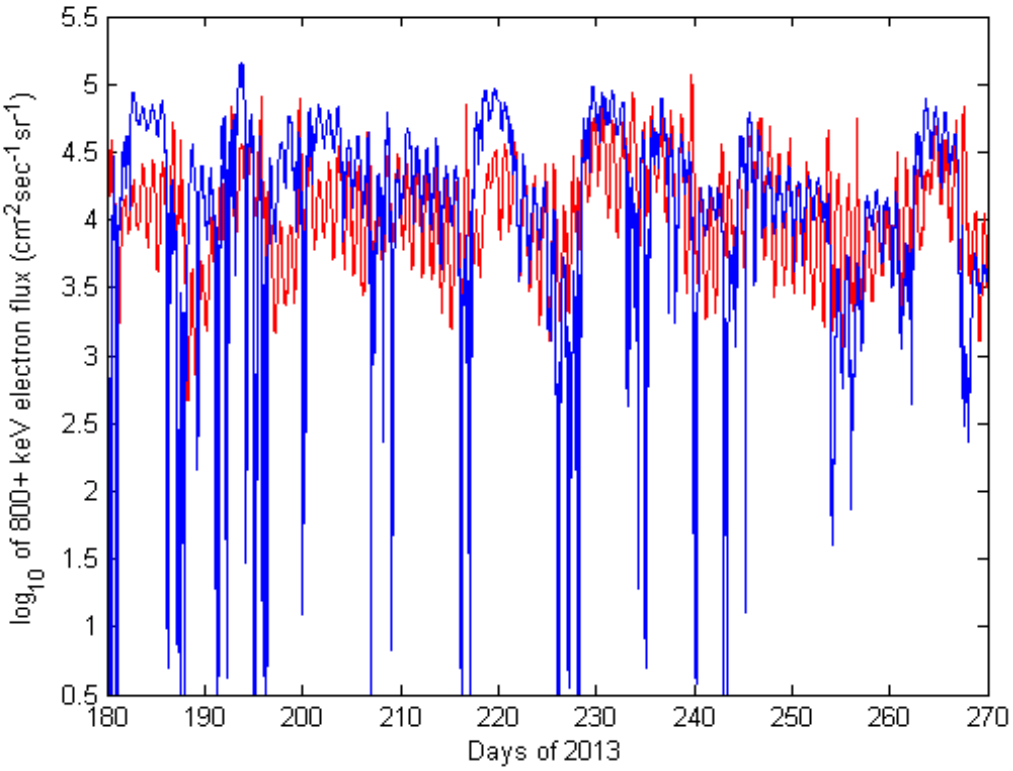

Figure 29: Flux of > 800 keV electrons observed on GOES-13 (blue), flux modelled by VNC (red) for the third quarter of 2013.

.

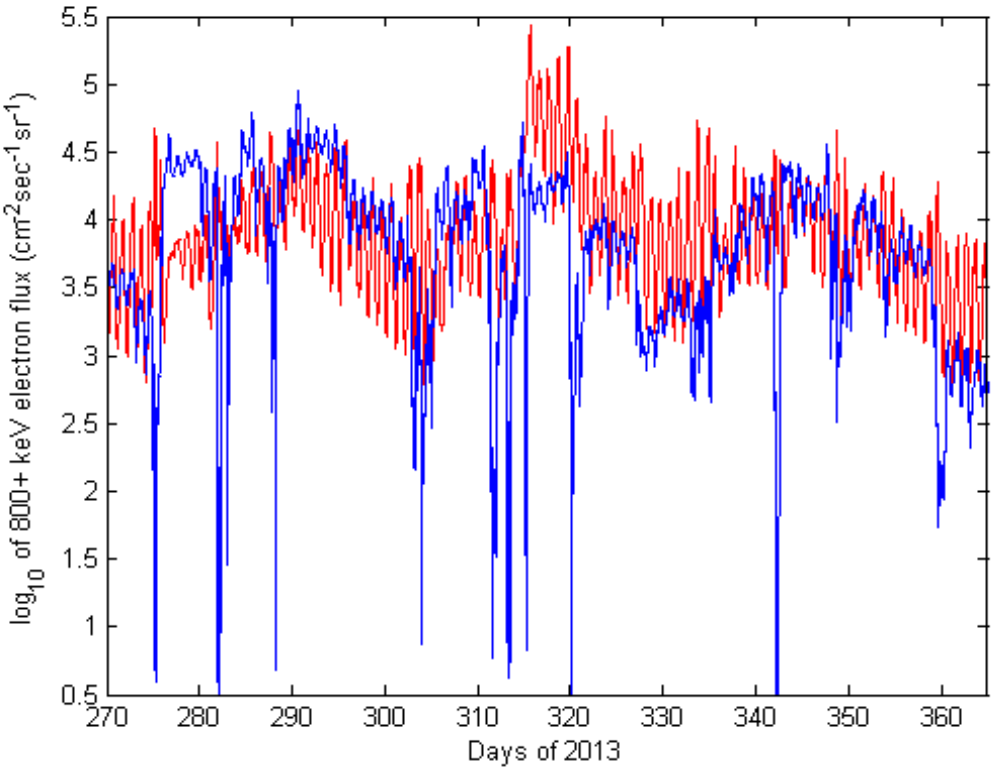

Figure 30: Flux of > 800 keV electrons observed on GOES-13 (blue), flux modelled by VNC (red) for the fourth quarter of 2013.

.

Variations exist between the GSO model data for the yearly simulation run and the smaller weekly time periods (August 1-25, September 1-23, October 1-20) analysed previously. However, they are insignificant and are not indicative of any long-term effect. Rather, they are the result of lower flux profile time resolution and the associated interpolation effects. In addition, the Kp index used as an input to both the model and the magnetic field is taken from a different library than the one used in the simulation. Small variations between Kp indices from several data archives have been observed and this can have a minor impact on model output.

3.8 Sensitivity to wave model parameters

Figure 31 shows results obtained for the same time period as Figure 7 with the dayside chorus diffusion coefficients are multiplied by 2. As well as local acceleration, chorus waves cause pitch angle scattering. It can be seen on Figure 31 (c) that in this case the dropouts are much more pronounced. Figure 32 shows the same information for the 1-23 September 2013 time period. Here, the two areas of increased particle flux are also much more in agreement with the observations. Finally, Figure 33 shows the 1-20 October 2013 time period with enhanced dayside chorus.

It is unlikely that magnetopause shadowing was the source of electron losses in September, given the relatively benign geomagnetic environment, and so the low flux levels observed on days 13-19 may have been caused by pitch angle scattering by plasma waves. EMIC waves were turned off in the VERB simulation, and in any case are not believed to significantly affect electrons below 1 MeV. Enhanced dayside chorus, on the other hand, evidently reproduces the orbserved dynamics and is a tempting candidate. This experiment was done to demonstrate how changing the physics-based wave model can affect electron fluxes around L^*=4-5. As was mentioned previously, the wave model and its diffusion coefficients are constantly updated and improved using statistical wave data from observations on various space satellites.

3.9 Summary

The data-driven NARMAX system was coupled with the physics-based VERB code to produce the VNC (VERB-NARMAX Coupled) model. This was done by using NARMAX-predicted integral daily fluxes for $>$ 800 keV and $>$ 2 MeV electrons to form an input to the VERB variable outer boundary, which together with the Kp index provided all the input parameters necessary to drive the simulation. In essence, instead of using a convection code, VERB was initialised with predicted high-energy geostationary orbit fluxes. Fluxes were translated from the average GSO position to the outer simulation boundary by assuming conservation of the first adiabatic invariant and a cosntant phase space density between GSO and L^*=7.

Three time periods were chosen for an in-depth study and simulated by VNC: a period of moderate geomagnetic activity (1-25 August, 2013), low activity (1-

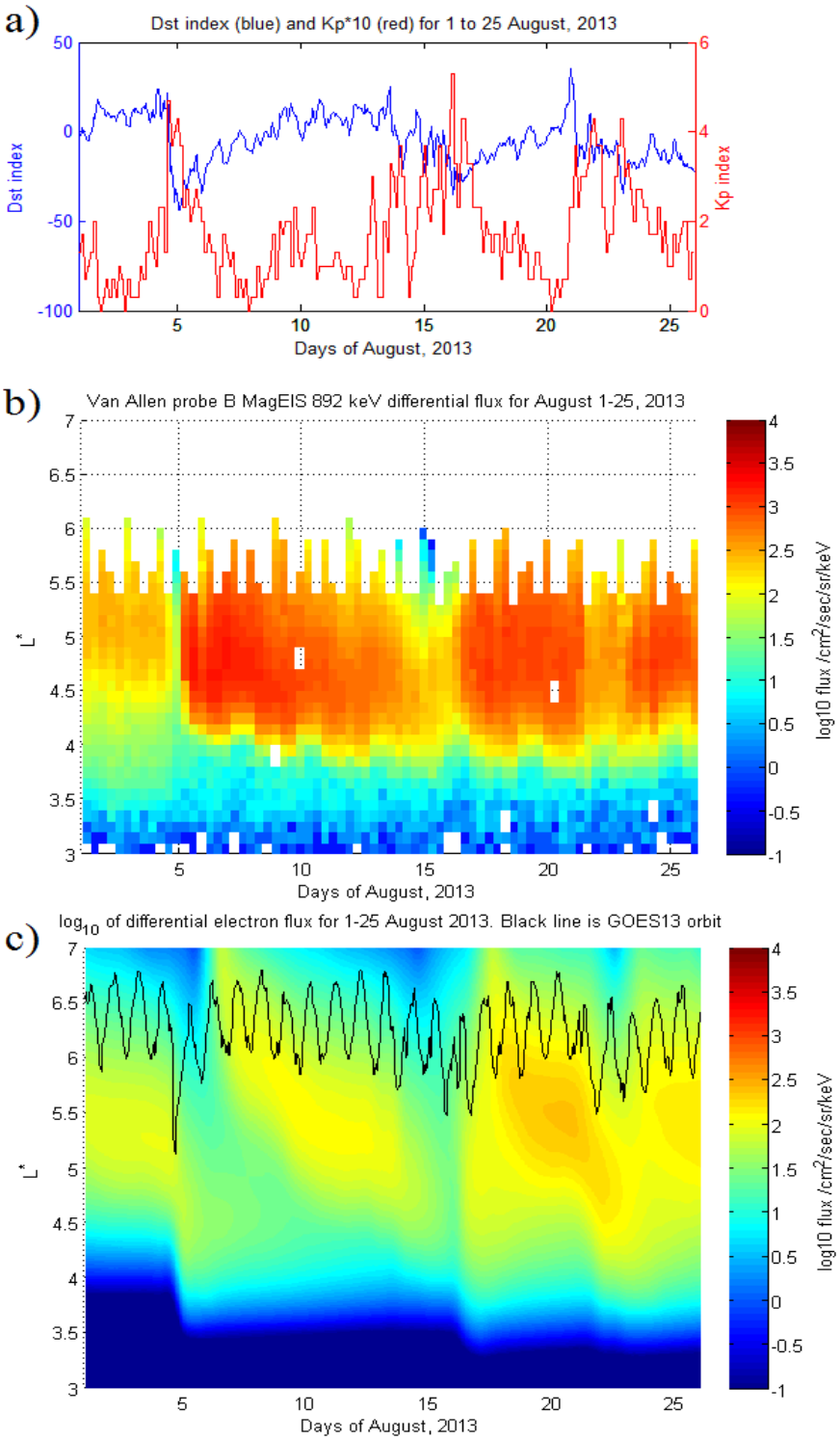

Figure 31: For 1-25 August 2013, a) Dst and Kp indices b) Van Allen probe B MagEIS data for 892 keV, c) VERB simulation of the outer radiation belt using the NARMAX-derived differential flux as the outer boundary, for $\times 2$ enhanced dayside chorus. Black curve in c) represents geostationary orbit.

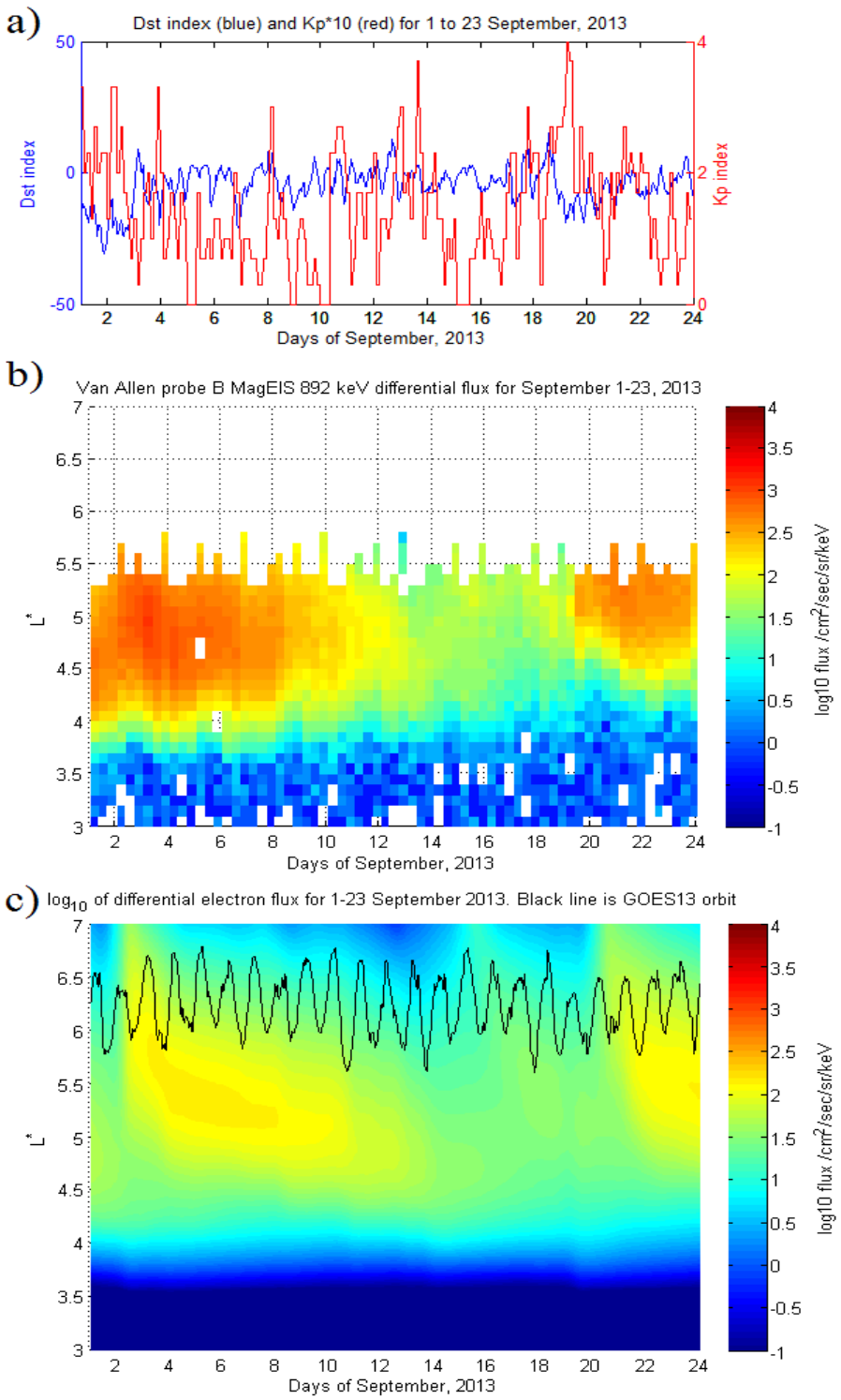

Figure 32: For 1-23 September 2013, a) Dst and Kp indices b) Van Allen probe B MagEIS data for 892 keV, c) VERB simulation of the outer radiation belt using the NARMAX-derived differential flux as the outer boundary, for $\times 2$ enhanced dayside chorus. Black curve in c) represents geostationary orbit.

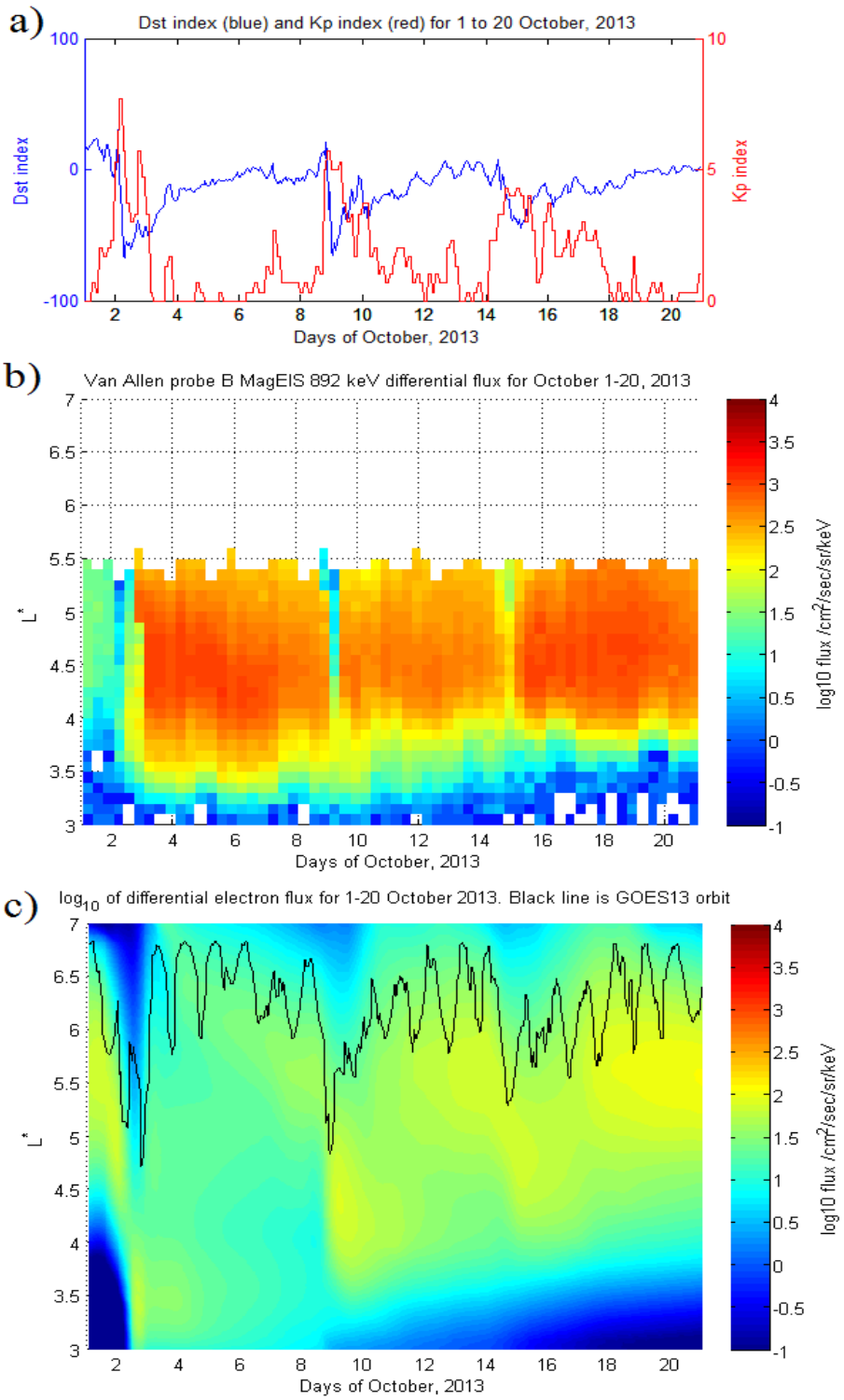

Figure 33: For 1-20 October 2013, a) Dst and Kp indices b) Van Allen probe B MagEIS data for 892 keV, c) VERB simulation of the outer radiation belt using the NARMAX-derived differential flux as the outer boundary, for $\times 2$ enhanced dayside chorus. Black curve in c) represents geostationary orbit.

23 September, 2013) and relatively high activity (1-20 October, 2013). The results of the simulations were compared to Van Allen probe particle detector (MagEIS) data for the whole outer belt, and to GOES-13 flux data at geostationary orbit. To do that, the fluxes were converted from differential into integral form by assuming a exponential distribution as a function of energy. The simulation results were seen to broadly replicate the observations, capturing the major changes to flux levels and being in reasonable quantitative agreement. Discrepancies were discussed in the relevant subsections. It was shown that it is possible to predict outer radiation belt dynamics by using high-energy channel electron flux data from GSO as an input.

Simulation results were analysed for both low and high energies. It was found that VNC over-estimates electron losses at low energies inwards of L^*=4 but otherwise models the flux dynamics reasonably well. At high energies, simulated fluxes around L^*=4 steadily increase with time in contradiction of observations. This is most likely the result of EMIC waves not being included in the wave model, as well as a lack of adequate representation for magnetopause shadowing.

The model was initialised with the boundary flux derived from GOES-13 integral daily fluxes as opposed to NARMAX predictions of them. This was done to check the validity of the scheme by eliminating any uncertainties caused by NARMAX. The results did not have the time lag sometimes associated with NARMAX, but under-estimated fluxes even further compared to observations. This was attributed to the daily integral nature of the fluxes, which smoothes out hourly gradients in the outer boundary. As a result, the model under-estimates fluxes during enhancements and over-estimates fluxes during dropouts. Because NARMAX sometimes over-estimates fluxes during rapid enhancements, it partially compensates for this effect.

A long-term simulation was performed encompassing the whole of 2013. This was done to test for any long-term simulation effects. No long-term flux build-up or depletion effects were found for the energy of 891 keV (in contrast to results for higher energies that were discussed previously). The time periods analysed previously (1-25 August, 1-23 September and 1-20 October, 2013) as stand-alone simulations were compared with the same time periods taken from long-term simulation. Results at geostationary orbit were very similar, but significant differences were observed in the heart of the outer belt around $L^* = 4$. These were due to flux from previously simulated time periods being carried over into the time period of study. The differences were more pronounced during quiet periods. It was concluded that any VNC simulation should be run with around 10-15 days of simulation time before the time period of interest included. This 'slack' time period should be initialised with representative input parameters. Geostationary orbit data for all of 2013 was also obtained and compared to GOES-13 observations. Inaccuracies were outlined in the relevant section.

The same three time periods mentioned previously were re-simulated with increased chorus wave diffucion coefficients. The results were more qualitatively similar to observations than if the original simulation results, but the magnitude of the simulated fluxes was lower. It was concluded that pitch-angle scattering by local instabilities around L^*=4 is underestimated in the original VNC model.

Increased chorus coefficients (which also cause pitch-angle scattering) were able to reproduce the flux drop more effectively.

4 Chapter 4: VNC-S - data-driven radiation belt modelling

4.1 Scaling the VERB matrix for improved performance at GSO

To improve predictions at geostationary orbit, it is possible to simply scale the flux matrix by weighted averages of the NARMAX values. This makes no sense from a physics point of view, so it is not suitable to extracting information about electron fluxes in the heart of the radiation belts. The reason it works near GSO is as follows. The flux density decreases gradually as a function of radial distance. That is why flux varies depending on time of day - near noon MLT as the spacecraft enters field lines that are closer in L^* to the heart of the radiation belts, fluxes maximise. This diurnal change is one influence on flux variability, the other influence being large-scale variations as a result of storm activity which is captured by NARMAX. Therefore, by scaling the whole matrix by weighted NARMAX values, both the diurnal variations captured by VERB and the storm activity captured by NARMAX can be represented.

The methodology is as follows:

1. generate the flux profile for near the energy desired (so all essential physical processes for that energy are captured). For flux $>$ 800 keV, the profile would be generated for 800 keV, for flux $>$ 2 MeV, the energy used will be 2 MeV.

2. split the flux matrix generated in the standard manner by VNC into separate days

3. for each day, find the mean daily flux by taking hourly predicted flux values at GSO and averaging them

4. divide each value in the 24-hour period by this average

5. multiply all of the normalised values in the 24-hour period by weighted averages of relevant NARMAX predictions. For example, the value at 0100 UT is multiplied by an average between the current day's NARMAX prediction and yesterday's NARMAX prediction. The normalised flux at 1200 UT is multiplied by the NARMAX prediction for the current day, the value at 2300 UT is multiplied by an average of the current day and the future day NARMAX predictions, etc. If real GOES-13 data of total flux for the previous day is available, that can be used instead of the previous day's predicted flux.

6. repeat for the next 24-hour period, and so on until the whole time segment is covered.

The scaling method works because it is primarily driven by NARMAX (the VERB matrix essentially only provides a measure of diurnal flux variations). In turn, NARMAX is better suited for predicting compression events (because it uses L1 solar wind data among its inputs). The VERB code and magnetic field model used are both driven by the Kp index which only registers compression events implicitly through their effect on the Earth's magnetic field. Therefore adiabatic acceleration and the Dst effect may be better accounted for with the

data-driven NARMAX. In particular it will be shown that the version of VNC with scaling is better at forecasting rapid rises in flux that occur as a result of compression events. Also, using real GOES-13 integrated flux data for the day before results in superior performance in forecasting dropouts: the hours 0100-1100 UT are influenced by real data rather than the simulation. Since real data by definition registers dropouts better than the simulation, this can reduce the delay in registering such a depletion.

In general, it is better to use the standard VNC scheme for radiation belt forecasting and particularly to obtain data inwards of GSO. It is physically more robust and agrees better with Van Allen probes data; the scaled version of VNC (or 'VNC-S') has no physical meaning outside GSO. However, for GSO the scaled version offers better performance. Conceptually, scaling leans the data-physics coupled model more heavily in favour of the data part of it - specifically, NARMAX - which offers superior performance near the NARMAX operating parameters at the cost of reduced performance everywhere else.

4.2 Magnetic field models

The choice of magnetic field model is crucial for the accuracy of the results, because the scaling is performed based on flux values obtained using the magnetic field models. As such, magnetic field models are used twice - once to calculate integral flux over 24 hours from the original profile, and then again to obtain the GSO flux for the same time period, this time from the scaled profile. As such, a comparative investigation has been performed using the same three time periods as in Chapter 3 - August 1-25, 2013, September 1-23, 2013, and October 1-20, 2013. The models used were those in the IRBEM library which only relied on the Kp index for inputs. It is believed that models which rely on more parameters such as Dst and solar wind measurements may give even more accurate results, but in order to keep the generality of the model (two inputs only), only Kp-driven ones were used. Also, the effects of smoothing the flux profile (i.e. having a running average of 24 data points instead of a fixed average of hours 0100-2400 per day) were investigated.

An example of a smoothed and unsmoothed profile can be seen on Figure 34 where (a) is the original profile for August 1-25, 2013, (b) is the unsmoothed profile, and (c) is the smoothed profile. The lines seen below L^*=3 in Figure 34 (b) and (c) are not a physical effect but are a consequence of the scaling. It can be seen that smoothing (Figure 34 (c)) removes sharp edges between consecutive days which would translate into sharp jumps on the model output as the spacecraft crosses 00 UT. These jumps exist because NARMAX is calculated and released every 24 hours at 00 UT. Furthermore, in Figure 34 (b) the averaging by which each data point in the 24-hour set is divided is calculated from those 24 data points, and so the normalisation at 2300UT will be different than at 00 UT. Both these factors cause sharp 'ledges' as the model switches to the next day. This is non-physical and, as will be shown later, degrades model performance. Sharp 'ledges' can also be seen on Figure 34 (c) (for example, on Day 5-6), but this is related to the changing NARMAX integral flux value.

This does have some physical significance, as these sharp flux enhancements do indeed happen. It can be seen on Figure 6, where GSO flux rises rapidly.

The VNC-S model efficiency was tested for different magnetic field models using the prediction efficiency parameter [e.g. Li, 2004]:

$$PE = (1 - \frac{\chi^2}{\Lambda^2}) \times 100\% \tag{29}$$

where χ is the difference between the model output and observations summed over all data points ($\chi^2 = \frac{1}{N}\sum_{i}^{N}[log_{10}(j_i^{model}) - log_{10}(j_i^{obs})]^2$ where N is the number of data points, j_i^{model} is the ith datapoint from the simulation, and j_i^{obs} is the corresponding observed datapoint). Λ is a measure of the spread of the data ($\Lambda^2 = \frac{1}{N}\sum_{i}^{N}[log_{10}(j_i^{obs} - <log_{10}(j^{obs})>)]^2$) where $<log_{10}(j^{obs})>$ is the mean of the logarithms of all data points in the set.

The results for the three time periods analysed previously are displayed on Table 1. The graphs showing the data vs. VNC-S outputs for 2+ MeV flux using the various field models for the three time periods, first without smoothing and then with smoothing, can be seen on Figures 35-36, 37-38 and 39-40 for August 1-25, September 1-23 and October 1-20, 2013 respectively. The following conclusions can be drawn from the results. Firstly, the [Fairfield and Mead, 1975] and [Tsyganenko, 1989] models provide the best results in all cases. This supports earlier work [e.g. Donovan and Rostoker, 1991]. That study simulated magnetospheric convection and found that the [Tsyganenko, 1989] model agreed with results better than the [Tsyganenko, 1987], particularly for higher Kp indices. For this reason [Tsyganenko, 1989] is used throughout the study unless otherwise stated. Secondly, smoothing has the effect of slightly improving the prediction efficiency. Thirdly, the prediction efficiency depends on geomagnetic conditions - during the August 1-25, 2013 period, which saw quite large and rapid enhancements, the prediction efficiency hovers around 40-50 %. During September 1-23, 2013, which featured a relatively benign geomagnetic environment with only one sudden enhancement (on September 20, 2013), the prediction efficiency rises to 70-80 %. During October 1-20, 2013, with its high changes in flux, prediction efficiency is lowest, around 30 %. It is important to notice that even in the storms such as October 2-3, 2013, the VNC-S model responds faster than the classic VNC, minimising the difference between model output and observations. This will be explored in more detail below, where a direct comparison will be made between VNC and VNC-S for geosynchronous orbit.

Looking at Figure 35 vs. Figure 36 it is possible to see the role of the smoothing algorithm. Sharp spikes are present in data around August 6-7, 2013, in Figure 35 model output which are absent on Figure 36. These ridges are a result of different normalisation coefficients for different days, and cause the model to first over-estimate the flux, and then to rapidly lower its forecast with no physical reason to do so. The smoothing brings model output more

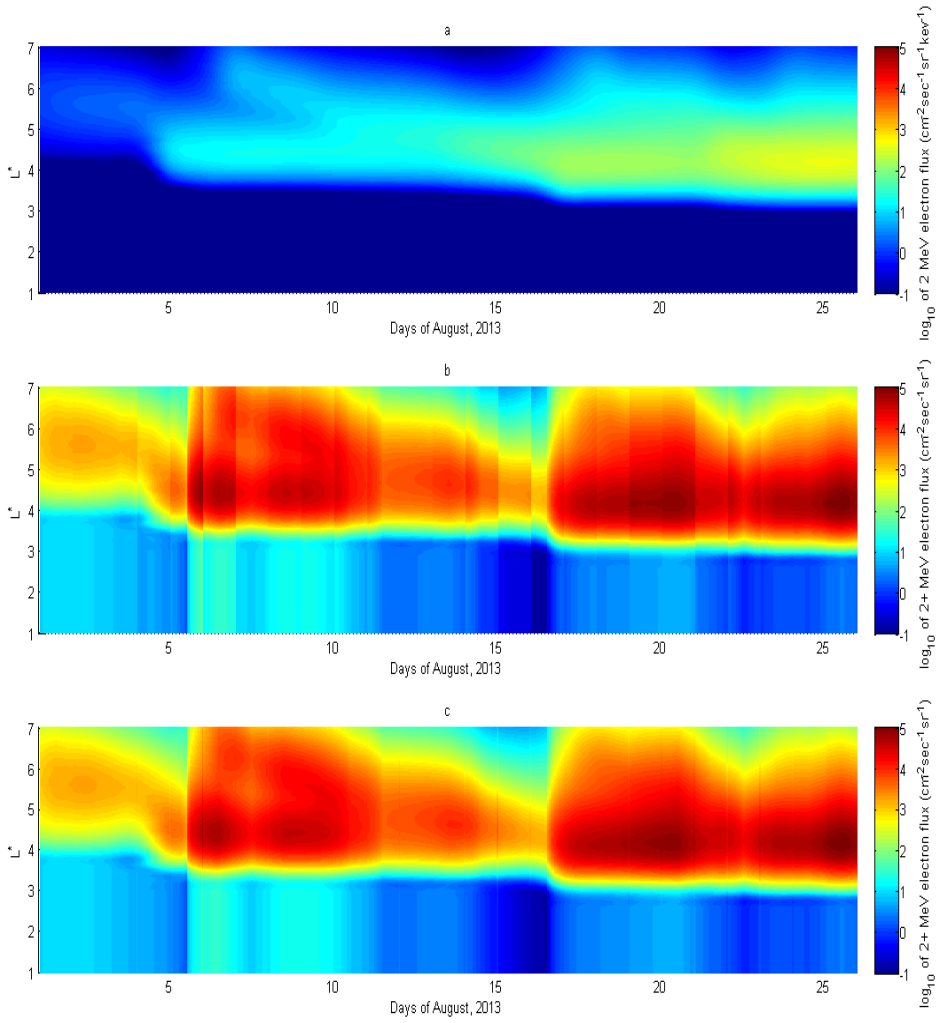

Figure 34: Flux profile for 1-25 August, 2013 (a) from VNC (differential flux at 2 MeV), (b) VNC-S integral flux > 2 MeV without smoothing, and (c) VNC-S integral flux > 2 MeV with smoothing applied.

August 1-25, 2013

with smoothing

Magnetic field model	PE (> 2 MeV)	PE (> 800 keV)
No external field	0.3165	0.3826
[Fairfield and Mead, 1975]	0.4957	0.4879
[Tsyganenko, 1987, (short)]	0.4945	0.4700
[Tsyganenko, 1987, (long)]	0.4299	0.4592
[Tsyganenko, 1989]	0.5129	0.4894

without smoothing

Magnetic field model	PE (> 2 MeV)	PE (> 800 keV)
No external field	0.3022	0.3833
[Fairfield and Mead, 1975]	0.4893	0.4888
[Tsyganenko, 1987, (short)]	0.4921	0.4726
[Tsyganenko, 1987, (long)]	0.4210	0.4464
[Tsyganenko, 1989]	0.5111	0.4901

September 1-23, 2013

with smoothing

Magnetic field model	PE (> 2 MeV)	PE (> 800 keV)
No external field	0.6243	0.4960
[Fairfield and Mead, 1975]	0.7643	0.6354
[Tsyganenko, 1987, (short)]	0.7878	0.6463
[Tsyganenko, 1987, (long)]	0.7153	0.5901
[Tsyganenko, 1989]	0.7988	0.6522

without smoothing

Magnetic field model	PE (> 2 MeV)	PE (> 800 keV)
No external field	0.6072	0.4795
[Fairfield and Mead, 1975]	0.7501	0.6195
[Tsyganenko, 1987, (short)]	0.7766	0.6364
[Tsyganenko, 1987, (long)]	0.7136	0.5820
[Tsyganenko, 1989]	0.7912	0.6460

October 1-20, 2013

with smoothing

Magnetic field model	PE (> 2 MeV)	PE (> 800 keV)
No external field	0.3203	0.5298
[Fairfield and Mead, 1975]	0.3265	0.5673
[Tsyganenko, 1987, (short)]	0.3739	0.5631
[Tsyganenko, 1987, (long)]	0.3194	0.5177
[Tsyganenko, 1989]	0.3033	0.4613

without smoothing

Magnetic field model	PE (> 2 MeV)	PE (> 800 keV)
No external field	0.2188	0.4944
[Fairfield and Mead, 1975]	0.2848	0.5383
[Tsyganenko, 1987, (short)]	0.3433	0.5606
[Tsyganenko, 1987, (long)]	0.3129	0.5348
[Tsyganenko, 1989]	0.2902	0.4544

Table 1: Prediction efficiency for various time periods and magnetic field models for VNC-S with and without applying the smoothing algorithm.

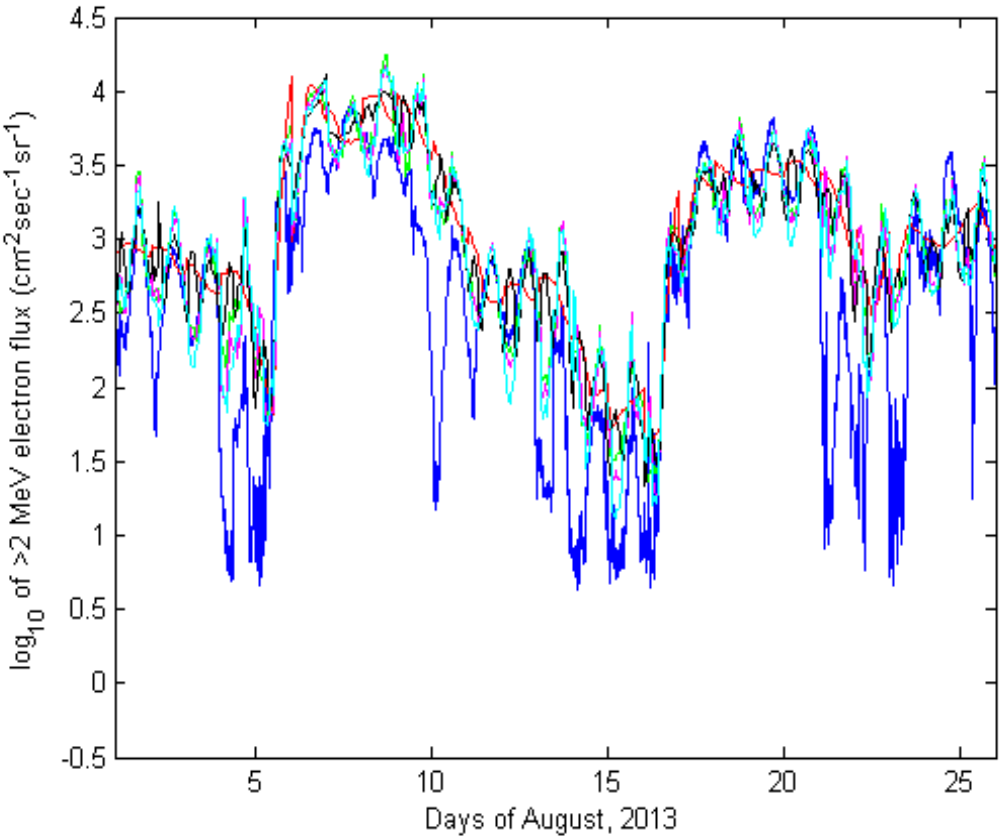

Figure 35: Flux of $>$ 2 MeV electrons observed on GOES-13 (blue) vs. flux simulated by VNC-S using various field models, for 1-25 August, 2013, without smoothing. Red signifies no external field, green is Fairfield and Mead [1975], magenta - Tsyganenko [1987, short], black - Tsyganenko [1987, long], cyan - Tsyganenko [1989].

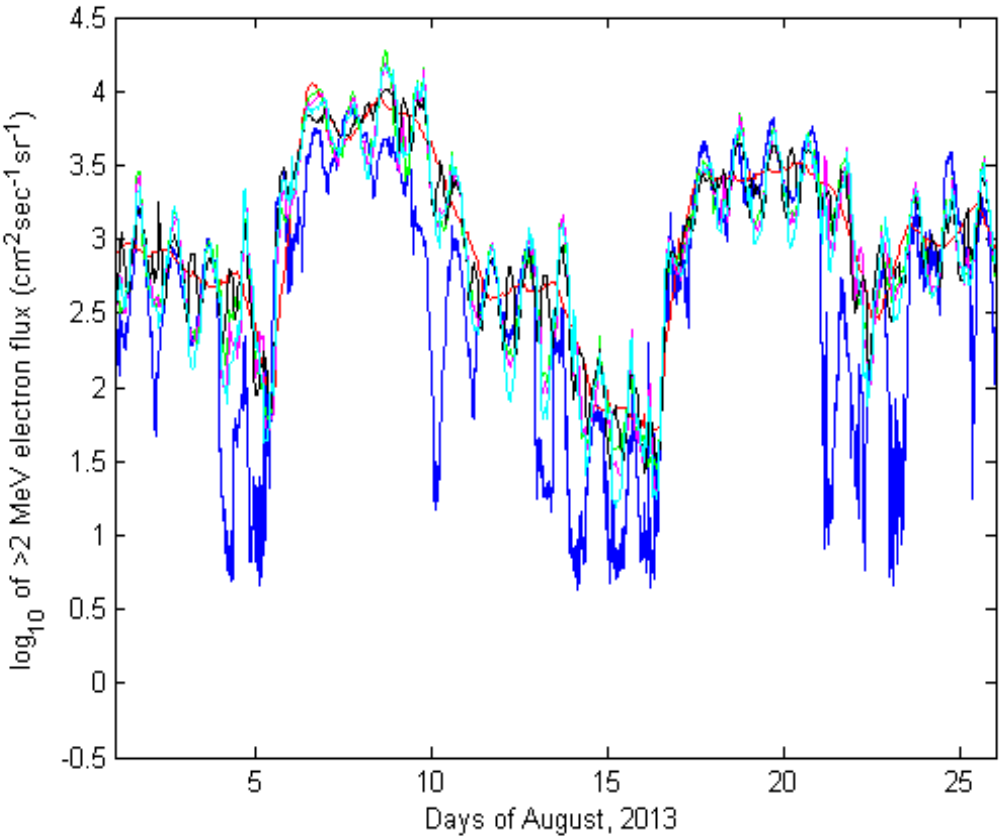

Figure 36: Flux of $>$ 2 MeV electrons observed on GOES-13 (blue) vs. flux simulated by VNC-S using various field models, for 1-25 August, 2013, with smoothing applied. Red signifies no external field, green is Fairfield and Mead [1975], magenta - Tsyganenko [1987, short], black - Tsyganenko [1987, long], cyan - Tsyganenko [1989].

.

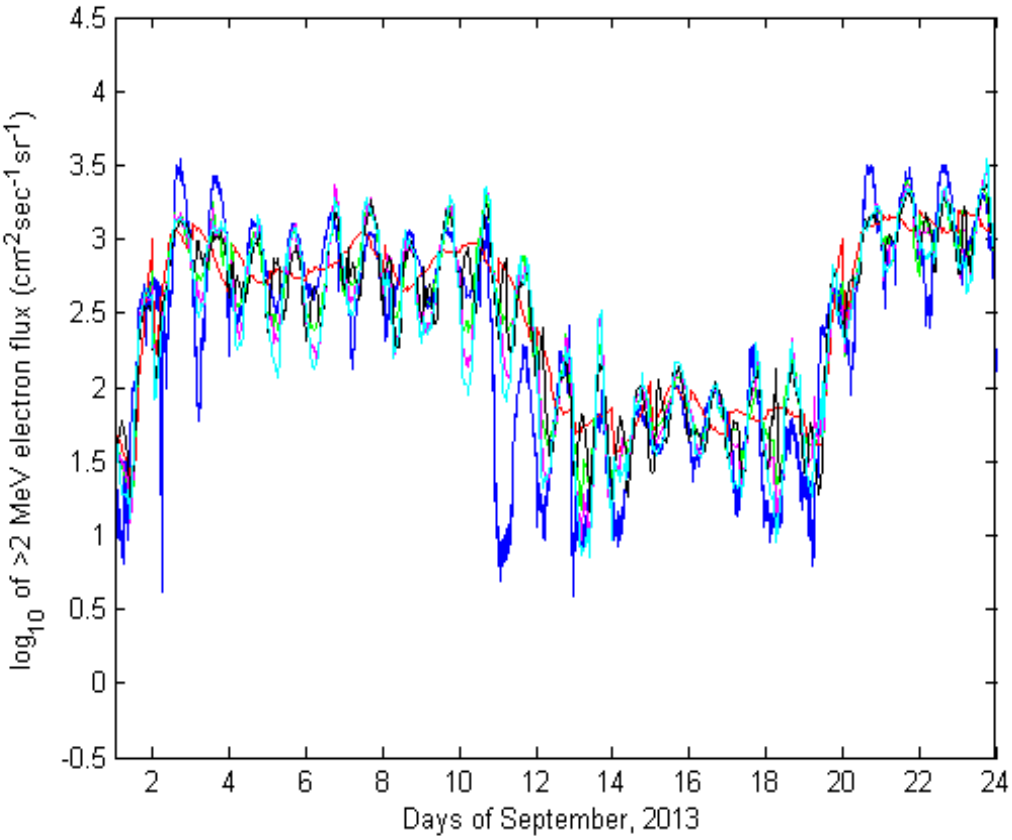

Figure 37: Flux of > 2 MeV electrons observed on GOES-13 (blue) vs. flux simulated by VNC-S using various field models, for 1-23 September, 2013, without smoothing. Red signifies no external field, green is Fairfield and Mead [1975], magenta - Tsyganenko [1987, short], black - Tsyganenko [1987, long], cyan - Tsyganenko [1989].

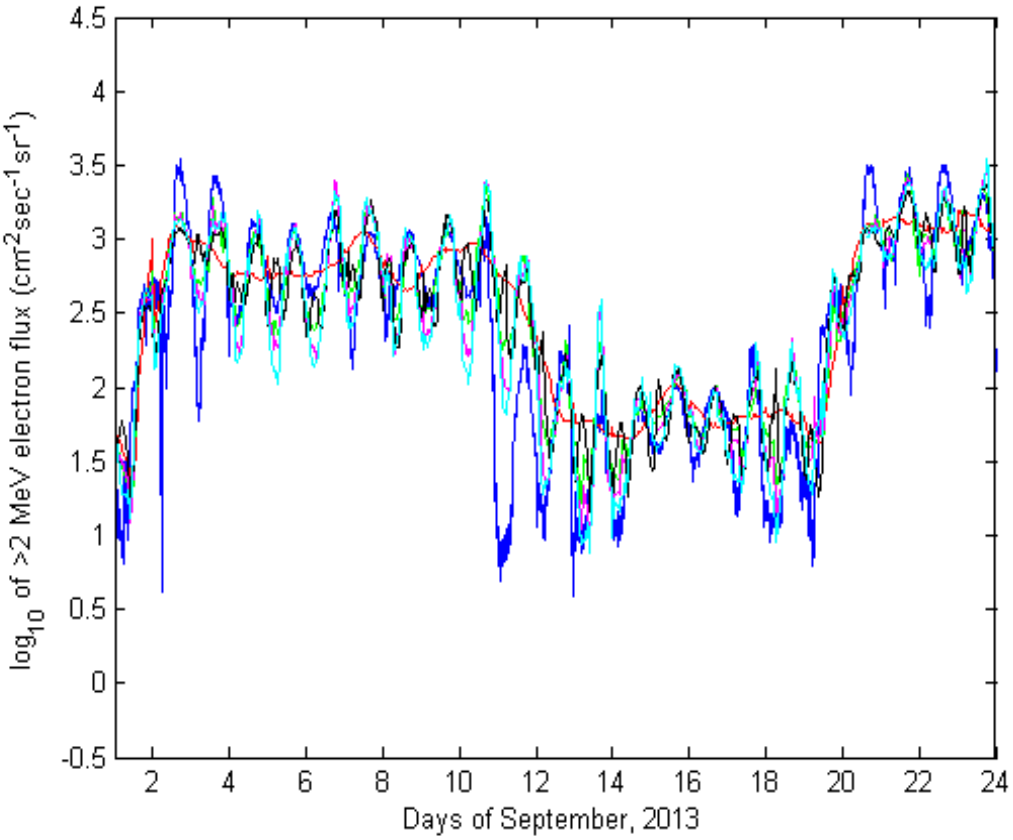

Figure 38: Flux of > 2 MeV electrons observed on GOES-13 (blue) vs. flux simulated by VNC-S using various field models, for 1-23 September, 2013, with smoothing applied. Red signifies no external field, green is Fairfield and Mead [1975], magenta - Tsyganenko [1987, short], black - Tsyganenko [1987, long], cyan - Tsyganenko [1989].

.

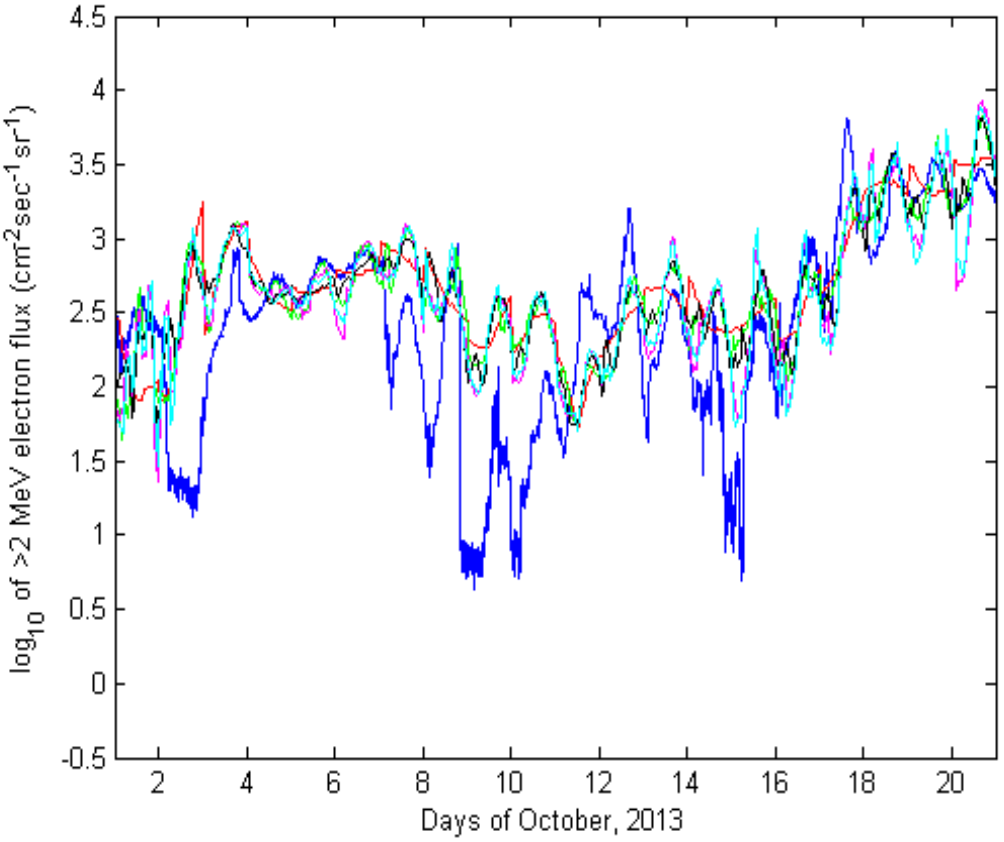

Figure 39: Flux of > 2 MeV electrons observed on GOES-13 (blue) vs. flux simulated by VNC-S using various field models, for 1-20 October, 2013, without smoothing. Red signifies no external field, green is Fairfield and Mead [1975], magenta - Tsyganenko [1987, short], black - Tsyganenko [1987, long], cyan - Tsyganenko [1989].

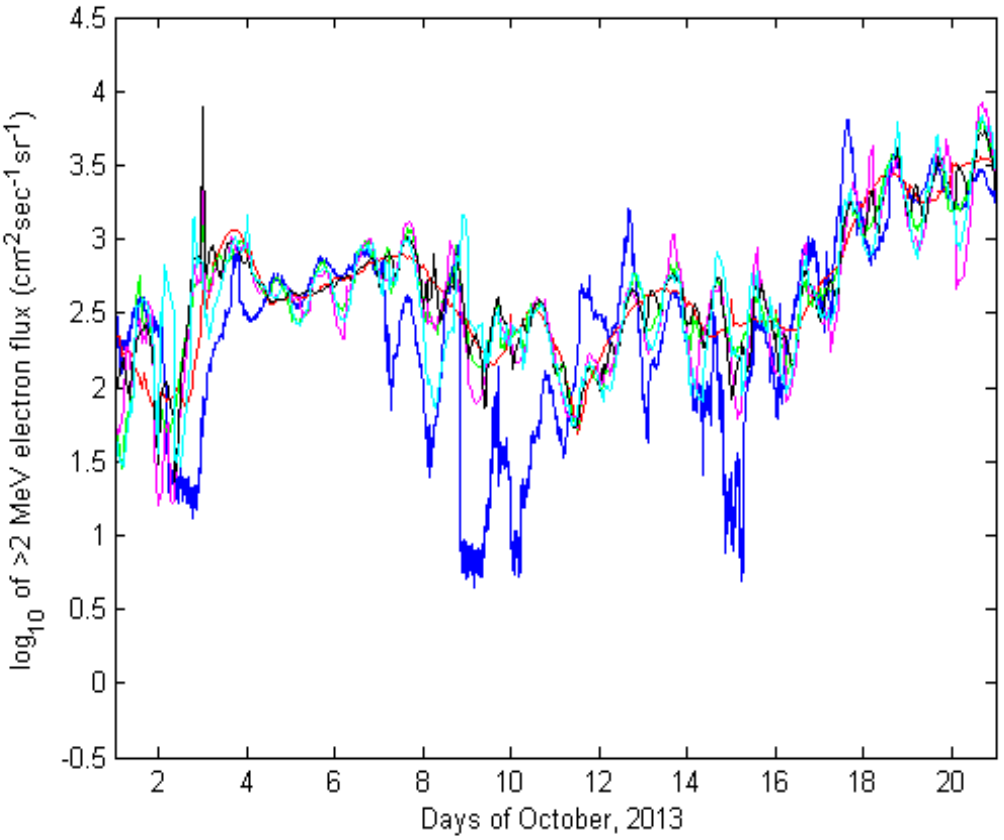

Figure 40: Flux of > 2 MeV electrons observed on GOES-13 (blue) vs. flux simulated by VNC-S using various field models, for 1-20 October, 2013, with smoothing applied. Red signifies no external field, green is Fairfield and Mead [1975], magenta - Tsyganenko [1987, short], black - Tsyganenko [1987, long], cyan - Tsyganenko [1989].

.

in line with observations (Figure 36) and ultimately improves the prediction efficiency. No such obvious differences are visible for either the September 1-23, 2013 (Figures 37 and 38) or October 1-20, 2013 (Figures 39 and 40) time periods. The origin of the single-point spike present with some magnetic field models on October 3, 2014 is unclear. Overall Table 1 clearly shows that smoothing improves performance for all time periods.

Fluxes for 800+ keV electrons are shown on Figures 41, 42 and 43 for the August, September and October time periods respectively. Table 1 also lists their prediction efficiencies. For the August and October periods, prediction efficiencies are higher than for the $>$ 2 MeV channel, but for the September time period they are lower. Looking at Figure 41 for the August period, it can be seen that dropouts like the ones on August 9-10 or August 12-13 are more pronounced for higher energy channels. Therefore, the model will deviate more at higher energies. On the other hand, enhancements like the one evidenced on August 5-6 occur sooner for low energies than for high energies. The model, as can be seen on Figure 41 vs. Figure 36 for that time period, is less able to keep up with the rapid flux rise for the $>$ 800 keV channel than for the $>$ 2 MeV channel. Presumably, electrons are first accelerated to 800 keV and only then, some time later, to 2 MeV. The disparity in these two populations may be picked out by NARMAX, but due to the relatively low time resolution of NARMAX, it will not improve the rise time of the model significantly. Enhancements occur on the scale of hours. Therefore, if a time period has many enhancements, deviation between the model and results is likely to rise for lower energies.

The modelling of the September 1-23 time periods, on Figures 38 ($>$ 2 MeV) and 42 ($>$ 800 keV) revels another dynamic. As well as the aforementioned lag in modelling $>$ 800 keV enhancements (evident on September 1-2), the diurnal differences for the lower energy channel fluxes are exaggerated by the model. This is evident on September 4-10. Diurnal flux variations for $>$ 800 keV are less than for $>$ 2 MeV electrons. This could be due to preferential scattering of $>$ 2 MeV electrons into the loss cone by EMIC waves in the dusk sector. As will be explored in the next section of the thesis, EMIC waves do not appear to affect $<$ 1 MeV electrons under normal conditions. However, EMIC waves were not included in the VNC model, so they had no effect on the flux profile outwards of the outer radiation belt. Diurnal changes in B change the energy of the particles on that field line via the first invariant. Electrons of a fixed energy drifting towards magnetic midnight will move radially inwards, conserving their first invariant. A satellite orbiting towards magnetic midnight at a fixed radial distance will cut through weaker and weaker field lines, and will see lower and lower electron energies. Since the GOES-13 channels have a lower-energy cutoff, the total electron counts drop on the magnetic nightside. It is possible that, since $>$ 800 keV electron flux counts include a larger proportion of the electron population (including the $>$ 2 MeV electrons), there is less diurnal variation as a percentage of the total integral flux. Since the $>$ 2 MeV channel only involves a small part of the distribution, a change in B would register greater variation in flux. This effect lowers the prediction efficiency of the model for the $>$ 800 keV electron channel relative to the $>$ 2 MeV channel, and is pronounced during

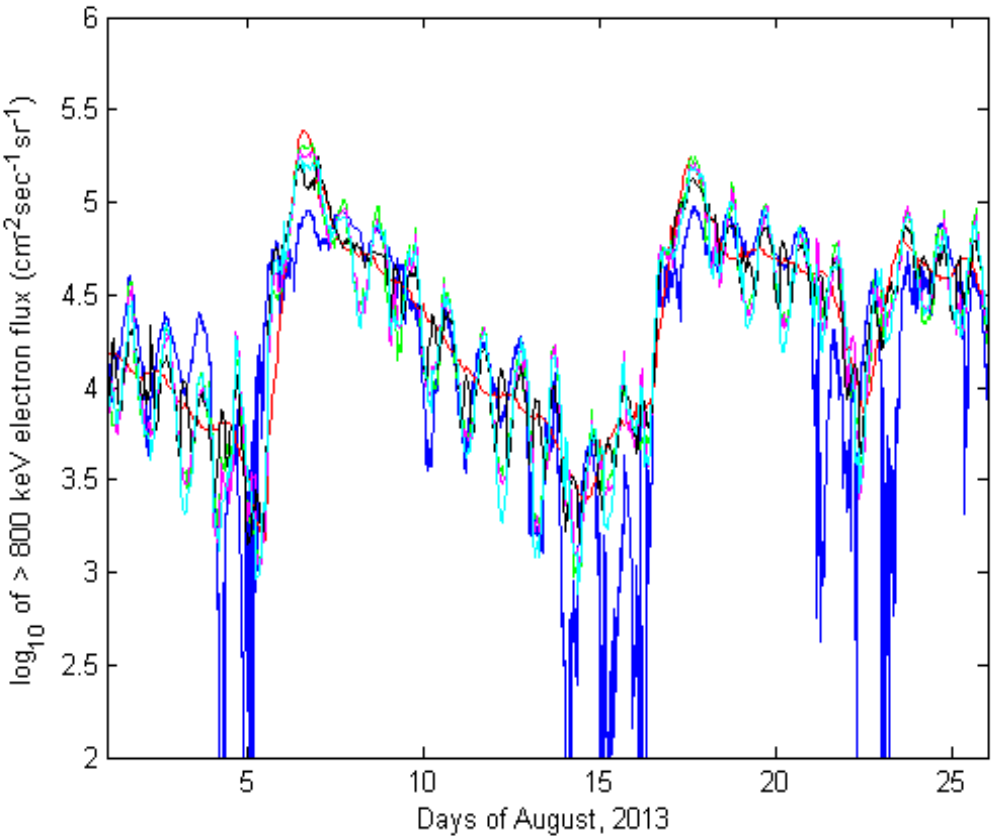

Figure 41: Flux of > 800 keV electrons observed on GOES-13 (blue) vs. flux simulated by VNC-S using various field models, for 1-25 August, 2013, with smoothing applied. Red signifies no external field, green is Fairfield and Mead [1975], magenta - Tsyganenko [1987, short], black - Tsyganenko [1987, long], cyan - Tsyganenko [1989].

.

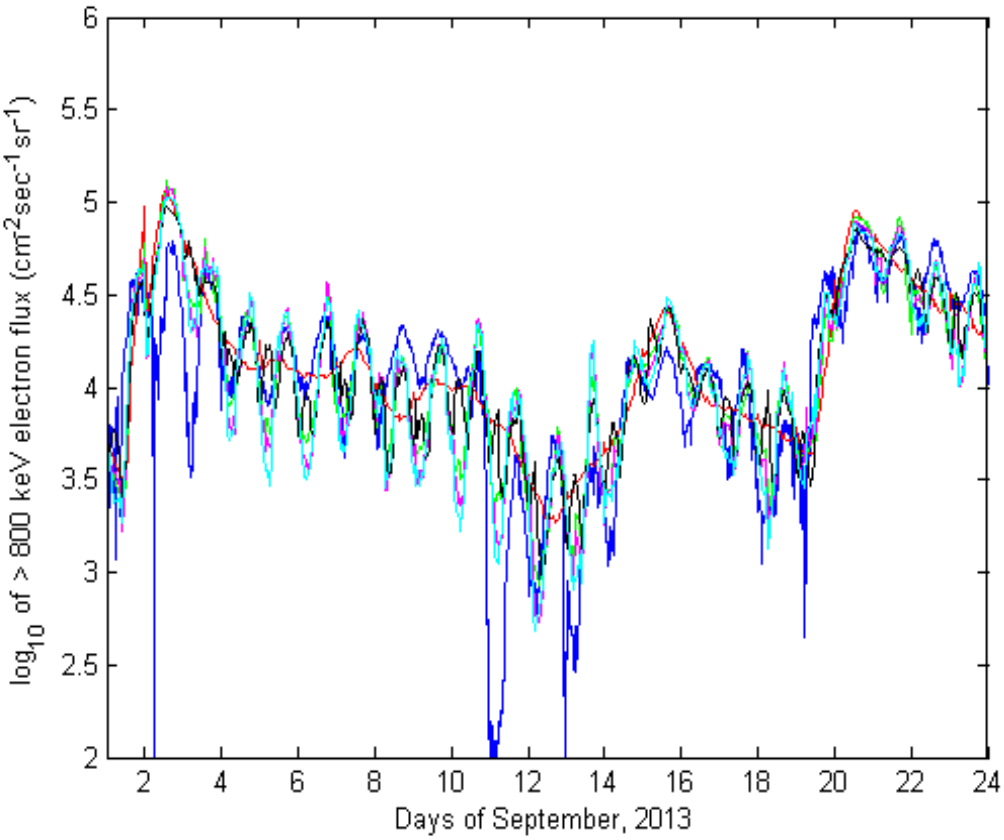

Figure 42: Flux of > 800 keV electrons observed on GOES-13 (blue) vs. flux simulated by VNC-S using various field models, for 1-23 September, 2013, with smoothing applied. Red signifies no external field, green is Fairfield and Mead [1975], magenta - Tsyganenko [1987, short], black - Tsyganenko [1987, long], cyan - Tsyganenko [1989].

.

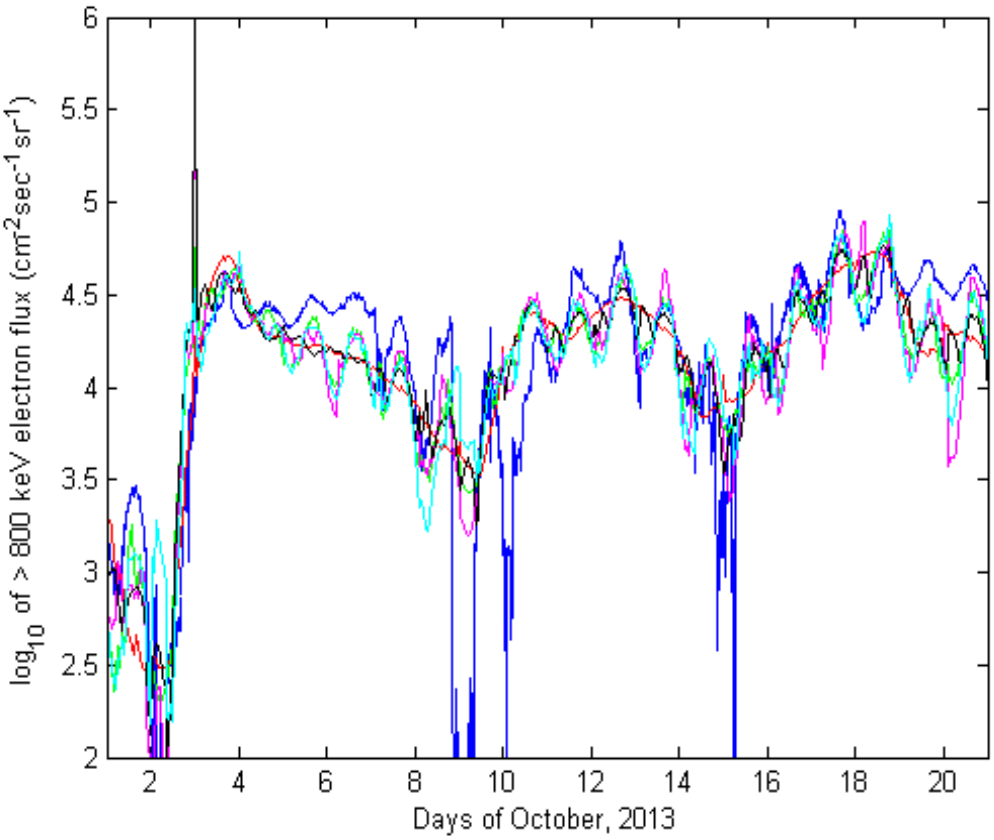

Figure 43: Flux of > 800 keV electrons observed on GOES-13 (blue) vs. flux simulated by VNC-S using various field models, for 1-20 October, 2013, with smoothing applied. Red signifies no external field, green is Fairfield and Mead [1975], magenta - Tsyganenko [1987, short], black - Tsyganenko [1987, long], cyan - Tsyganenko [1989].

.

relatively quiet periods, such as September, when the magnetic field becomes more dipolar and diurnal variations are exaggerated.

Finally, the October 1-20 time period again shows an increased prediction efficiency for $>$ 800 keV electrons relative to the $>$ 2 MeV electrons (Figures 43 and 40 respectively). The October 2013 period features significant dropouts in both energy channels, but the model captures the October 1-2 dropout much more effectively for $>$ 800 keV electrons, albeit lagging with the enhancement that occurs afterwards. In fact, the model response for the two energy channels is markedly different, which suggests that the NARMAX output for the two energy channels was different. NARMAX seems more capable at lower energies during this period of quite active space weather. Some dropouts (e.g. on October 6-8) appear to be completely missed by the model at $>$ 2 MeV but are captured reasonably well at $>$ 800 keV. This suggests that the dropouts are caused by some energy-dependent processes other than magnetopause shadowing. A separate study to investigate possible EMIC activity in this time period would shed light on the matter. While magnetopause shadowing can be linked to solar wind drivers [e.g. Shue et al., 1997], EMIC wave generation is a more complex process and will likely produce more variation if linked to solar wind parameters. NARMAX in its current form does not explicitly predict EMIC waves, but simulates $>$ 2 MeV electron dynamics based on past data from the $>$ 2 MeV channel (which cannot predict it by definition), the $>$ 800 keV channel (which has no bearing on EMIC activity) and solar wind drivers (whose link to EMIC activity is not straightforward).

Figures for the August, September and October periods without smoothing for $>$ 800 keV are displayed on Figures 44, 45 and 46 respectively. The associated prediction efficiencies are also listed in Table 1. As with the higher energy channel, prediction efficiency is lower without smoothing and sharp jumps appear in the GSO flux data as can be seen, for example, on August 6-7 in Figure 44.

4.3 Direct comparison between VNC and VNC-S

Figure 47 shows GSO fluxes for the same 1-25 August 2013 time period as analysed in the previous sections, with both VNC and VNC-S overlaid in red and green respectively. The prediction efficiencies are 0.2579 and 0.4894 for VNC and VNC-S respectively. It can be seen from the figure that VNC-S reacts to sudden enhancement events much faster than VNC, as is evident on days 5-8. The second enhancement event on days 15-18 is captured by both systems apparently simultaneously, and both system appear to be roughly equal in terms of simulating dropouts. The same data for September 1-23, 2013 is shown on Figure 48. Here, the relative prediction efficiencies are 0.3598 and 0.6522. Since the time period is quieter, VNC appears on the figure to perform adequately, albeit with some quite significant overshoots (e.g. on days 13-14). VNC-S nevertheless follows the observations more closely than VNC. Finally, for October 1-20 the data is plotted on Figure 49, with prediction efficiencies equal to 0.0019 and 0.4613. Here, VNC-S clearly performs far better, both at

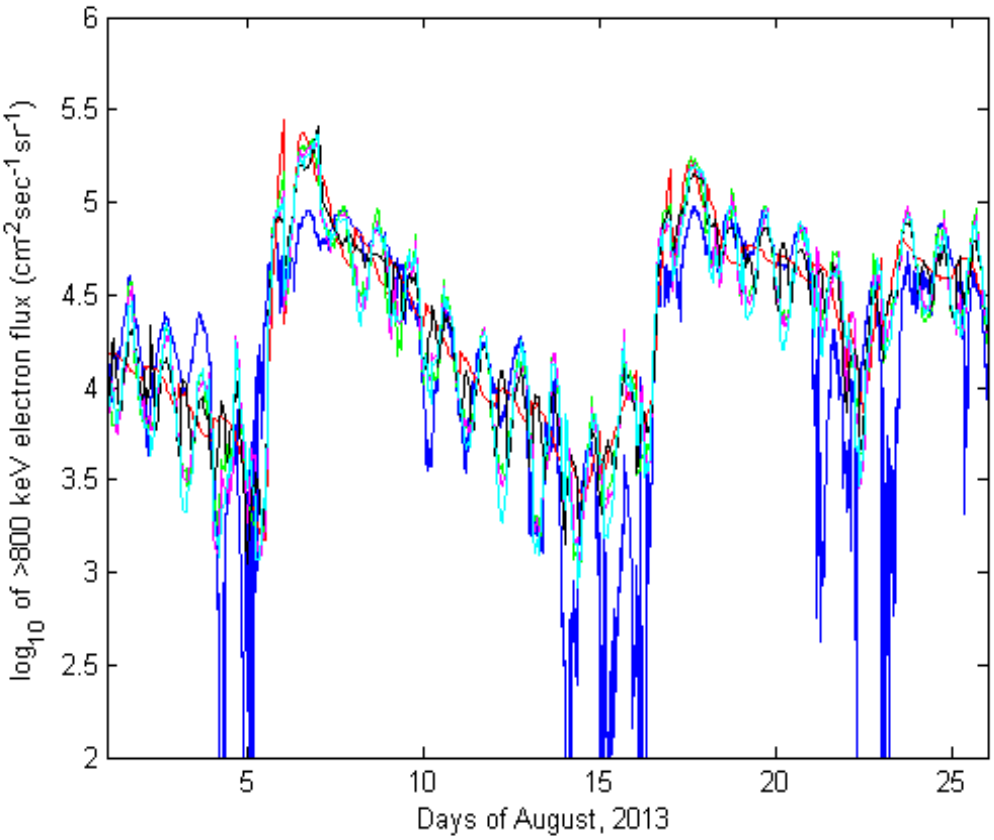

Figure 44: Flux of > 800 keV electrons observed on GOES-13 (blue) vs. flux simulated by VNC-S using various field models, for 1-25 August, 2013, without smoothing. Red signifies no external field, green is Fairfield and Mead [1975], magenta - Tsyganenko [1987, short], black - Tsyganenko [1987, long], cyan - Tsyganenko [1989].

.

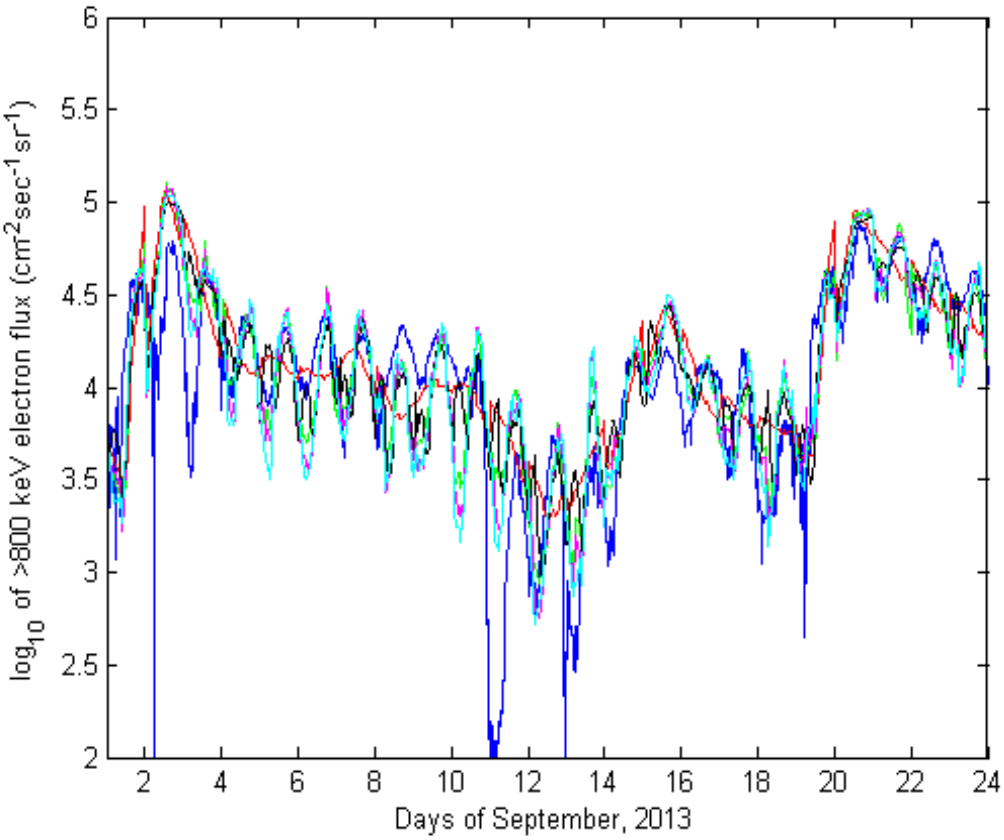

Figure 45: Flux of > 800 keV electrons observed on GOES-13 (blue) vs. flux simulated by VNC-S using various field models, for 1-23 September, 2013, without smoothing. Red signifies no external field, green is Fairfield and Mead [1975], magenta - Tsyganenko [1987, short], black - Tsyganenko [1987, long], cyan - Tsyganenko [1989].

.

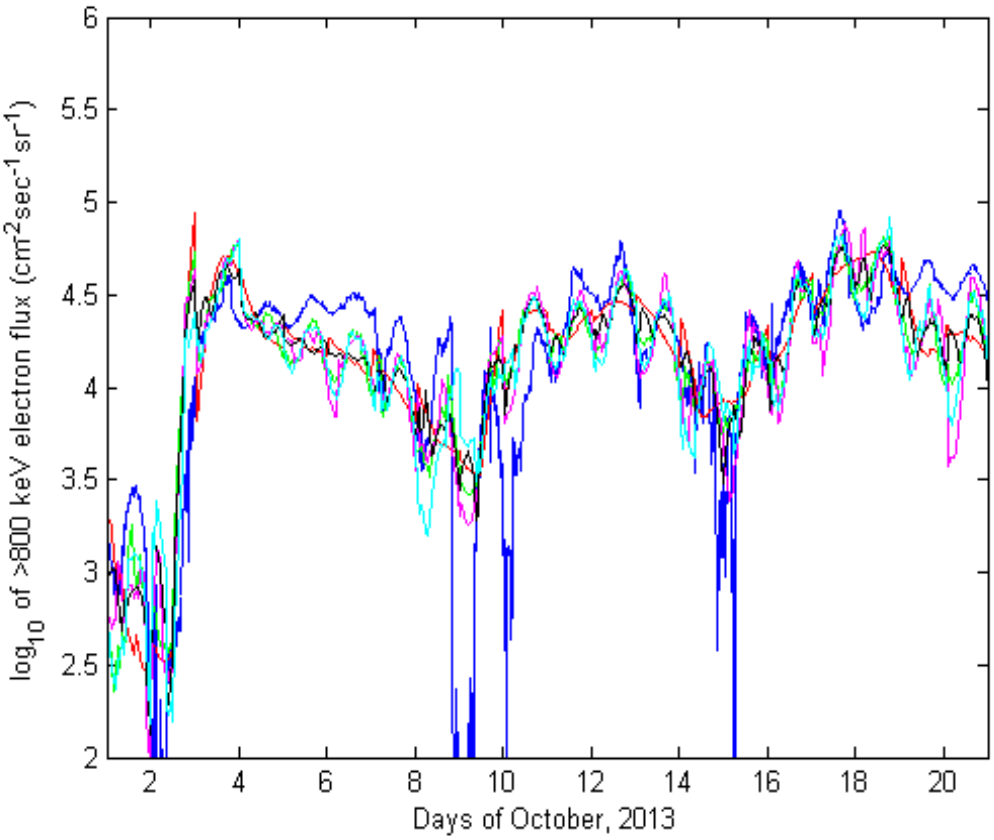

Figure 46: Flux of > 800 keV electrons observed on GOES-13 (blue) vs. flux simulated by VNC-S using various field models, for 1-20 October, 2013, without smoothing. Red signifies no external field, green is Fairfield and Mead [1975], magenta - Tsyganenko [1987, short], black - Tsyganenko [1987, long], cyan - Tsyganenko [1989].

.

simulating the initial dropout on days 1-2 and at capturing the first enhancement on days 2-4.

The observations for the three time periods study unambigously demonstrate that, as far as GSO flux prediction, VNC-S is significantly better than VNC. The two systems, although of similar design, exhibit very different behaviour. The scaling algorithm on VNC-S fundamentally redefines the prediction system, biasing it much more towards being a data-driven methodology. The VNC-derived flux profile is manipulated in such a way that its only purpose is to provide a measure of the slope in flux strength between around L^*=5-7. It no longer holds physically meaningful information about fluxes outside the region near geostationary orbit. On the other hand, accuracy at GSO improves significantly; it can be argued that VNC-S is a higher-resolution version of NARMAX that correctly captures diurnal variations but loses some of its accuracy in the process. As such it is not a completely data-driven system - some physical assumptions are inherent in the gradient between L^*=5 and L^*=7 - and its inaccuracy stems from that part of the design.

Another important feature of VNC-S is that, as shown earlier, it can predict high-energy fluxes $>$ 2 MeV. This is something VNC in its current form cannot do, as was explored previously. This is once again only possible because it almost completely relies on NARMAX data, without simulating any physical processes apart from the steady decrease in fluxes with increasing radial distance. As such it is somewhat reminiscent of the early data-driven model of Li et al. [2001], which only simulated radial diffusion and used data analysis to derive parameters for the driving function.

4.4 Long-term simulations of VNC-S

The same time period of one full year (2013) as was modelled by VNC has been modelled by VNC-S. Figures 50 to 53 show the $>$ 800 keV flux and its VNC-S simulations for the four quarters of 2013.

Apart from the over-estimation on days 1-15, the three months of simulation broadly followed the variations observed by GOES-13. Several periods of flux dropouts and enhancements can be distinguished; the biggest flux increase occured around days 60-63, where flux increased from a dropout (negligible levels) to over 10,000 particles per second. This flux increase was accurately modelled. The steady flux drop in the days following the increase was also tracked by the model, although it over-estimated diurnal flux variations. In the second quarter, the picture was similar, although the model over-estimated flux by several days as a dropout on the days 104-105 was missed by the system. Another rapid flux increase around day 115 was successfully modelled. Days around 140-150 (the latter parts of May 2013) feature a data gap. A dropout immediately following that data gap was missed by NARMAX, although the system did register a flux decrease on the next day. In the third quarter, VNC-S tracked the rapid changes in flux relatively well, albeit again over-estimating the extent of the diurnal variation, which resulted in an under-estimation of fluxes at nighttime. Flux increases such as on days 228-229 and 261-263 were simulated successfully.

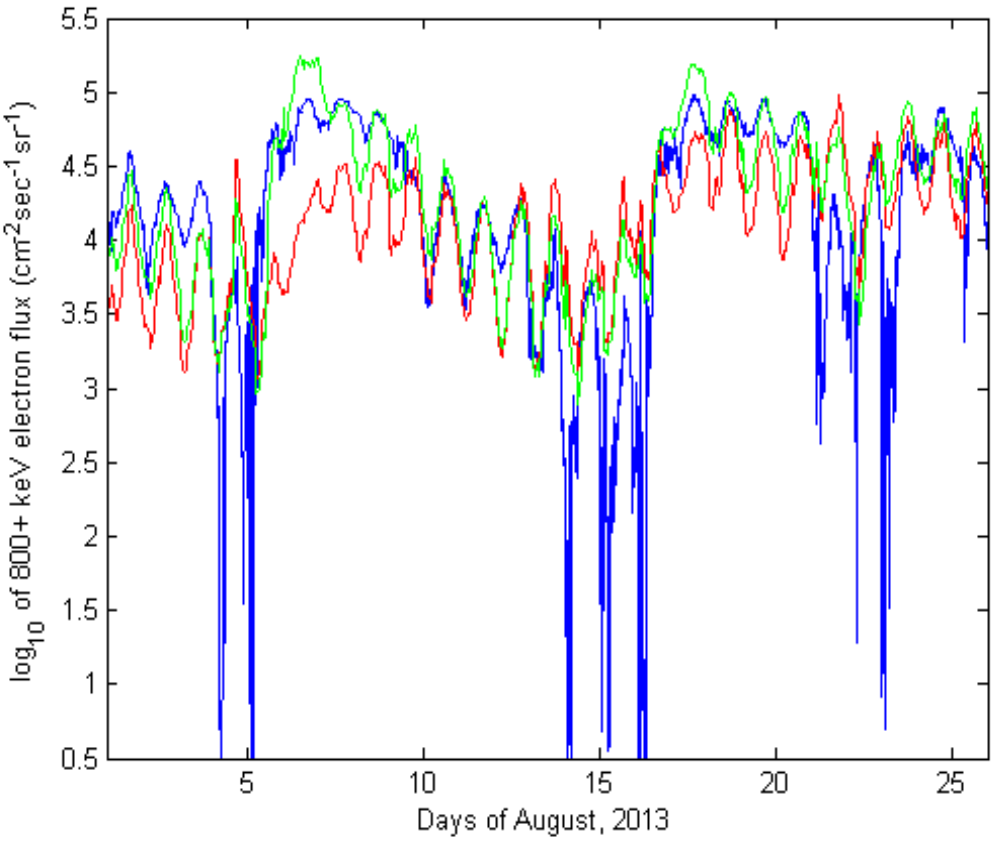

Figure 47: Flux of > 800 keV electrons observed on GOES-13 (blue), flux modelled by VNC (red) and VNC-S (green), for August 1-25, 2013.
.

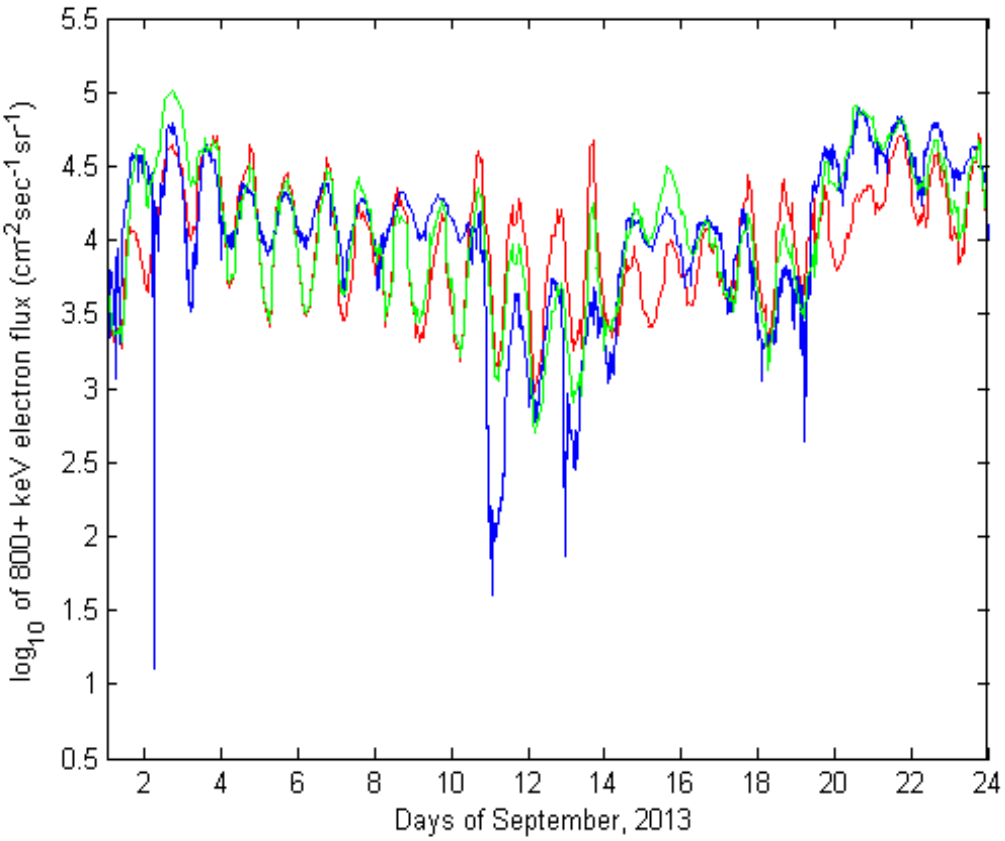

Figure 48: Flux of > 800 keV electrons observed on GOES-13 (blue), flux modelled by VNC (red) and VNC-S (green), for September 1-23, 2013.
.

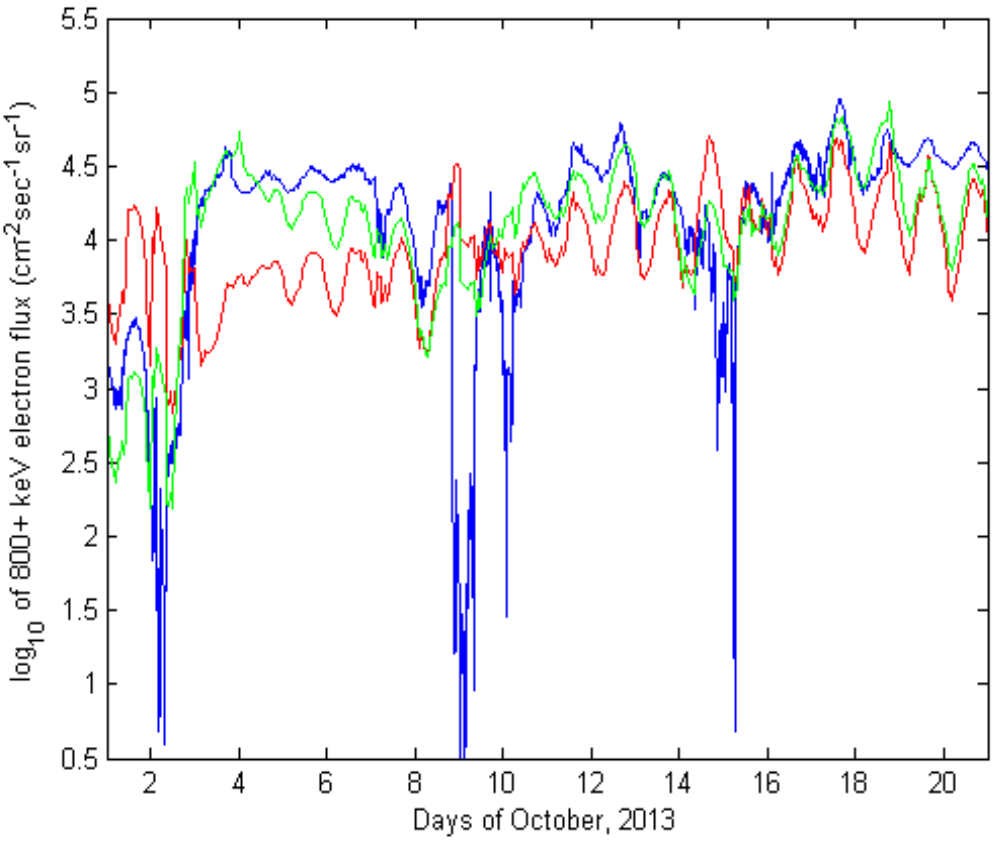

Figure 49: Flux of > 800 keV electrons observed on GOES-13 (blue), flux modelled by VNC (red) and VNC-S (green), for October 1-20, 2013.
.

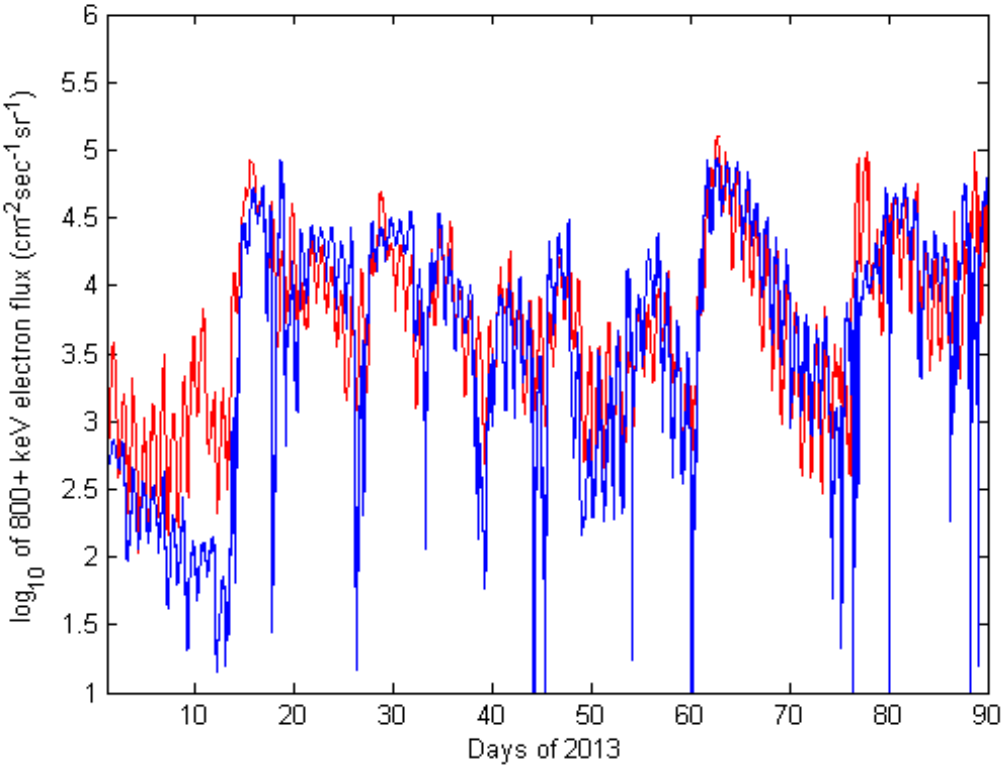

Figure 50: Flux of > 800 keV electrons observed on GOES-13 (blue), flux modelled by VNC-S (red) for the first quarter of 2013.

.

The last quarter included many of the time periods that were analysed in more detail elsewhere; apart from the flux over-estimation around day 315 and the usual under-estimation of fluxes at night-time, the behaviour of the model was the same as before that.

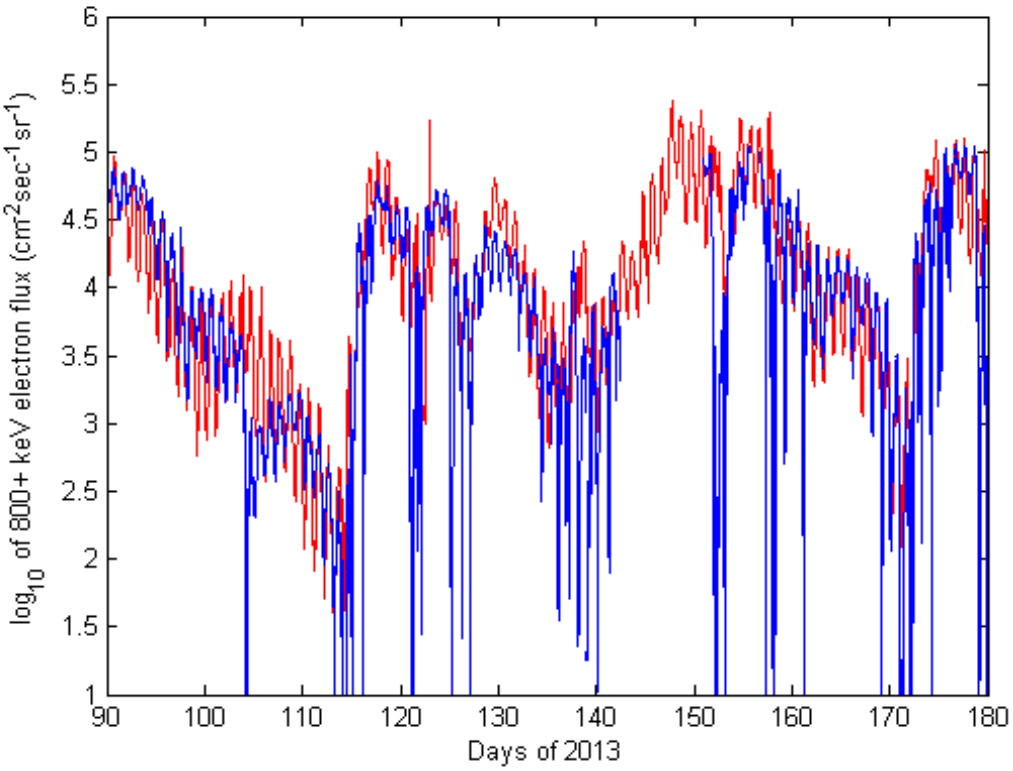

Figure 51: Flux of > 800 keV electrons observed on GOES-13 (blue), flux modelled by VNC-S (red) for the second quarter of 2013.

.

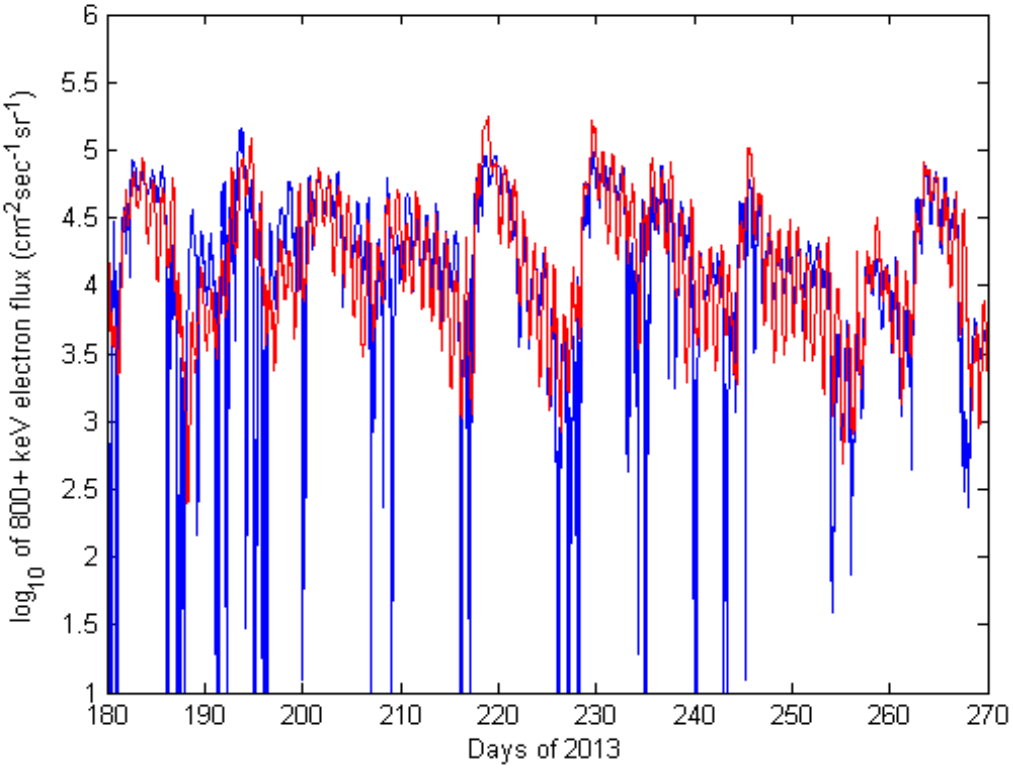

Figure 52: Flux of > 800 keV electrons observed on GOES-13 (blue), flux modelled by VNC-S (red) for the third quarter of 2013.

.

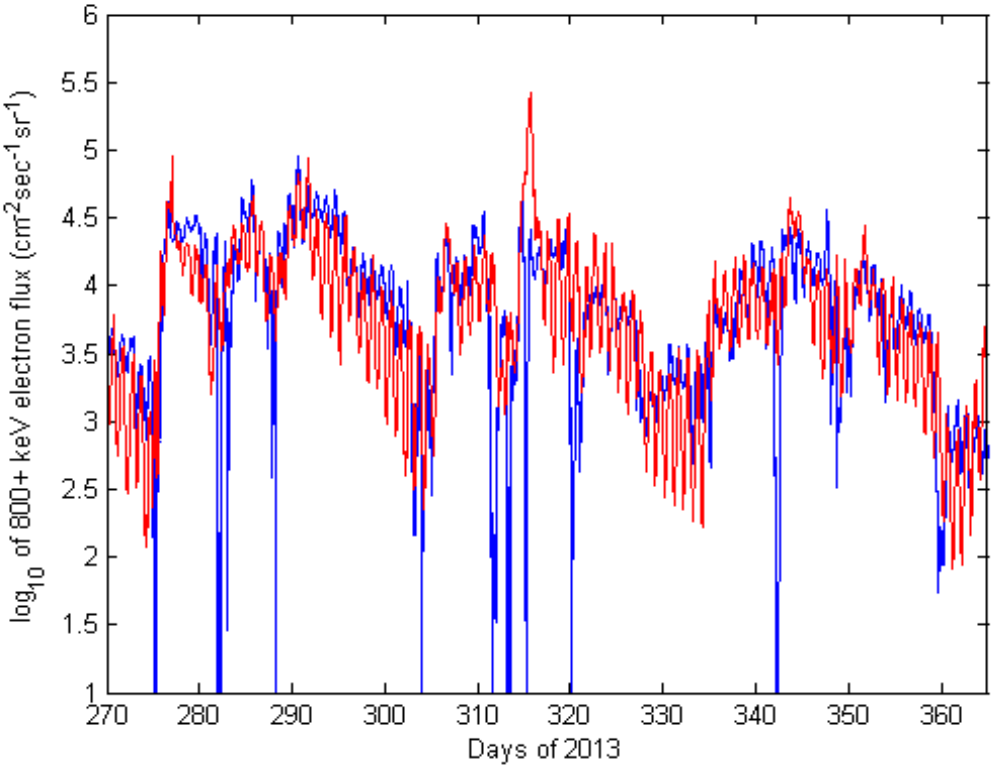

Figure 53: Flux of > 800 keV electrons observed on GOES-13 (blue), flux modelled by VNC-S (red) for the fourth quarter of 2013.

.

Figures 54 to 57 show the > 2 MeV electron flux and its VNC-S simulation for the four quarters of 2013. For the high-energy channel, new dynamics are identified. Low fluxes (around unity on the y-axis) tend to exhibit very small diurnal variations, and the model significantly over-estimates diurnal variations in this case. It is recommended that a different magnetic field model be used under circumstances where such fluxes are likely (they tend to correspond to geomagnetically quiet periods). The large enhancement around days 60-63 is successfully simulated. In the second quarter the picture is similar, with VNC-S tracking changes caused by varying NARMAX values. A large dropout on days 152-155 is modelled by the system, albeit with a delay and a smaller variation. The performance is somewhat better in the third quarter, which features neither large-scale dropouts (though plenty of small-scale depletion events) nor extended periods of low fluxes. Once again, over-estimation of diurnal variations is evident. Finally in the fourth quarter, performance degrades again as extended

quiet periods increase the error between the model and the observations.

The overall prediction efficiency was 0.4319 for the $>$ 800 keV channel and 0.5740 for the $>$ 2 MeV channel.This is lower than for individual time periods analysed earlier. The reason for this is that there are many periods in the full-year simulation where the model performance is less effective. The time period in May-June 2013 includes some of the strongest fluxes observed that year, with $>$ 2 MeV electron fluxes reaching tens of thousands. Normally the fluxes of electrons for that energy channel are around a hundred. With these large increases followed by sudden depletions, the variations between the model and the observations become significant. Secondly, as was evidenced for $>$ 2 MeV electrons, there are extended quiet periods where fluxes exhibit very little diurnal variation. The model then over-estimates the variations. While this is not strictly a problem from the view of satellite protection (extended periods of low fluxes of relativistic electrons present little danger to satellites), it should be addressed in the future. It is proposed to use a dipolar magnetic field for those geomagnetic conditions. Finally, for both the $>$ 800 keV and $>$ 2 MeV electrons, the model exaggerates the diurnal differences even in periods of normal flux, leading to an under-estimation of fluxes at magnetic nighttime. This is again not necessarily critical for satellite protection (it is the local maxima at daytime that are important, not the nighttime minima). These inaccuracies may be due to the magnetic field model used, but as several magnetic field models were tested and the T89 was found to perform best overall, the problem may well lie elsewhere. Since the VNC-S design 'arbitrarily' scales the flux profile without explicit physical reasons to do so, the gradient between L^*= 6 and L^*=7 may end up inaccurate, leading to erroneous output. Further research is needed to understand how the gradient behaves under different conditions. The problems inherent in VNC (for example, using averaged high-energy fluxes for the outer boundary instead of high-resolution low energy fluxes) may well account for this inaccuracy in VNC-S.

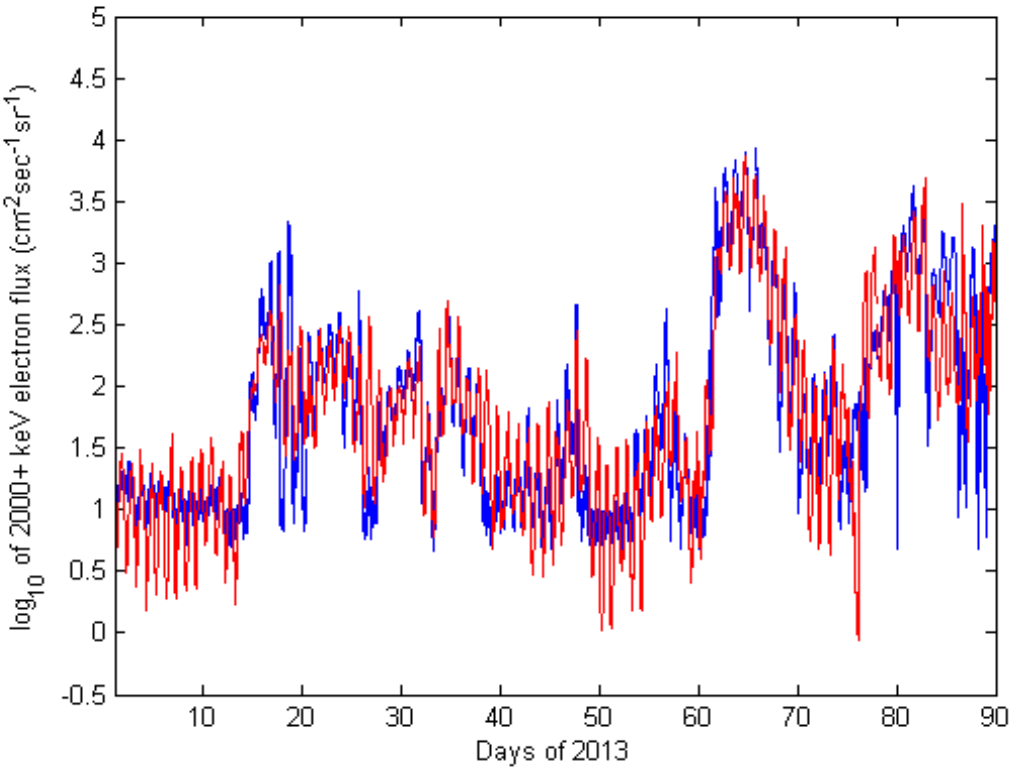

Figure 54: Flux of $>$ 2000 keV electrons observed on GOES-13 (blue), flux modelled by VNC-S (red) for the first quarter of 2013.

.

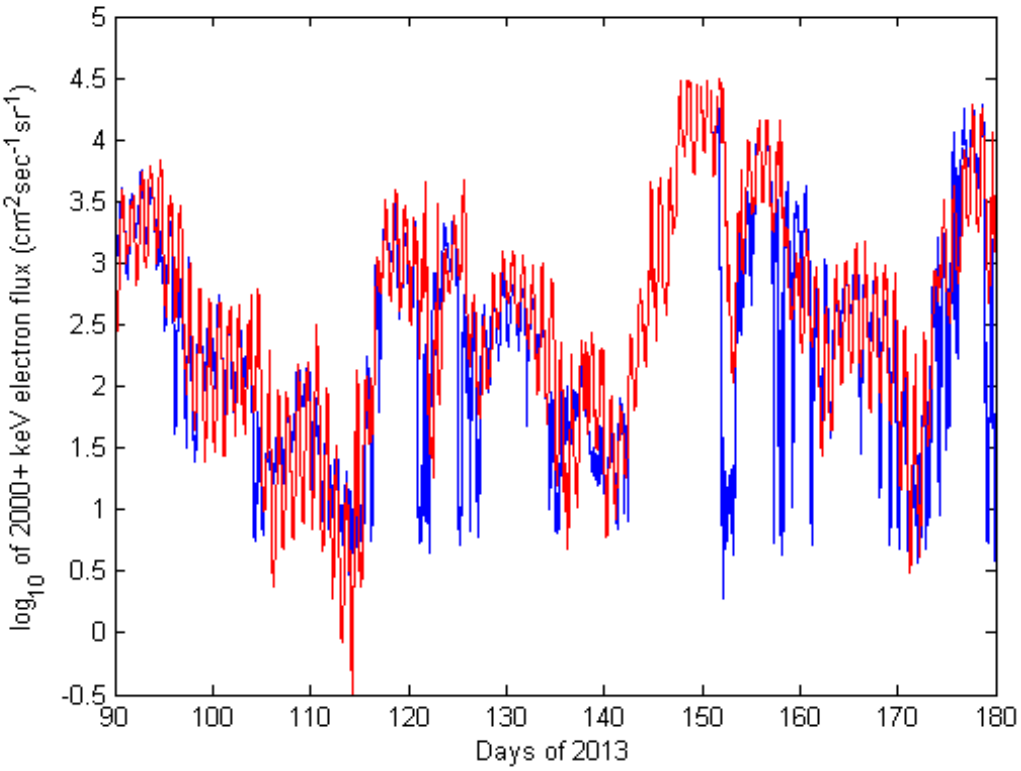

Figure 55: Flux of $>$ 2000 keV electrons observed on GOES-13 (blue), flux modelled by VNC-S (red) for the second quarter of 2013.

.

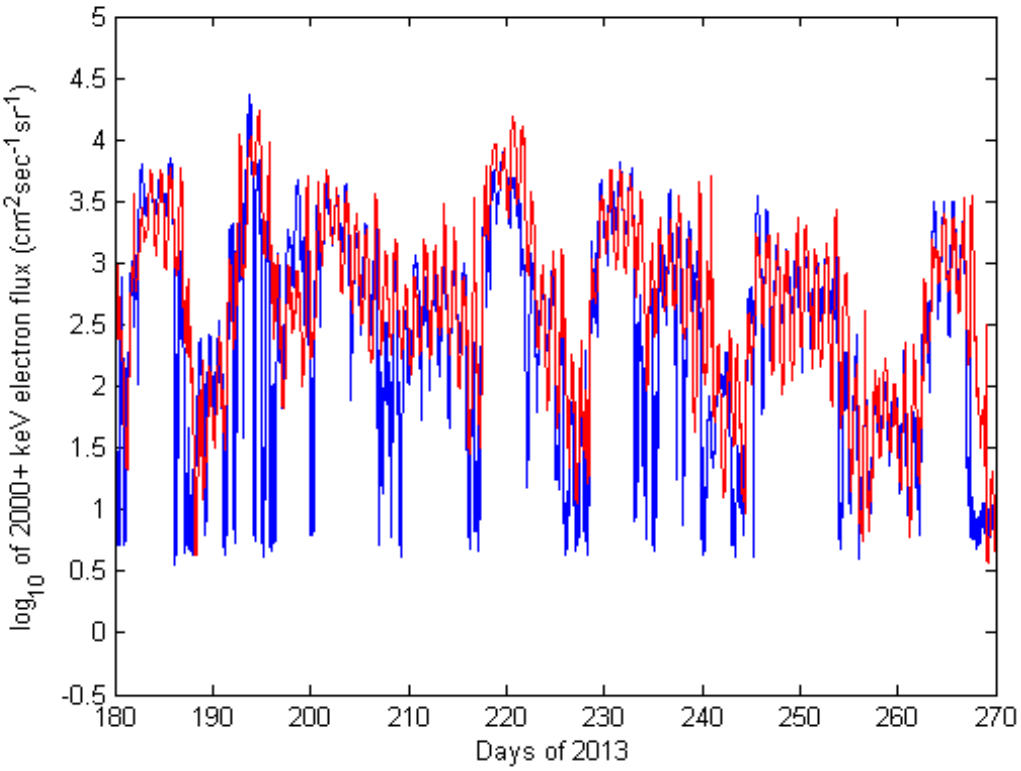

Figure 56: Flux of > 2000 keV electrons observed on GOES-13 (blue), flux modelled by VNC-S (red) for the third quarter of 2013.

.

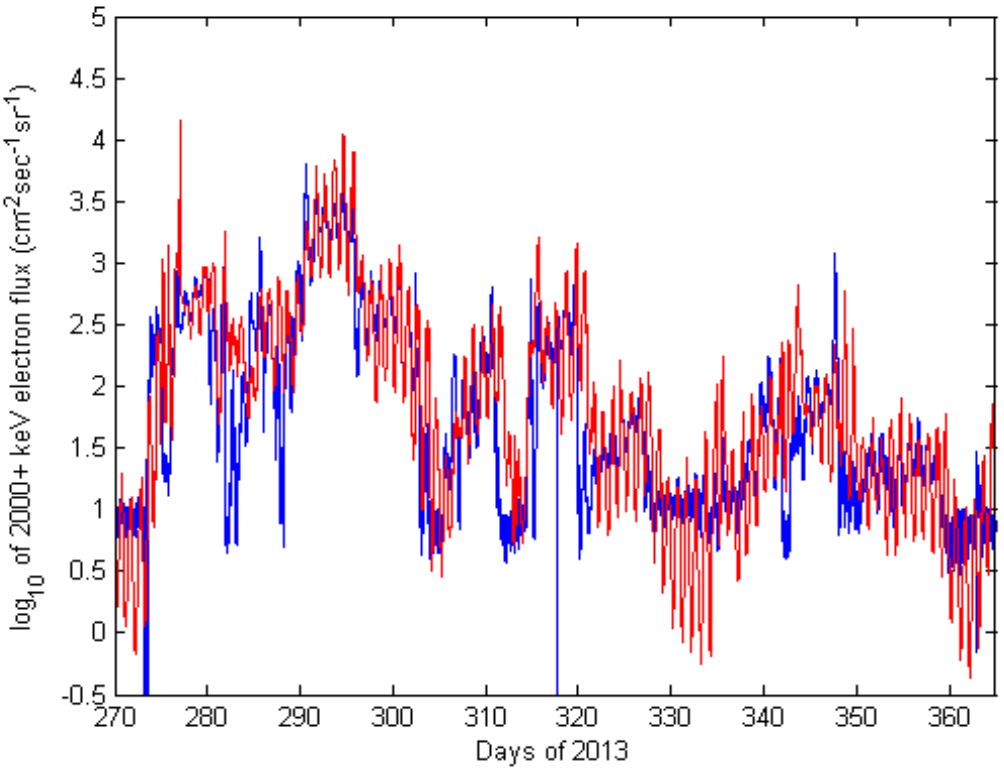

Figure 57: Flux of > 2000 keV electrons observed on GOES-13 (blue), flux modelled by VNC-S (red) for the fourth quarter of 2013.

.

4.5 Summary

A modification of VNC was explored where the flux profile was scaled by weighted averages of NARMAX values for the relevant days. The modification was dubbed VNC-S or Scaled. The scheme was found to generate better predictions at geostationary orbit at the cost of greatly reduced accuracy inwards of geostationary orbit. It was also found to be capable of generating accurate predictions for energies > 2 MeV, for which the original VNC predictions were demonstrated to have been inaccurate.

Several magnetic field models - all driven by at most one parameter, the Kp index - were experimented with to determine which one generates the best predictions. It was found that the [Tsyganenko, 1989] and [Fairfield and Mead, 1975] models produced the best results. However, it was also found that during quiet periods, the [Tsyganenko, 1989] model over-estimated the diurnal flux variations. As such it was suggested that a more dipolar model would be more suitable for low Kp indices, to reflect the more dipolar magnetic field configuration. Nevertheless, it was found that prediction efficiency maximised during geomagnetically quieter periods as opposed to times of more active space weather.

The effect of smoothing - normalising each time period by a running average of 24 data points around it, rather than the 24 data points of the particular day in question - was investigated. Smoothing resulted in less sharp jumps as the system crossed the midnight line, and was found to improve overall prediction efficiency.

The output from VNC-S was compared directly to output from VNC. It was found that VNC-S performed better at simulating flux enhancements and generally followed the observations more closely, even in quieter periods without major enhancements.

A long-term simulation was carried out for VNC-S, analysing the same time period (all of 2013) as in Section 3.7. The prediction efficiency from VNC-S was found to be significantly higher than from VNC.

5 Chapter 5: EMIC waves in the radiation belts

5.1 Quantifying the effect of EMIC waves on radiation belt dynamics: the search for minimum resonant energy

The quantitative effect of the EMIC wave on radiation belt dynamics is currently unclear. It is known that EMIC waves are very efficient at scattering relativistic electrons with energies > 1 MeV [e.g. Shprits et al., 2008b]. What is not known is how low the minimum resonant energy is, and thus, how much of the distribution is affected. The instability has a sharp cut-off at a certain energy [e.g. Li et al., 2013] below which the wave is out of resonance and has no effect on the electron population.

Theoretical minimum resonant energies were calculated by Summers and Thorne [2003] as being regulated by the parameter $\alpha^* = \Omega_e^2/\omega_{pe}^2$ where Ω_e is the electron gyrofrequency and ω_{pe} is the electron plasma frequency. A low α^*, typically 10^{-3}, is needed to obtain minimum resonant energies down to below 1 MeV. This can occur in regions of high plasma density such as the duskside plasmasphere or the plume. Increased concentrations of heavy ions also lower minimum resonant energies, such as those found during storm times. The study used the linear cold plasma dispersion relation for the relationship between frequency and wavenumber. The lowest resonant energies would correspond to the waves with the longest wavenumbers. Gary et al. [2012] used kinetic linear dispersion theory to evaluate effects of helium temperature, plasma beta and relative helium abundance on wave growth rates and maximum unstable wave number. The study showed that in a 2-ion plasma, cold and dense He^+ would favour the excitation of short-wavelength instabilities. The study concluded that under such conditions, resonance with electrons of down to 500 keV was feasible.

One of the earlier efforts to statistically analyse the scope of the instability was work by Meredith et al. [2003] using CRRES data. Instead of performing wave vector analysis, the study calculated minimum resonant energy from the wave frequencies using the cold plasma dispersion relation. The study found a range of minimum resonant energies between 500 keV and 50 MeV, with $E_{min} <$ 2 MeV for around 11 % of observation, primarily in the post-noon sector. Low resonant energy was found for frequencies close to the gyrofrequencies. This makes sense considering the wave number maximises around the resonances for the L-mode.

Ukhorskiy et al. [2010] argued that if a spread of frequencies with a finite bandwidth is considered, wave power would be found near or at the gyrofrequency, with correspondingly low wave numbers in that $\omega - k$ section. This approach could yield potential minimum resonant energies as low as 400 keV. However, analysis of time series of many EMIC waves show constant frequencies, so it could be that the finite bandwidth is an artefact of the frequency analysis. In any case, Lee et al. [2012] reported an observation of an EMIC wave specifically at the He^+ resonance over the supposed "stop band". This is

impossible according to the cold plasma approximation (the wave mode would have a cut-off in that region) but could be explained by thermal plasma effects. In fact the minimum resonant energy is related to wave number, and only depends on frequency implicitly via the dispersion relation. Chen et al. [2013] compared cold, warm and full plasma dispersion relations and found that significant errors in E_{min} can result from using the L-mode, particularly near or at the resonances. This confirmed earlier work by Silin et al. [2011a] which showed that as plasma beta increased, the full dispersion relation will start to deviate significantly from the cold plasma approximation. The active conditions when cold plasma theory begins to break down are also exactly the times when EMIC wave activity would be expected to rise. Measuring the k-vector is thus the correct way to gain information about minimum resonant energy directly from wave observations, regardless of the geomagnetic environment.

Of particular interest are EMIC triggered emissions, first reported by Cluster observations [e.g. Pickett et al., 2010]. Their theory is described in numerous theoretical works [e.g. Omura et al., 2010, Shoji and Omura, 2011] but they are believed to be quite rare (Grison et al. [2013] only reported three cases in 8 years of Cluster data). However, Nakamura et al. [2014] reported tens of triggered events observed by THEMIS mainly on the dayside around 6-10 R_E. This suggests that Cluster orbital coverage may not be ideal for observing them.

They are triggered by an EMIC wave that modifies the velocity distribution function of energetic protons to form a hole in phase space. Once the proton hole is formed, the dispersion relation is modified and the wave frequency increases with time. The growth mechanism is similar to that of the whistler-mode chorus emissions. The outcome of the emission is a series of wave packets generated at different rising frequencies, the highest of which can significantly exceed the original EMIC wave that triggered the process. Since the higher frequencies have higher wavenumbers, it is possible that this mechanism can generate a train of EMIC sub-packets that can scatter electrons at lower energies than the 'classic' EMIC wave. Sakaguchi et al. [2013] reported an observation of a triggered EMIC emission in the slot region observed on the Akebono satellite and calculated the minimum resonant energies as 1-10 MeV. The methodology they used infers E_{min} from the wave frequency.

Their general paucity in satellite data sets may well be misleading. After generation the train of wave packets disperses as they travel with different group velocities. Away from the generation region, the chorus-like structure becomes impossible to observe. But the waves generated elsewhere can still arrive at the detector in the form of single higher-frequency wave packets (unless they are damped before reaching the observer). It is possible that a significant number of EMIC waves observed on various satellites originated as triggered emissions, and as such, they may well have a profound impact on radiation belt dynamics.

5.2 Determination of EMIC minimum resonant energy

The study by Pakhotin et al. [2013] examined a triggered EMIC emission event observed by Cluster on March 30, 2002, calculating the wave numbers and com-

paring them to the theoretical cold plasma dispersion relation. This section will summarise and extend this work as a demonstration of how the phase differencing technique can be used to calculate minimum resonant energies. Knowledge of the theoretical dispersion relation is not necessary, though it can be used as a check to make sure the numbers are in the right range.

The event was observed as the Cluster constellation crossed the plasmasphere around 0700-0900 UT on March 30, 2002, around L $\approx$ 4.4 and in the dusk MLT sector (MLT $\approx$ 2215 UT). The spacecraft crossed the magnetic equator shortly after the onset of the event. Figure 58 shows the plasmapause crossing as viewed from Cluster 1. The panels denote (a) density of energetic ions recorded by the CIS experiment [Reme et al., 2001] (b) ion velocity, (c) total magnetic field strength as measured with the fluxgate magnetometer (FGM) insturment [Balogh et al., 2001], (d) magnetic field waveform spectrum from STAFF [Cornilleau-Wehrlin et al., 2003] and (e) electric field waveform spectrum from WHISPER [Dècrèau et al., 1997]. The plasmapause crossing can be clearly identified by the rapid rise in the plasma frequency seen on WHISPER (panel (e)) between $\approx$ 0730 and 0850 UT. Energetic ions flagged by CIS (panel (a)) also register an increase inside the dense plasmapause between $\approx$ 0830 and 0900 UT. The EMIC waves can be seen on STAFF (panel (d)) between $\approx$ 0750 and 0830 UT as emissions around 1-3 Hz. The long line of enhanced signal power at 0.5 Hz that persists throughout the panel appears to be satellite spin.

The event was observed on the Cluster Fluxgate Magnetometer (FGM) instrument [Balogh et al., 2001] with the result displayed on Figure 59. The white lines denote ion gyrofrequencies (from top to bottom: H^+, He^+ and O^+ respectively). The B_y component of the magnetic field was used since the waves are transverse and were observed to propagate near-parallel to the local magnetic field. A characteristic stop band can be seen around 12-19 minutes into the event around 1 Hz where signal power is far lower. The cold plasma theory predicts the existence of such a cut-off where no waves propagate.

The fact that some wave power is evident inside the stop band can be an artefact of the spectral analysis. This also applies to the point raised by [Ukhorskiy et al., 2010] earlier. To demonstrate the problem, consider Figure 60. The figure shows an artificially created wave packet of 1 Hz frequency sampled at 22 Hz (the standard Cluster FGM sampling frequency). From the figure shows (a) the time series and (b)-(d) the Fourier transform of the signal with a sliding Hanning window and the signal split up into 5, 10 and 20 intervals respectively. It can be seen that as the number of intervals increases, the temporal resolution improves while the resolution in the frequency domain degrades. Splitting the time series into segments and carrying out a fast fourier transform over each segment reveals the temporal dynamic of the signal frequency, but each FFT operation has less data points to work with so frequency ambiguity increases. It can be seen that the Fourier transform has a visible 'bandwidth' that increases as the frequency resolution decreases, while the original signal has no bandwidth at all by definition (being an artificial 1 Hz signal that could be described by a delta function). In this way, the wave power at the gyrofrequency seen on the Fourier transforms of the CRRES data could well be an artefact just like the

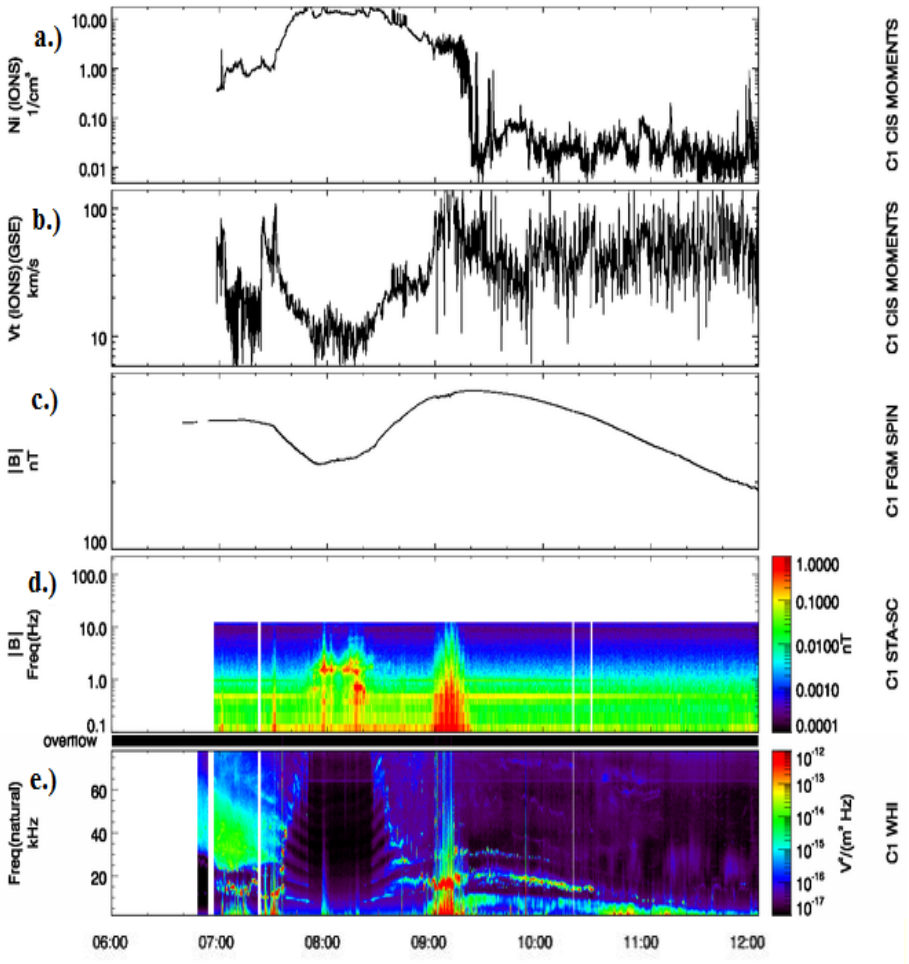

Figure 58: From top to bottom, (a) energetic ion density recorded by CIS, (b) ion velocity recorded by CIS, (c) total magnetic field strength from FGM, (d) magnetic field waveform from STAFF and (e) electric field waveform from WHISPER. Data was provided by the Cluster Active Archive.

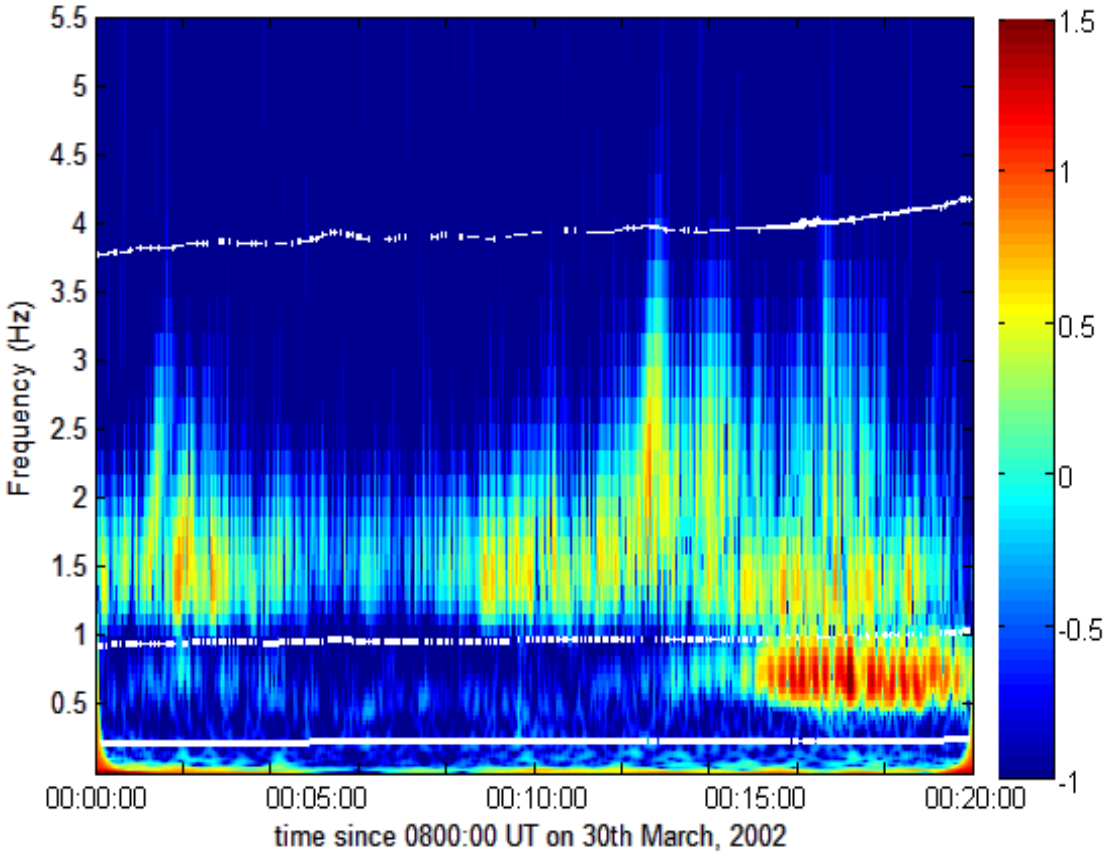

Figure 59: power spectral density of the B_y component of the magnetic field observed using the Cluster 1 Fluxgate Magnetometer. White lines denote local ion gyrofrequencies.

'bandwidth' seen in the test signal on Figure 60. This demonstrates the need to calculate the wave vector in order to unambiguously determine minimum energy, rather than relying on the dispersion relation to infer it from the wave frequency.

5.3 k-vector determination

The phase differencing method of determining wave vector direction [e.g. Balikhin et al., 1997] can be used if a signal is seen on two spacecraft simultaneously such that it is possible to unambiguously determine they are the same signal. Then, knowing the separation vector between the two spacecraft, the phase difference at an observed frequency ω_1 between the two wave signals corresponds to

$$\Delta\psi(\omega_1) = (\vec{k}(\omega_1)\vec{R}) = |k(\omega_1)||R|cos(\theta_{kR}) \tag{30}$$

Thus the projection of the wave vector $\vec{k}$ on the inter-satellite separation vector $\vec{R}$ can be calculated from the phase difference. To recover the full wave vector from its projection, which is a scalar, knowledge of the wave vector direction is needed. This can be obtained using the minimum variance technique [Sonnerup and Cahill, 1967] if the waves are elliptically polarised. Then, $\vec{k} = (\Delta\psi/|\vec{R}|)/\theta_{kR}$. Minimum variance uses the Maxwell equation $\nabla \cdot \mathbf{B} = 0$. Then, for a transverse plane wave, if the coordinate system is rotated such that the x-axis is aligned with the propagation direction, magnetic field fluctuations will tend to zero along that axis. Thus the direction of minimum variance in the magnetic fields can be assumed to be the line along which the wave propagates. Which way the wave propagates can be determined using multiple satellites (if one satellite sees the wave appear before the second one) or using other techniques such as Poynting vector analysis.

An example of minimum variance analysis is shown on Figure 61 in what is known as a hodogram. This is a view of the FGM time series projected along the axes of maximum, intermediate and minimum variance, as determined by zero-meaning each axis in the time series and then analysing the variance of this time series. The new projection clearly shows the circular polarisation of the wave packet segment. Considering that the aforementioned multi-satellite analysis determines that the EMIC wave is coming out of the page in this case, it can be seen to be left-hand circularly polarised, as expected for the L-mode.

Figure 62 shows an example of a time period where wave packets are visually identified from the shape of their envelope as being the same wave packet propagating from one satellite to the other. A total of about 30 such wave packets have been identified in the time series, some of which were later discarded from the analysis due to other issues such as unclear wave vector direction. For the remaining ones, phase differencing analysis has been performed. The results, as well as the corresponding cold plasma dispersion relation, are shown on Figure 63. Density values to calculate the L-mode dispersion relation are the same

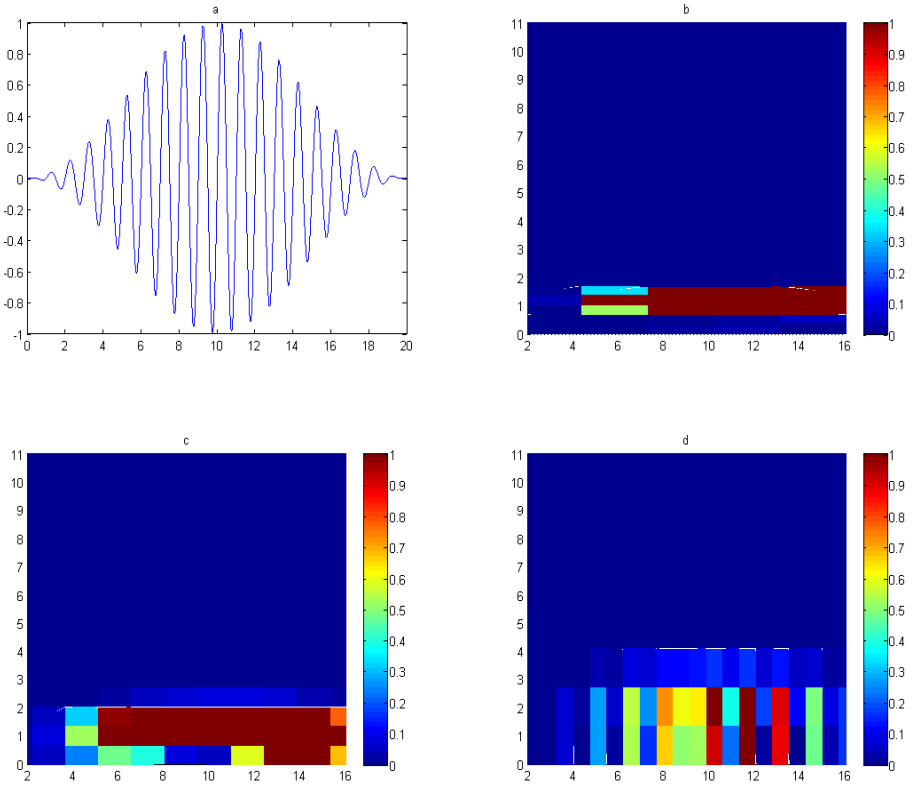

Figure 60: a) time series of an artificially generated wave packet at 1 Hz, b) Fourier transform of the time series averaged over 5 intervals, c) 10 intervals and d) 20 intervals. Colours denote signal power in arbitrary units.

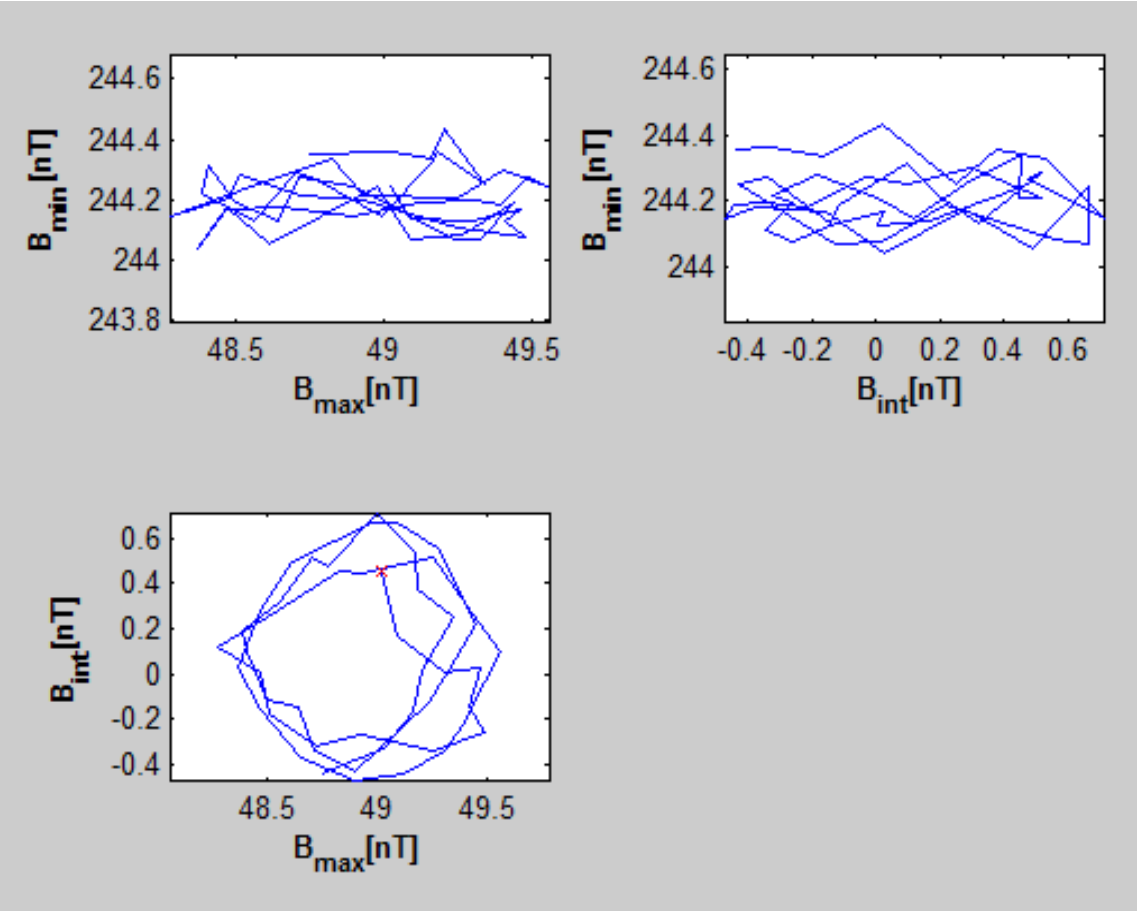

Figure 61: Hodogram representing a fragment of an individual wave packet observed on Cluster 4 during the March 30, 2002 event. The FGM data is projected into the variance reference frame, with orthogonal axes representing the maximum, intermediate and minimum variance directions. The bottom left panel is the view along the minimum variance direction, wave propagation direction is coming out of the page. The circular polarisation of the wave packet can be clearly seen in this picture. The red marker denotes the start of the time series - the wave is left-hand polarised, as expected for an EMIC wave.

as used by [e.g. Shoji et al., 2011]. There, ion abundances are calculated using the method described in Omura et al. [2010] which uses cold plasma wave theory and stop band location, as well as quasi-neutrality and the assumption $He^+ \approx O^+$ to solve 2 simultaneous equations. Meanwhile electron density was calculated from spacecraft potential after fitting the potential profile from the plasma frequency profile where it can be seen on WHISPER [Moullard et al., 2002]. The advantage of these methods is that they do not rely on particle spectrometers for charged particle density information. Mass spectrometers can only register those particles possessing the energy to penetrate the potential barrier and reach the detector; in normal operation this excludes low-energy particles that form the bulk of the population.

It can be seen that the wave packets span a range between $K = 0.11$ and 0.98 where $K = kc/\omega_{H^+}$ is the wavenumber normalised to the ion intertial length. The wave packet location on the dispersion space ($\omega - k$ plane) are seen to follow the cold plasma dispersion relation. Although some wave packets on the triggered emission reach relatively high frequencies, very high wave numbers have not been observed. The highest value of K corresponds to an E_{min} of 990 keV using equation (12) from Silin et al. [2011a]. Silin et al. [2011a] assumes $v_\perp$=0 (0 degree pitch angles) which would by definition fall into the loss cone on the first bounce anyway. Only the first order (cyclotron) resonance is considered. Another important point to note is that equation (11) in the above paper uses a different definition of K to the Pakhotin et al. [2013] version - to convert the values seen on Figure 63 into those used by Silin et al. [2011a], it is necessary to multiply them by $\frac{\omega_{H^+} V_A}{c\Omega_{H^+}}$ where $V_A = B/\sqrt{\mu_0 \rho}$ is the Alfven velocity and ρ is the plasma mass density.

The above analysis indicates that, even for triggered emissions, the minimum resonant energies are around the widely cited 1 MeV range. This contrasts with the observations of [Ukhorskiy et al., 2010] who claim to have observed minimum resonant energies of 400 keV. Minimum energy in this case is obtained directly from wave vector analysis without any inference based on frequency.

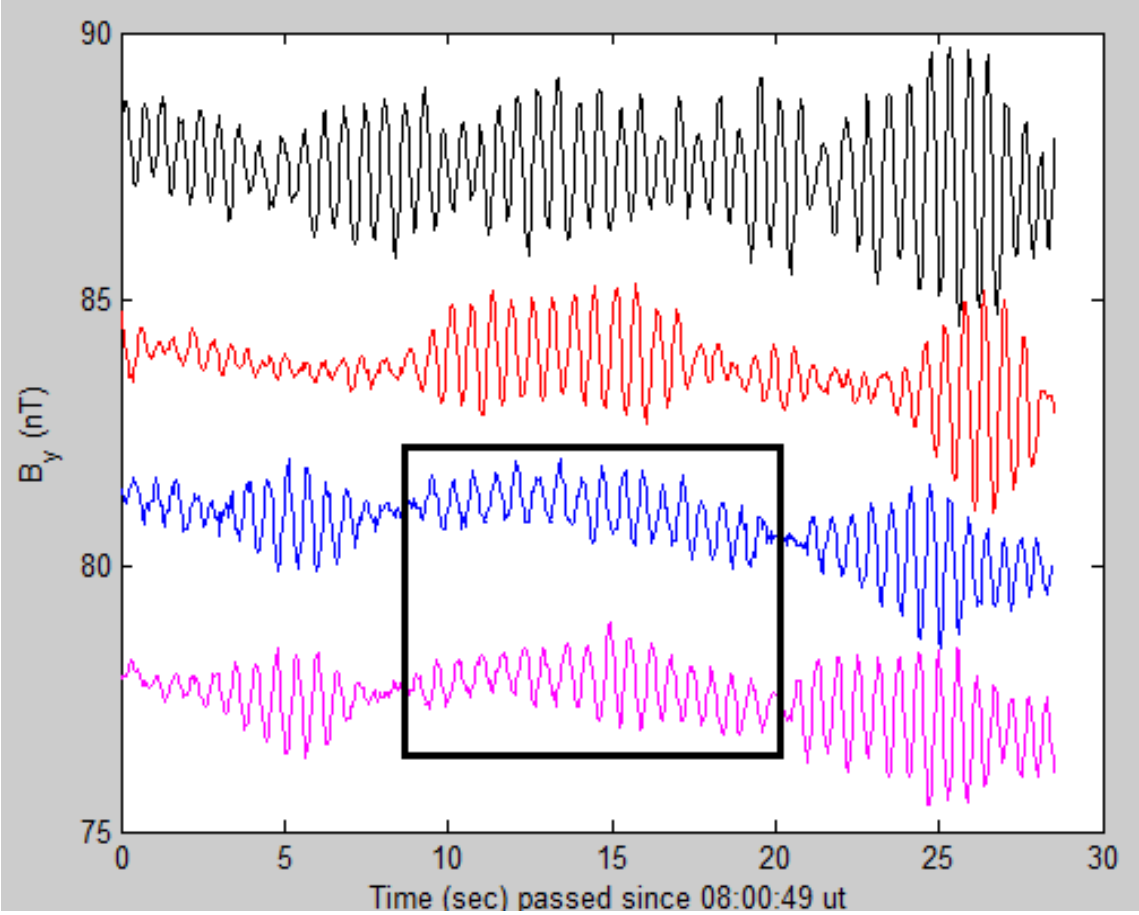

Figure 62: Time series of FGM data showing a wave packet observed simultaneously on two satellites (black square). Cluster 1 is blue, Cluster 2 is red, Cluster 3 is black and Cluster 4 is magenta. The B_y component of field strength has been artificially shifted +5 nT for Cluster 3 and -5 nT for Cluster 4 for easier viewing.

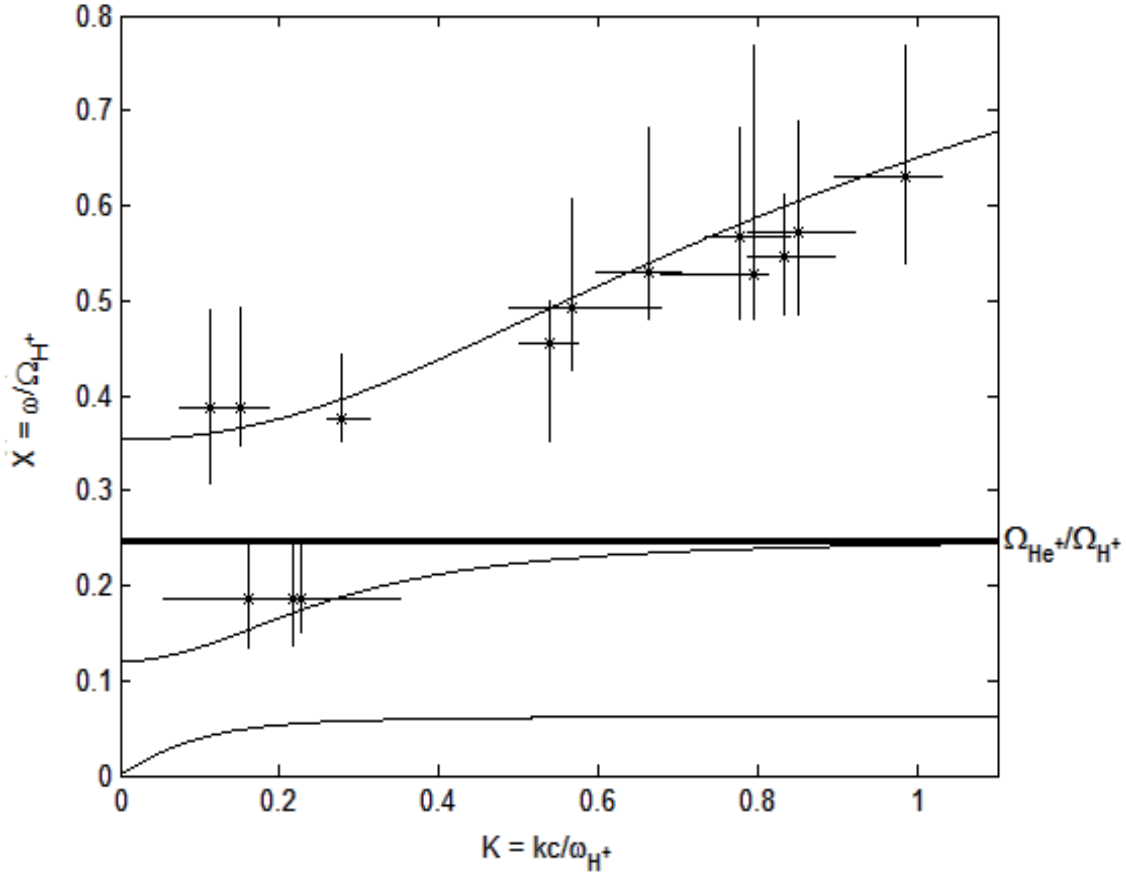

Figure 63: Frequency vs. wavenumber plot for wave packets observed during the event. The bold line marks the helium ion gyrofrequency. The crosses signify ω-k locations for individual wave packets, overplotted with error bars. The solid curves are different branches of the cold plasma dispersion relation for the measured plasma composition.

5.4 Minimum resonant energies in the cusp

[Silin, private communication] reported an EMIC event in the plasmaspheric cusp, which is shown on Figure 64. The figure shows the B_y components of the magnetic field from Cluster 1 and 2, starting on 13:27 UT on March 30, 2002. At that time, the satellite was over the northern pole of the Earth leaving the magnetosphere. The EMIC event is shown inside a black rectangle. Using the phase differencing methodology, a wave number $k = 2.8 \times 10^{-5}$ was obtained. Using CIS and WHISPER data from Cluster 1 at the time of the event, the following densities are obtained: $n_e = 13.5cm^{-3}, n_{H+} = 15.42cm^{-3}, n_{He^+} = 0.2815cm^{-3}, n_{O^+} = 0.1892cm^{-3}$. The ion densities were obtained by normalising CIS fluxes by their total sum and then multiplying each normalised ratio by the electron density. The inherent assumption is that the ion ratios remain constant throughout the energy distribution. Since EMIC waves affect different ions in different ways, the above method is a potential source of inaccuracy. The electron density was a parameter presented in the WHISPER data set and is normally calculated from the plasma frequency and spacecraft potential. The total magnetic field magnitude was 105 nT.

Using equation (12) from [Silin et al., 2011a], the E_{min} obtained for these parameters was 723 keV. This is less than both the GOES-13 lower limit of 800 keV, and the MagEIS energy channel of 891 keV. Other analysis of the same event using the wave telescope technique [Silin, private communication] confirmed energies of around 900 keV - also lower than the 1 MeV frequently cited as the accepted minimum. Even this higher wavenumber could affect a significant part of the distribution observed by GOES-13, and due to inaccuracies may well be as low as the MagEIS channel energy (which is only 9 keV lower).

Cusp dynamics may well be different to those that predominate inside radiation belts. The EMIC wave observed here is a very high-latitude phenomenon, likely corresponding to a very high L-shell, so it is unlikely to affect near-equatorial radiation belt dynamics around L^*=3-7. However, the fact that conditions exist and indeed observations confirm the generation of EMIC waves of energies as low as 723 keV shows that this wave mode cannot be discounted in radiation belt dynamics even at energies below 1 MeV. At high L-shells, where the magnetic field strength is lower, the minimum resonant energies of EMIC waves may well be lower than usual.

5.5 Summary

Wave vector analysis on two EMIC events was performed, and the minimum resonant energy was calculated following the methodology of Silin et al. [2011a]. The aim was to find out whether magnetospheric EMIC waves were capable of scattering electrons significantly below 1 MeV. The minimum energy for an EMIC triggered emission detected by Cluster around L=4-5 was around 1 MeV. Meanwhile, an EMIC wave reported in the cusp later that day above the North pole yielded an E_{min} of 723 keV. Thus, the EMIC triggered emission was deemed

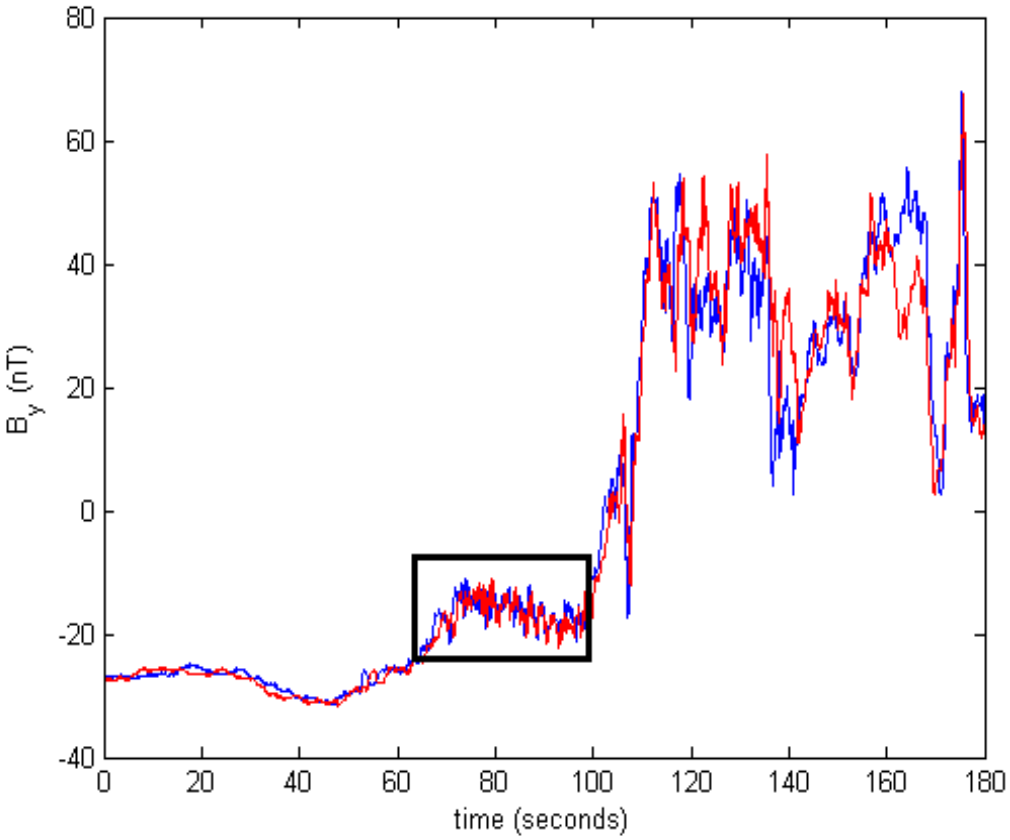

Figure 64: FGM time series of the B_y magnetic field component observed by Cluster 1 (blue) and 2 (red) for a time period starting 13:27:00 UT on March 30, 2002. The black rectangle denotes the EMIC wave.

as likely not capable of significantly affecting the population below 1 MeV, while the cusp event was. Nevertheless it must be noted that the E_{min} of the EMIC triggered emission is very close to 1 MeV and even slightly below it. As such, had it occured under slightly different plasma conditions, it is very feasible for such an emission to be able to cause electron scattering at energies significantly below 1 MeV. No attempt was made to analyse electron precipitation at the time of the two events to determine the energy spectra of the electrons falling into the loss cone. This is left as a further development of this study.

6 Chapter 6: Conclusions

A new radiation belt prediction model combining physics-driven and data science methodologies has been developed and tested. The VNC methodology [Pakhotin et al., 2014] was compared to observations both at GSO and inwards of it, using the Van Allen probes, for a range of representative magnetospheric conditions. The main conclusions are as follows.

1. It is possible to predict radiation belt behaviour by observing high-energy electron fluxes. Although the model suffers from inaccuracies, it does predict fluxes within the right orders of magnitude and successfully simulates radiation belt dynamics, including flux ehnahcements and depletions. A clear link exists with outer boundary variations (derived from NARMAX predictions of high-energy channels at geostationary orbit) and behaviour inside geostationary orbit. That in itself is strong evidence that at least a significant proportion of high-energy fluxes observed at GSO come from outside GSO, and are not locally accelerated electrons that then diffuse outwards. Those populations may still be present, but if they formed the overwhelming majority, the entire scheme would not be effective as a radiation belt forecasting tool as the causality of the processes would be reversed. In addition, some MagEIS observations exist of *two* high-energy populations seemingly coexisting at different L^* values, one of which bears all the hallmarks of a locally accelerated population, while the other appears to originate outwards of the spacecraft's apogee and radially diffuse inwards. This is all strong evidence that points to high-energy GSO fluxes originating as a result of injections from the magnetotail.

2. The model performance should benefit from an hourly forecast of NARMAX, rather than an integral daily one. This will, among other things, create sharper gradients in the outer boundary. Dropouts and depletions will then become more pronounced. It is unclear whether magnetopause shadowing can be successfully modelled by the VERB methodology. On the one hand, the model consistently failed to simulate depletions that penetrate into the heart of the belt, even in tests involving unusually small boundary flux values. On the other hand, in many cases shadowing takes place higher than $L^* = 7$ so the depletion effect is driven by outwards radial diffusion rather than actual areas of near-zero PSD in the simulation space. It is possible that the failure to simulate depletion may be due to small gradients, which themselves are a result of the low time resolution of NARMAX.

3. The model will likely benefit from using a lower-energy channel as an input to the outer boundary. Although it has been demonstrated that high-energy channels can indeed work as a predictor, they are likely contaminated by locally accelerated electrons. The proposed scheme would take low-energy ($\approx$ 100 keV or lower) electron fluxes from the MLT sectors 2200-0200 (which is where particle injections are assumed to come from). Coverage would be maintained by interpolating between several GOES satellites which are closest to these MLT locations. This should capture any injected fluxes, which can then be initialised as an input to the model. Developing a NARMAX simulation specifically for these populations at these MLT sectors will increase the prediction range even further ahead in time. However, any GSO flux information will be constrained by limitations in predicting the Kp index, since that drives the magnetic field model predicting L^* locations from which the fluxes should be taken.

4. The role of EMIC waves for this energy range was unclear and was specifically explored in Chapter 5. This wave mode was omitted in the VNC wave model. A further study using a VERB wave model that involves EMIC, magnetosonic and other waves is warranted to see if this can improve performance. The code was tested for an energy of 891 keV, which is rather close to the generally accepted minimum energies for EMIC resonance ($\approx$ 1 MeV). Considering how efficient this wave type is at pitch-angle scattering, it is well worth including in the future. An experimental run of the simulation involving modified chorus wave diffusion coefficients generated results that suggest pitch-angle scattering is under-represented in the VNC model.

A modification of VNC has been explored where the flux profile is generated as normal and is then scaled by the weighted averages of NARMAX values. The scaling has the effect of increasing the weighting of NARMAX in the system. As such, VNC-S generates improved performance at geostationary orbit, at the cost of degraded performance elsewhere. It is possible to use the VNC and VNC-S systems in tangent - for GSO, VNC-S can be used, while elsewhere, for example in regions near the heart of the radiation belt, VNC should be used.

VNC-S can be used as a high-resolution version of NARMAX. Although the system was designed to output hourly values, in theory it is possible to generate predictions at any frequency. While NARMAX is more accurate at predicting daily integral fluxes, it misses diurnal variations. As noted by Ukhorskiy et al. [2004], diurnal variations may span several orders of magnitude. As a result, even if the models accurately predict daily average fluxes, they have no information on its maximum values, which is important from a space weather standpoint. VNC-M is able to provide information about these local maxima.

One further improvement in the model which is not pursued here would lie in replacing the NARMAX prediction for previous day's flux with the actual GOES-13 measurement of the previous day's flux. This was found to have the effects of making dropouts more pronounced: since the previous day's flux enters into the algorithm from 0100 to 1200 UT, a sudden drop in flux (which would be registered by GOES-13 but potentially missed by NARMAX on that day) will drive the simulated fluxes down. The downside would be a somewhat jagged appearance of the flux profile around dropout periods, as the relatively high

NARMAX prediction would suddenly get replaced by the much lower GOES-13 flux information around 00 UT.

There are still many sources of inaccuracies in the VNC-S model, since this scheme represents a first attempt to combine physical and data-driven models in a rather crude manner. It is recommended that, taking the data science approach, a statistical analysis be carried out to understand which magnetic field model generates the most accurate results under different magnetospheric conditions. The best magnetic field model may then be chosen by the system following this analysis. Preliminary results indicate, for example, that a more dipolar model is more suitable at very low Kp indices. A key problem to resolve is the gradient between L^*=6 and L^*=7. It is possible that if improvements applicable to VNC are implemented, the performance of the VNC-S design will also improve. How the scaling (which itself is a function of geomagnetic activity) interacts with the gradient produced under different geomagnetic conditions is a separate subject for a statistical study.

An EMIC triggered emission and an EMIC wave in the cusp have been evaluated by performing wave vector analysis. The ultimate aim was to find the minimum resonant energy for this wave mode in both cases. This was done in line with earlier work, as the VNC model omitted the EMIC instability. Meanwhile, NARMAX and some other studies (detailed in the literature review of Section 2.1) show that solar wind density has a negative effect on high-energy electron fluxes. This may be because density determines dynamic pressure (which in turn determines the effect of magnetopause shadowing) but that would affect all electron populations simultaneously. There is thus some evidence that solar wind density enters the magnetosphere and creates a favourable environment for EMIC wave excitation. These waves then scatter high-energy particles. The questions were: how low is this minimum resonant energy? VNC studies were mostly performed for $<$ 1 MeV electrons. Could their dynamics also be influenced by this wave mode?

Previous studies concerned with calculating E_{min} did so by inferring the wave number from the linear dispersion equation. Previous analytical work has demonstrated that this approach is flawed in an active magnetosphere, and that it is more accurate to measure the wave vector directly where possible. This analysis was performed on two promising events that were unique in that they had quite high normalised wave numbers. The conclusions are as follows:

1. The EMIC triggered emission on the morning of March 30, 2002, was studied and yielded an E_{min} of around 0.99 MeV. It was observed in the inner magnetosphere where the magnetic field strength and density were both relatively high. Although high wavenumbers were observed for this triggered emission at the highest frequencies, in this case the minimum resonant energy was around 1 MeV and above. Therefore, while this particular emission may have affected electron fluxes in the $>$ 2 MeV energy range, it is unlikely to have an impact on the energy range studied by MagEIS.

2. A cusp EMIC event was reported and observed later on the same day (around 13:27 UT) underwent the same wave vector identification analysis. The minimum energy obtained in this case was much lower - 723 keV. This energy

range is lower than both the MagEIS energy channel considered in the VNC studies, and both of the GOES-13 channels. The magnetospheric cusp has a different set of dynamics governing charged particles and is not generally considered to be a part of the radiation belts. As such, this event is not representative of a radiation belt phenomenon. However, it serves as a demonstration that EMIC waves possessing these minimum resonant energies can exist in the magnetosphere. The ambient plasma conditions - low number densities and a low magnetic field - do exist at high L-shells. The high wavenumbers necessary to achieve these energies, in turn, can occur in a triggered emission.

3. This leads to the postulation that, were a triggered emission to occur at higher L-shells, it may theoretically have an E_{min} significantly lower than 1 MeV. A study of such events is left as a subject for further research. It will also be useful to conduct a conjugate study with an analysis of the energies of precipitating electrons at the time of various EMIC waves, to confirm or reject the validity of the approach detailed by Silin et al. [2011a]. Insofar as including the EMIC wave into a physics-based wave model, it is recommended that this wave be included. As such, analysis of current VNC output for electrons around the energy range of 1 MeV should be treated with caution. VNC has demonstrated a consistent over-estimation of fluxes compared to observations for both quiet and geomagnetically active periods, both inside the outer belt and at geostationary orbit. This could be due to inefficient modelling of magnetopause shadowing, but it could also well be due to the omission of EMIC waves. Further studies are recommended comparing VNC results for times when EMIC activity was observed, to those times when it was not. Insofar as pitch-angle scattering coefficients calculated as a function of energy, it is recommended that they be reviewed using statistical wave vector data, rather than simply Gaussian plots of wave frequency and wave numbers inferred via the dispersion relation. The differences, especially for geomagnetically active periods and at high L-shells, may well be significant.

7 Appendix 1

Calculation of integral flux from two energy channels

Assuming an exponential distribution,

$$J(E) = A\exp(-BE) \tag{31}$$

$$E_1{}^* = \sqrt{E_{min_1}.E_{min_1}} \tag{32}$$

$$E_2{}^* = \sqrt{E_{min_2}.E_{min_2}} \tag{33}$$

$$J(E_1{}^*) = A\exp(-BE_1{}^*) \tag{34}$$

$$J(E_2{}^*) = A\exp(-BE_2{}^*) \tag{35}$$

$$\frac{\exp(-BE_1{}^*)}{J(E_1{}^*)} = \frac{\exp(-BE_2{}^*)}{J(E_2{}^*)} \tag{36}$$

$$-BE_1{}^* - ln(J(E_1{}^*)) = -BE_2{}^* - ln(J(E_2{}^*)) \tag{37}$$

$$ln\frac{J(E_2{}^*)}{J(E_1{}^*)} = (E_1{}^* - E_2{}^*)B \tag{38}$$

$$B = \frac{ln(J(E_2{}^*)) - ln(J(E_1{}^*))}{E_1{}^* - E_2{}^*} \tag{39}$$

$$A = \frac{J(E_2{}^*)}{\exp(-BE_2{}^*)} = \frac{J(E_1{}^*)}{\exp(-BE_1{}^*)} \tag{40}$$

but $J(E) = A\exp(-BE)$

$$J(E{>}\tilde{E_1}) = \int_{\tilde{E_1}}^{\infty} J(E)dE = \frac{A\exp(-B\tilde{E_1})}{B} \tag{41}$$

References

G. A. Abel, M. P. Freeman, A. J. Smith, and G. D. Reeves. Association of substorm chorus events with drift echoes. *Journal of Geophysical Research: Space Physics*, 111(A11):n/a–n/a, 2006. ISSN 2156-2202. doi: 10.1029/2006JA011860. URL `http://dx.doi.org/10.1029/2006JA011860`.

D. N. Baker, R. L. McPherron, T. E. Cayton, and R. W. Klebesadel. Linear prediction filter analysis of relativistic electron properties at 6.6 re. *Journal of Geophysical Research: Space Physics*, 95(A9):15133–15140, 1990. ISSN 2156-2202. doi: 10.1029/JA095iA09p15133. URL `http://dx.doi.org/10.1029/JA095iA09p15133`.

D.N. Baker. Solar wind-magnetosphere drivers of space weather. *Journal of Atmospheric and Terrestrial Physics*, 58(14):1509–1526, October 1996. ISSN 0021-9169. doi: 10.1016/0021-9169(96)00006-2.

M. A. Balikhin, T. Dudok de Wit, H. St. C. K. Alleyne, L. J. C. Woolliscroft, S. N. Walker, V. Krasnosel'skikh, W. A. C. Mier-Jedrzejeowicz, and W. Baumjohann. Experimental determination of the dispersion of waves observed upstream of a quasi-perpendicular shock. *Geophys. Res. Lett.*, 24(7): 787–790, 1997. ISSN 0094-8276.

M. A. Balikhin, O. M. Boaghe, S. A. Billings, and H. S. C. K. Alleyne. Terrestrial magnetosphere as a nonlinear resonator. *Geophys. Res. Lett.*, 28(6):1123–1126, 2001.

M. A. Balikhin, R. J. Boynton, S. N. Walker, J. E. Borovsky, S. A. Billings, and H. L. Wei. Using the narmax approach to model the evolution of energetic electrons fluxes at geostationary orbit. *Geophysical Research Letters*, 38(18), 2011. ISSN 1944-8007. doi: 10.1029/2011GL048980. URL `http://dx.doi.org/10.1029/2011GL048980`.

A Balogh, CM Carr, MH Acuna, MW Dunlop, TJ Beek, P Brown, K-H Fornacon, E Georgescu, K-H Glassmeier, J Harris, et al. The cluster magnetic field investigation: Overview of in-flight performance and initial results. *Ann. Geophys.*, 19:1207–1217, 2001.

S. A. Billings, S. Chen, and M. J. Korenberg. Identification of mimo non-linear systems using a forward-regression orthogonal estimator. *International Journal of Control*, 49:2157–2189, 1989. URL `http://eprints.soton.ac.uk/251146/`. Address: London.

J.B. Blake, P.A. Carranza, S.G. Claudepierre, J.H. Clemmons, Jr. Crain, W.R., Y. Dotan, J.F. Fennell, F.H. Fuentes, R.M. Galvan, J.S. George, M.G. Henderson, M. Lalic, A.Y. Lin, M.D. Looper, D.J. Mabry, J.E. Mazur, B. McCarthy, C.Q. Nguyen, T.P. O'Brien, M.A. Perez, M.T. Redding, J.L. Roeder, D.J. Salvaggio, G.A. Sorensen, H.E. Spence, S. Yi, and M.P. Zakrzewski.

The magnetic electron ion spectrometer (mageis) instruments aboard the radiation belt storm probes (rbsp) spacecraft. *Space Science Reviews*, 179(1-4):383–421, 2013. ISSN 0038-6308. doi: 10.1007/s11214-013-9991-8. URL http://dx.doi.org/10.1007/s11214-013-9991-8.

O. M. Boaghe, M. A. Balikhin, S. A. Billings, and H. Alleyne. Identification of nonlinear processes in the magnetospheric dynamics and forecasting of dst index. *J. Geophys. Res.*, 106(A12):30047–30066, 2001.

Joseph E. Borovsky. Canonical correlation analysis of the combined solar-wind and geomagnetic-index data sets. *Journal of Geophysical Research: Space Physics*, pages n/a–n/a, 2014. ISSN 2169-9402. doi: 10.1002/2013JA019607. URL http://dx.doi.org/10.1002/2013JA019607.

J. Bortnik, R. M. Thorne, T. P. O'Brien, J. C. Green, R. J. Strangeway, Y. Y. Shprits, and D. N. Baker. Observation of two distinct, rapid loss mechanisms during the 20 november 2003 radiation belt dropout event. *Journal of Geophysical Research: Space Physics*, 111(A12):n/a–n/a, 2006. ISSN 2156-2202. doi: 10.1029/2006JA011802. URL http://dx.doi.org/10.1029/2006JA011802.

Jacob Bortnik, Richard M. Thorne, and Nigel P. Meredith. Plasmaspheric hiss overview and relation to chorus. *Journal of Atmospheric and Solar-Terrestrial Physics*, 71(16):1636 – 1646, 2009. ISSN 1364-6826. doi: http://dx.doi.org/10.1016/j.jastp.2009.03.023. URL http://www.sciencedirect.com/science/article/pii/S1364682609000819. Toward an Integrated View of Inner Magnetosphere and Radiation Belts.

R. J. Boynton, M. A. Balikhin, S. A. Billings, H. L. Wei, and N. Ganushkina. Using the NARMAX OLS-ERR algorithm to obtain the most influential coupling functions that affect the evolution of the magnetosphere. *Journal of Geophysical Research: Space Physics*, 116(A5):n/a–n/a, 2011. ISSN 2156-2202. doi: 10.1029/2010JA015505. URL http://dx.doi.org/10.1029/2010JA015505.

R. J. Boynton, M. A. Balikhin, S. A. Billings, G. D. Reeves, N. Ganushkina, M. Gedalin, O. A. Amariutei, J. E. Borovsky, and S. N. Walker. The analysis of electron fluxes at geosynchronous orbit employing a narmax approach. *J. Geophys. Res. Space Physics*, 118:1500–1513, 2013.

D. H. Brautigam and J. M. Albert. Radial diffusion analysis of outer radiation belt electrons during the october 9, 1990, magnetic storm. *Journal of Geophysical Research: Space Physics*, 105(A1):291–309, 2000. ISSN 2156-2202. doi: 10.1029/1999JA900344. URL http://dx.doi.org/10.1029/1999JA900344.

E. Burin des Roziers and X. Li. Specification of ¿2 mev geosynchronous electrons based on solar wind measurements. *Space Weather*, 4(6): n/a–n/a, 2006. ISSN 1542-7390. doi: 10.1029/2005SW000177. URL http://dx.doi.org/10.1029/2005SW000177.

Wallace H. Campbell. Failure of dst index fields to represent a ring current. *Space Weather*, 2(8):n/a–n/a, 2004. ISSN 1542-7390. doi: 10.1029/2003SW000041. URL http://dx.doi.org/10.1029/2003SW000041.

Lunjin Chen, Richard M. Thorne, Yuri Shprits, and Binbin Ni. An improved dispersion relation for parallel propagating electromagnetic waves in warm plasmas: Application to electron scattering. *Journal of Geophysical Research: Space Physics*, 118(5):2185–2195, 2013. ISSN 2169-9402. doi: 10.1002/jgra.50260. URL http://dx.doi.org/10.1002/jgra.50260.

Y. Chen, R. H. W. Friedel, and G. D. Reeves. Phase space density distributions of energetic electrons in the outer radiation belt during two geospace environment modeling inner magnetosphere/storms selected storms. *J. Geophys. Res.*, 111(A11):A11S04, November 2006. ISSN 0148-0227. doi: 10.1029/2006JA011703.

N Cornilleau-Wehrlin, G Chanteur, S Perraut, L Rezeau, P Robert, A Roux, C De Villedary, P Canu, M Maksimovic, Y De Conchy, et al. First results obtained by the cluster STAFF experiment. *Ann. Geophys.*, 21:437–456, 2003.

T. Neil Davis and Masahisa Sugiura. Auroral electrojet activity index ae and its universal time variations. *Journal of Geophysical Research*, 71(3): 785–801, 1966. ISSN 2156-2202. doi: 10.1029/JZ071i003p00785. URL http://dx.doi.org/10.1029/JZ071i003p00785.

P.M.E. Dècrèau, P. Fergeau, V. Krannosels'kikh, Lèvêque, Ph. Martin, O. Randriamboarison, F.X. Senè, J.G. Trotignon, P. Canu, P.B. Mögensen, and WHISPER Investigators. WHISPER, a resonance sounder and wave analyser: Performances and perspectives for the cluster mission. *Space Science Reviews*, 79:157–193, 1997.

L. Desorgher, P. Bühler, A. Zehnder, and E. O. Flückiger. Simulation of the outer radiation belt electron flux decrease during the march 26, 1995, magnetic storm. *Journal of Geophysical Research: Space Physics*, 105(A9): 21211–21223, 2000. ISSN 2156-2202. doi: 10.1029/2000JA900060. URL http://dx.doi.org/10.1029/2000JA900060.

E. F. Donovan and G. Rostoker. Internal consistency of the tsyganenko magnetic field model and the heppner-maynard empirical model of the ionospheric electric field distribution. *Geophysical Research Letters*, 18 (6):1043–1046, 1991. ISSN 1944-8007. doi: 10.1029/91GL01053. URL http://dx.doi.org/10.1029/91GL01053.

Donald H. Fairfield and Gilbert D. Mead. Magnetospheric mapping with a quantitative geomagnetic field model. *Journal of Geophysical Research*, 80 (4):535–542, 1975. ISSN 2156-2202. doi: 10.1029/JA080i004p00535. URL http://dx.doi.org/10.1029/JA080i004p00535.

C.-G. Fälthammar. Effects of time-dependent electric fields on geomagnetically trapped radiation. *J. Geophys. Res.*, 70(11):2503–2516, 1965. ISSN 2156-2202. doi: 10.1029/JZ070i011p02503.

R.H.W Friedel, G.D Reeves, and T Obara. Relativistic electron dynamics in the inner magnetosphere - a review. *Journal of Atmospheric and Solar-Terrestrial Physics*, 64(2):265–282, January 2002. ISSN 1364-6826. doi: 10.1016/S1364-6826(01)00088-8.

N. Y. Ganushkina, O. A. Amariutei, Y. Y. Shprits, and M. W. Liemohn. Transport of the plasma sheet electrons to the geostationary distances. *Journal of Geophysical Research: Space Physics*, 118:82–98, 2013.

N. Y. Ganushkina, M. W. Liemohn, O. A. Amariutei, and D. Pitchford. Low-energy electrons (5-50 kev) in the inner magnetosphere. *Journal of Geophysical Research: Space Physics*, 119(1):246–259, 2014. ISSN 2169-9402. doi: 10.1002/2013JA019304. URL `http://dx.doi.org/10.1002/2013JA019304`.

S. P. Gary, K. Liu, and L. Chen. Alfven-cyclotron instability with singly ionised helium: Linear theory. *J. Geophys. Res.*, 117(A08201), 2012.

B. Grison, O. Santolik, N. Cornilleau-Wehrlin, A. Masson, M. J. Engebretson, J. S. Pickett, Y. Omura, P. Robert, and R. Nomura. Emic triggered chorus emissions in cluster data. *J. Geophys. Res.*, 118(3):1159–1169, 2013. ISSN 2169-9402. doi: 10.1002/jgra.50178.

R. B. Horne, S. A. Glauert, N. P. Meredith, D. Boscher, V. Maget, D. Heynderickx, and D. Pitchford. Space weather impacts on satellites and forecasting the earth's electron radiation belts with spacecast. *Space Weather*, 11(4):169–186, 2013. ISSN 1542-7390. doi: 10.1002/swe.20023. URL `http://dx.doi.org/10.1002/swe.20023`.

Roger H. A. Iles, Nigel P. Meredith, Andrew N. Fazakerley, and Richard B. Horne. Phase space density analysis of the outer radiation belt energetic electron dynamics. *Journal of Geophysical Research: Space Physics*, 111(A3), 2006. ISSN 2156-2202. doi: 10.1029/2005JA011206. URL `http://dx.doi.org/10.1029/2005JA011206`.

A. C. Kellerman and Y. Y. Shprits. On the influence of solar wind conditions on the outer-electron radiation belt. *Journal of Geophysical Research: Space Physics*, 117(A5):n/a–n/a, 2012. ISSN 2156-2202. doi: 10.1029/2011JA017253. URL `http://dx.doi.org/10.1029/2011JA017253`.

A. C. Kellerman, Y. Y. Shprits, and D. L. Turner. A geosynchronous radiation-belt electron empirical prediction (GREEP) model. *Space Weather*, 11(8):463–475, 2013. ISSN 1542-7390. doi: 10.1002/swe.20074. URL `http://dx.doi.org/10.1002/swe.20074`.

Hee-Jeong Kim and Anthony A. Chan. Fully adiabatic changes in storm time relativistic electron fluxes. *Journal of Geophysical Research: Space Physics*, 102(A10):22107–22116, 1997. ISSN 2156-2202. doi: 10.1029/97JA01814. URL http://dx.doi.org/10.1029/97JA01814.

Kyung-Chan Kim, Yuri Shprits, Dmitriy Subbotin, and Binbin Ni. Relativistic radiation belt electron responses to GEM magnetic storms: Comparison of CRRES observations with 3-D VERB simulations. *Journal of Geophysical Research: Space Physics*, 117(A8):n/a–n/a, 2012. ISSN 2156-2202. doi: 10.1029/2011JA017460. URL http://dx.doi.org/10.1029/2011JA017460.

H. C. Koons and D. J. Gorney. A neural network model of the relativistic electron flux at geosynchronous orbit. *Journal of Geophysical Research: Space Physics*, 96(A4):5549–5556, 1991. ISSN 2156-2202. doi: 10.1029/90JA02380. URL http://dx.doi.org/10.1029/90JA02380.

J. H. Lee, L. Chen, V. Angelopoulos, and R. M. Thorne. THEMIS observations and modeling of multiple ion species and EMIC waves: Implications for a vanishing He^+ stop band. *J. Geophys. Res.*, 117(A06204), 2012.

A. M. Lenchek, S. F. Singer, and R. C. Wentworth. Geomagnetically trapped electrons from cosmic ray albedo neutrons. *Journal of Geophysical Research*, 66(12):4027–4046, 1961. ISSN 2156-2202. doi: 10.1029/JZ066i012p04027. URL http://dx.doi.org/10.1029/JZ066i012p04027.

W. Li, R. M. Thorne, Q. Ma, B. Ni, J. Bortnik, D. N. Baker, H. E. Spence, G. D. Reeves, S. G. Kanekal, J. C. Green, C. A. Kletzing, W. S. Kurth, G. B. Hospodarsky, J. B. Blake, J. F. Fennell, and S. G. Claudepierre. Radiation belt electron acceleration by chorus waves during the 17 march 2013 storm. *Journal of Geophysical Research: Space Physics*, pages n/a–n/a, 2014. ISSN 2169-9402. doi: 10.1002/2014JA019945. URL http://dx.doi.org/10.1002/2014JA019945.

Xinlin Li. Variations of 0.7-6.0 mev electrons at geosynchronous orbit as a function of solar wind. *Space Weather*, 2(3):n/a–n/a, 2004. ISSN 1542-7390. doi: 10.1029/2003SW000017. URL http://dx.doi.org/10.1029/2003SW000017.

Xinlin Li, M. Temerin, D. N. Baker, G. D. Reeves, and D. Larson. Quantitative prediction of radiation belt electrons at geostationary orbit based on solar wind measurements. *Geophysical Research Letters*, 28(9):1887–1890, 2001. ISSN 1944-8007. doi: 10.1029/2000GL012681. URL http://dx.doi.org/10.1029/2000GL012681.

Zan Li, Robyn M. Millan, and Mary K. Hudson. Simulation of the energy distribution of relativistic electron precipitation caused by quasi-linear interactions with emic waves. *Journal of Geophysical Research: Space Physics*, 118 (12):7576–7583, 2013. ISSN 2169-9402. doi: 10.1002/2013JA019163. URL http://dx.doi.org/10.1002/2013JA019163.

A. G. Ling, G. P. Ginet, R. V. Hilmer, and K. L. Perry. A neural network-based geosynchronous relativistic electron flux forecasting model. *Space Weather*, 8(9):n/a–n/a, 2010. ISSN 1542-7390. doi: 10.1029/2010SW000576. URL http://dx.doi.org/10.1029/2010SW000576.

Wladislaw Lyatsky and George V. Khazanov. A predictive model for relativistic electrons at geostationary orbit. *Geophysical Research Letters*, 35 (15):n/a–n/a, 2008. ISSN 1944-8007. doi: 10.1029/2008GL034688. URL http://dx.doi.org/10.1029/2008GL034688.

Mark H. MacAlester and William Murtagh. Extreme space weather impact: An emergency management perspective. *Space Weather*, pages n/a–n/a, 2014. ISSN 1542-7390. doi: 10.1002/2014SW001095. URL http://dx.doi.org/10.1002/2014SW001095.

J. P. McCollough, S. R. Elkington, M. E. Usanova, I. R. Mann, D. N. Baker, and Z. C. Kale. Physical mechanisms of compressional emic wave growth. *Journal of Geophysical Research: Space Physics*, 115(A10): n/a–n/a, 2010. ISSN 2156-2202. doi: 10.1029/2010JA015393. URL http://dx.doi.org/10.1029/2010JA015393.

J. P. McCollough, S. R. Elkington, and D. N. Baker. The role of shabansky orbits in compression-related electromagnetic ion cyclotron wave growth. *Journal of Geophysical Research: Space Physics*, 117(A1): n/a–n/a, 2012. ISSN 2156-2202. doi: 10.1029/2011JA016948. URL http://dx.doi.org/10.1029/2011JA016948.

N. P. Meredith, R. M. Thorne, R. B. Horne, D. Summers, B. J. Fraser, and R. R. Anderson. Statistical analysis of relativistic electron energies for cyclotron resonance with emic waves observed on crres. *J. Geophys. Res.*, 108(A6): 1250, June 2003. ISSN 0148-0227. doi: 10.1029/2002JA009700.

Nigel P. Meredith, Richard B. Horne, Richard M. Thorne, Danny Summers, and Roger R. Anderson. Substorm dependence of plasmaspheric hiss. *Journal of Geophysical Research: Space Physics*, 109(A6):n/a–n/a, 2004. ISSN 2156-2202. doi: 10.1029/2004JA010387. URL http://dx.doi.org/10.1029/2004JA010387.

Nigel P. Meredith, Richard B. Horne, and Roger R. Anderson. Survey of magnetosonic waves and proton ring distributions in the earth's inner magnetosphere. *Journal of Geophysical Research: Space Physics*, 113 (A6):n/a–n/a, 2008. ISSN 2156-2202. doi: 10.1029/2007JA012975. URL http://dx.doi.org/10.1029/2007JA012975.

Kyungguk Min, Jeongwoo Lee, and Kunihiro Keika. Chorus wave generation near the dawnside magnetopause due to drift shell splitting of substorm-injected electrons. *Journal of Geophysical Research: Space Physics*, 115 (A5):n/a–n/a, 2010. ISSN 2156-2202. doi: 10.1029/2010JA015474. URL http://dx.doi.org/10.1029/2010JA015474.

O. Moullard, A. Masson, H. Laakso, M. Parrot, P. Dècrèau, O. Santolik, and M. Andre. Density modulated whistler mode emissions observed near the plasmapause. *Geophys. Res. Lett.*, 29(20):36–1–36–4, 2002. ISSN 1944-8007. doi: 10.1029/2002GL015101.

Tsugunobu Nagai. 'space weather forecast': Prediction of relativistic electron intensity at synchronous orbit. *Geophysical Research Letters*, 15(5): 425–428, 1988. ISSN 1944-8007. doi: 10.1029/GL015i005p00425. URL http://dx.doi.org/10.1029/GL015i005p00425.

Satoko Nakamura, Yoshiharu Omura, Shinobu Machida, Masafumi Shoji, Masahito Nosè, and Vassilis Angelopoulos. Electromagnetic ion cyclotron rising tone emissions observed by themis probes outside the plasmapause. *Journal of Geophysical Research: Space Physics*, 119(3):1874–1886, 2014. ISSN 2169-9402. doi: 10.1002/2013JA019146. URL http://dx.doi.org/10.1002/2013JA019146.

F. Němec, O. Santolík, K. Gereová, E. Macúšová, H. Laakso, Y. de Conchy, M. Maksimovic, and N. Cornilleau-Wehrlin. Equatorial noise: Statistical study of its localization and the derived number density. *Advances in Space Research*, 37(3):610 – 616, 2006. ISSN 0273-1177. doi: http://dx.doi.org/10.1016/j.asr.2005.03.025. Boundary Layers, Waves and Non-Linear Dynamical Processes.

T. P. O'Brien. SEAES-GEO: A spacecraft environmental anomalies expert system for geosynchronous orbit. *Space Weather*, 7(9):n/a–n/a, 2009. ISSN 1542-7390. doi: 10.1029/2009SW000473. URL http://dx.doi.org/10.1029/2009SW000473.

T. P. O'Brien, K. R. Lorentzen, I. R. Mann, N. P. Meredith, J. B. Blake, J. F. Fennell, M. D. Looper, D. K. Milling, and R. R. Anderson. Energization of relativistic electrons in the presence of ULF power and MeV microbursts: Evidence for dual ULF and VLF acceleration. *Journal of Geophysical Research: Space Physics*, 108(A8):n/a–n/a, 2003. ISSN 2156-2202. doi: 10.1029/2002JA009784. URL http://dx.doi.org/10.1029/2002JA009784.

Y. Omura, J. Pickett, B. Grison, O. Santolik, I. Dandouras, M. Engebretson, P. M. E. Dècrèau, and A. Masson. Theory and observation of electromagnetic ion cyclotron triggered emissions in the magnetosphere. *J. Geophys. Res.*, 115 (A7):A07234, 2010. ISSN 2156-2202. doi: 10.1029/2010JA015300.

Ksenia Orlova, Maria Spasojevic, and Yuri Shprits. Activity-dependent global model of electron loss inside the plasmasphere. *Geophysical Research Letters*, 41(11):3744–3751, 2014. ISSN 1944-8007. doi: 10.1002/2014GL060100. URL http://dx.doi.org/10.1002/2014GL060100.

I. P. Pakhotin, S. N. Walker, Y. Y. Shprits, and M. A. Balikhin. Dispersion relation of electromagnetic ion cyclotron waves using cluster observations. *Annales Geophysicae*, 31:1437–1446, 2013. doi: 10.5194/angeo-31-1437-2013.

I. P. Pakhotin, A. Y. Drozdov, Y. Y. Shprits, R. J. Boynton, D. Subbotin, and M. A. Balikhin. Simulation of high-energy radiation belt electron fluxes using narmax-verb coupled codes. *Journal of Geophysical Research: Space Physics*, pages n/a–n/a, 2014. ISSN 2169-9402. doi: 10.1002/2014JA020238. URL http://dx.doi.org/10.1002/2014JA020238.

J. S. Pickett, B. Grison, Y. Omura, M. J. Engebretson, I. Dandouras, A. Masson, M. L. Adrian, O. Santolik, P. M. E. Dècrèau, N. Cornilleau-Wehrlin, and D. Constantinescu. Cluster observations of emic triggered emissions in association with pc1 waves near earth's plasmapause. *Geophys. Res. Lett.*, 37 (9):L09104, May 2010. ISSN 0094-8276. doi: 10.1029/2010GL042648.

G. D. Reeves, K. L. McAdams, R. H. W. Friedel, and T. P. O'Brien. Acceleration and loss of relativistic electrons during geomagnetic storms. *Geophys. Res. Lett.*, 30(10):1529, May 2003. ISSN 0094-8276. doi: 10.1029/2002GL016513.

G. D. Reeves, H. E. Spence, M. G. Henderson, S. K. Morley, R. H. W. Friedel, H. O. Funsten, D. N. Baker, S. G. Kanekal, J. B. Blake, J. F. Fennell, S. G. Claudepierre, R. M. Thorne, D. L. Turner, C. A. Kletzing, W. S. Kurth, B. A. Larsen, and J. T. Niehof. Electron acceleration in the heart of the van allen radiation belts. *Science*, 341:991–994, 2013.

H Reme, C Aoustin, JM Bosqued, I Dandouras, B Lavraud, JA Sauvaud, A Barthe, J Bouyssou, Th Camus, O Coeur-Joly, et al. First multispacecraft ion measurements in and near the earth's magnetosphere with the identical cluster ion spectrometry (CIS) experiment. *Ann. Geophys.*, 19:1303–1354, 2001.

J. G. Roederer. *Dynamics of Geomagnetically Trapped Radiation.* Springer-Verlag Berlin Heidelberg New York, 1970.

Christopher T. Russell, Robert E. Holzer, and Edward J. Smith. Ogo 3 observations of elf noise in the magnetosphere: 2. the nature of the equatorial noise. *Journal of Geophysical Research*, 75(4):755–768, 1970. ISSN 2156-2202. doi: 10.1029/JA075i004p00755. URL http://dx.doi.org/10.1029/JA075i004p00755.

K. Sakaguchi, Y. Miyoshi, S. Saito, T. Nagatsuma, K. Seki, and K. T. Murata. Relativistic electron flux forecast at geostationary orbit using kalman filter based on multivariate autoregressive model. *Space Weather*, 11(2):79–89, 2013. ISSN 1542-7390. doi: 10.1002/swe.20020. URL http://dx.doi.org/10.1002/swe.20020.

C. J. Schrijver, R. Dobbins, W. Murtagh, and S. M. Petrinec. Assessing the impact of space weather on the electric power grid based on insurance claims for industrial electrical equipment. *Space Weather*, pages n/a–n/a, 2014. ISSN 1542-7390. doi: 10.1002/2014SW001066. URL http://dx.doi.org/10.1002/2014SW001066.

M. Schulz and L. J. Lanzerotti. *Particle Diffusion in the Radiation Belts, Phys. Chem. Space*, volume 7. Springer, New York, 1974.

V.P. Shabansky. Some processes in the magnetosphere. *Space Science Reviews*, 12(3):299–418, 1971. ISSN 0038-6308. doi: 10.1007/BF00165511. URL `http://dx.doi.org/10.1007/BF00165511`.

M. Shoji and Y. Omura. Simulation of electromagnetic ion cyclotron triggered emissions in the earth's inner magnetosphere. *J. Geophys. Res.*, 116(A5): n/a–n/a, 2011. ISSN 2156-2202. doi: 10.1029/2010JA016351.

M. Shoji, Y. Omura, B. Grison, J. Pickett, I. Dandouras, and M. Engebretson. Electromagnetic ion cyclotron waves in the helium branch induced by multiple electromagnetic ion cyclotron triggered emissions. *Geophys. Res. Lett.*, 38(17): L17102, 2011. ISSN 1944-8007. doi: 10.1029/2011GL048427.

Y. Shprits, D. Kondrashov, Y. Chen, R. Thorne, M. Ghil, R. Friedel, and G. Reeves. Reanalysis of relativistic radiation belt electron fluxes using CRRES satellite data, a radial diffusion model, and a kalman filter. *J. Geophys. Res.*, 112(A12):A12216, December 2007. ISSN 0148-0227. doi: 10.1029/2007JA012579.

Y. Y. Shprits, S. R. Elkington, N. P. Meredith, and D. A. Subbotin. Review of modeling of losses and sources of relativistic electrons in the outer radiation belt i: Radial transport. *Journal of Atmospheric and Solar-Terrestrial Physics*, 70(14):1679–1693, November 2008a. ISSN 1364-6826. doi: 10.1016/j.jastp.2008.06.008.

Y. Y. Shprits, D. A. Subbotin, N. P. Meredith, and S. R. Elkington. Review of modeling of losses and sources of relativistic electrons in the outer radiation belt ii: Local acceleration and loss. *Journal of Atmospheric and Solar-Terrestrial Physics*, 70(14):1694–1713, November 2008b. ISSN 1364-6826. doi: 10.1016/j.jastp.2008.06.014.

Y. Y. Shprits, D. A. Subbotin, A. Y. Drozdov, M. E. Usanova, A. Kellerman, K. Orlova, D. N. Baker, D. L. Turner, and K.-C. Kim. Unusual stable trapping of the ultrarelativistic electrons in the van allen radiation belts. *Nature Physics*, 9:699–703, 2013.

Yuri Y. Shprits, Dmitri Subbotin, and Binbin Ni. Evolution of electron fluxes in the outer radiation belt computed with the VERB code. *Journal of Geophysical Research: Space Physics*, 114(A11), 2009. ISSN 2156-2202. doi: 10.1029/2008JA013784. URL `http://dx.doi.org/10.1029/2008JA013784`.

J.-H. Shue, J. K. Chao, H. C. Fu, C. T. Russell, P. Song, K. K. Khurana, and H. J. Singer. A new functional form to study the solar wind control of the magnetopause size and shape. *Journal of Geophysical Research: Space Physics*, 102(A5):9497–9511, 1997. ISSN 2156-2202. doi: 10.1029/97JA00196. URL `http://dx.doi.org/10.1029/97JA00196`.

I. Silin. No title.

I. Silin, I. R. Mann, R. D. Sydora, D. Summers, and R. L. Mace. Warm plasma effects on electromagnetic ion cyclotron wave mev electron interactions in the magnetosphere. *J. Geophys. Res.*, 116(A5):A05215, 2011a. ISSN 2156-2202. doi: 10.1029/2010JA016398.

I. Silin, R. D. Sydora, I. R. Mann, K. Sauer, and R. L. Mace. Nonlinear evolution of electromagnetic ion cyclotron waves. *Physics of Plasmas (1994-present)*, 18(4):042108, 2011b. doi: http://dx.doi.org/10.1063/1.3571598.

Laura E. Simms, V.A. Pilipenko, Mark J. Engebretson, Geoffrey D. Reeves, A.J. Smith, and Mark Clilverd. Prediction of relativistic electron flux at geostationary orbit following storms:multiple regression analysis. *Journal of Geophysical Research: Space Physics*, pages n/a–n/a, 2014. ISSN 2169-9402. doi: 10.1002/2014JA019955. URL `http://dx.doi.org/10.1002/2014JA019955`.

B. U. Ö. Sonnerup and Jr. Cahill, L. J. Magnetopause structure and attitude from explorer 12 observations. *J. Geophys. Res.*, 72(1):171–183, 1967. ISSN 0148-0227.

T. H. Stix. *The Theory of Plasma Waves*. Mc-Graw Hill, New York, 1962.

Yi-Jiun Su, Jack M. Quinn, W. Robert Johnston, James P. McCollough, and Michael J. Starks. Specification of > 2 MeV electron flux as a function of local time and geomagnetic activity at geosynchronous orbit. *Space Weather*, pages n/a–n/a, 2014. ISSN 1542-7390. doi: 10.1002/2014SW001069. URL `http://dx.doi.org/10.1002/2014SW001069`.

Zhenpeng Su, Fuliang Xiao, Huinan Zheng, and Shui Wang. CRRES observation and STEERB simulation of the 9 october 1990 electron radiation belt dropout event. *Geophysical Research Letters*, 38(6):n/a–n/a, 2011a. ISSN 1944-8007. doi: 10.1029/2011GL046873. URL `http://dx.doi.org/10.1029/2011GL046873`.

Zhenpeng Su, Fuliang Xiao, Huinan Zheng, and Shui Wang. Radiation belt electron dynamics driven by adiabatic transport, radial diffusion, and wave-particle interactions. *Journal of Geophysical Research: Space Physics*, 116 (A4):n/a–n/a, 2011b. ISSN 2156-2202. doi: 10.1029/2010JA016228. URL `http://dx.doi.org/10.1029/2010JA016228`.

D. A. Subbotin, Y. Y. Shprits, M. Gkioulidou, L. R. Lyons, B. Ni, V. G. Merkin, F. R. Toffoletto, R. M. Thorne, R.B. Horne, and M. K. Hudson. Simulation of the acceleration of relativistic electrons in the inner magnetosphere using RCM-VERB coupled codes. *Journal of Geophysical Research: Space Physics*, 116(A8), 2011a. ISSN 2156-2202. doi: 10.1029/2010JA016350. URL `http://dx.doi.org/10.1029/2010JA016350`.

D. A. Subbotin, Y. Y. Shprits, and B. Ni. Long-term radiation belt simulation with the VERB 3-D code: Comparison with CRRES observations. *Journal of Geophysical Research: Space Physics*, 116(A12), 2011b. ISSN 2156-2202. doi: 10.1029/2011JA017019. URL http://dx.doi.org/10.1029/2011JA017019.

Dmitriy Subbotin, Yuri Shprits, and Binbin Ni. Three-dimensional VERB radiation belt simulations including mixed diffusion. *Journal of Geophysical Research: Space Physics*, 115(A3), 2010. ISSN 2156-2202. doi: 10.1029/2009JA015070. URL http://dx.doi.org/10.1029/2009JA015070.

D. Summers and R. M. Thorne. Relativistic electron pitch-angle scattering by electromagnetic ion cyclotron waves during geomagnetic storms. *J. Geophys. Res.*, 108(A4):1143, 2003. ISSN 2156-2202. doi: 10.1029/2002JA009489.

Danny Summers and Chun-yu Ma. A model for generating relativistic electrons in the earth's inner magnetosphere based on gyroresonant wave-particle interactions. *Journal of Geophysical Research: Space Physics*, 105(A2): 2625–2639, 2000a. ISSN 2156-2202. doi: 10.1029/1999JA900444. URL http://dx.doi.org/10.1029/1999JA900444.

Danny Summers and Chun-yu Ma. Rapid acceleration of electrons in the magnetosphere by fast-mode mhd waves. *Journal of Geophysical Research: Space Physics*, 105(A7):15887–15895, 2000b. ISSN 2156-2202. doi: 10.1029/1999JA000408. URL http://dx.doi.org/10.1029/1999JA000408.

Danny Summers, Richard M. Thorne, and Fuliang Xiao. Relativistic theory of wave-particle resonant diffusion with application to electron acceleration in the magnetosphere. *Journal of Geophysical Research: Space Physics*, 103 (A9):20487–20500, 1998. ISSN 2156-2202. doi: 10.1029/98JA01740. URL http://dx.doi.org/10.1029/98JA01740.

R. M. Thorne, M. Li, B. Ni, Q. Ma, J. Bortnik, L. Chen, D. N. Baker, H. E. Spence, G. D. Reeves, M. G. Henderson, C. A. Kletzing, W. S. Kurth, G. B. Hospodarsky, J. B. Blake, J. F. Fennell, S. G. Claudepierre, and S. G. Kanekal. Rapid local acceleration of relativistic radiation-belt electrons by magnetospheric chorus. *Nature*, 504:411–414, 2013.

Bruce T. Tsurutani and Edward J. Smith. Postmidnight chorus: A substorm phenomenon. *Journal of Geophysical Research*, 79(1):118–127, 1974. ISSN 2156-2202. doi: 10.1029/JA079i001p00118. URL http://dx.doi.org/10.1029/JA079i001p00118.

Bruce T. Tsurutani and Edward J. Smith. Two types of magnetospheric elf chorus and their substorm dependences. *Journal of Geophysical Research*, 82 (32):5112–5128, 1977. ISSN 2156-2202. doi: 10.1029/JA082i032p05112. URL http://dx.doi.org/10.1029/JA082i032p05112.

N.A. Tsyganenko. Global quantitative models of the geomagnetic field in the cislunar magnetosphere for different disturbance levels. *Planetary and Space Science*, 35(11):1347 – 1358, 1987. ISSN 0032-0633. doi: http://dx.doi.org/10.1016/0032-0633(87)90046-8. URL http://www.sciencedirect.com/science/article/pii/0032063387900468.

N.A. Tsyganenko. A magnetospheric magnetic field model with a warped tail current sheet. *Planetary and Space Science*, 37(1):5 – 20, 1989. ISSN 0032-0633. doi: http://dx.doi.org/10.1016/0032-0633(89)90066-4. URL http://www.sciencedirect.com/science/article/pii/0032063389900664.

Drew L. Turner and Xinlin Li. Quantitative forecast of relativistic electron flux at geosynchronous orbit based on low-energy electron flux. *Space Weather*, 6(5):n/a–n/a, 2008. ISSN 1542-7390. doi: 10.1029/2007SW000354. URL http://dx.doi.org/10.1029/2007SW000354.

A. Y. Ukhorskiy, M. I. Sitnov, A. S. Sharma, B. J. Anderson, S. Ohtani, and A. T. Y. Lui. Data-derived forecasting model for relativistic electron intensity at geosynchronous orbit. *Geophysical Research Letters*, 31 (9):n/a–n/a, 2004. ISSN 1944-8007. doi: 10.1029/2004GL019616. URL http://dx.doi.org/10.1029/2004GL019616.

A. Y. Ukhorskiy, Y. Y. Shprits, B. J. Anderson, K. Takahashi, and R. M. Thorne. Rapid scattering of radiation belt electrons by storm-time emic waves. *Geophys. Res. Lett.*, 37(9):n/a–n/a, 2010. ISSN 1944-8007. doi: 10.1029/2010GL042906.

James A. Wanliss and Kristin M. Showalter. High-resolution global storm index: Dst versus sym-h. *Journal of Geophysical Research: Space Physics*, 111 (A2):n/a–n/a, 2006. ISSN 2156-2202. doi: 10.1029/2005JA011034. URL http://dx.doi.org/10.1029/2005JA011034.

S. Wing, J. R. Johnson, J. Jen, C.-I. Meng, D. G. Sibeck, K. Bechtold, J. Freeman, K. Costello, M. Balikhin, and K. Takahashi. Kp forecast models. *Journal of Geophysical Research: Space Physics*, 110(A4), 2005. ISSN 2156-2202. doi: 10.1029/2004JA010500. URL http://dx.doi.org/10.1029/2004JA010500.

Y. Yu, J. Koller, and S. K. Morley. Quantifying the effect of magnetopause shadowing on electron radiation belt dropouts. *Annales Geophysicae*, 31(11):1929–1939, 2013. doi: 10.5194/angeo-31-1929-2013. URL http://www.ann-geophys.net/31/1929/2013/.